

Parameter adjustment of nuclear leading-order local pairing energy density functionals

Michael Bender, Karim Bennaceur, Valentin Guillon

¹Université Claude Bernard Lyon 1, CNRS / IN2P3, IP2I Lyon, UMR 5822, F-69622, Villeurbanne, France

13 March 2026

Abstract Phenomenological local pairing energy density functionals (EDFs) are widely used in the literature to complement Skyrme and other forms of effective EDFs that model the in-medium particle-hole interaction in nuclei. Because the amount of pair correlations induced by such pairing EDF scales with the level density of the underlying single-particle spectrum and the size of the pairing-active space, its parameters have to be specifically adjusted for each underlying choice of mean field and pairing regulator. The adjustment of pairing parameters that yield consistent results across many different Skyrme parameter sets is not a trivial task, mainly because of the large scatter in predictions for single-particle spectra.

This study reports on the benchmarking of a protocol for the adjustment of the parameters of a local leading-order (LO) $T = 1$ (like-particle) pairing EDF that consists in adjusting the density-dependence of the 1S_0 pairing gap at the chemical potential in infinite nuclear matter (INM). When using a suitably chosen reference calculation, this protocol leads to consistent results for the odd-even staggering of masses of spherical and heavy deformed nuclei and also for the rotational moments of inertia calculated in a time-reversal-breaking cranked HFB approach.

The implementation of the HFB solver for infinite matter at arbitrary isospin asymmetry used for this study is sketched in appendices. Additional points that are discussed concern (i) the illustration that the gaps at the chemical potential are not necessarily sufficient to completely characterise the pairing interaction in infinite matter, and that adjusting LO pairing EDF to reproduce gaps obtained from finite-range pairing interactions in HFB or from more microscopic calculations can lead to unrealistic predictions for finite nuclei; (ii) the finding that some regions of the parameter space

for the density dependence of the $T = 1$ LO pairing EDF lead to a spurious transition to a Bose-Einstein condensate of di-nucleons in spite of producing realistic pairing correlations for well-bound nuclei; (iii) the correlation between effective mass and the parameters of the LO pairing EDF that control the form factor of the density dependence when reproducing pairing gaps in infinite matter, (iv) the significant impact on the odd-even staggering of masses made by either including or not the spin-gradient terms in the particle-hole part of the Skyrme EDF; (v) the sizeable impact of keeping or not the contribution from the density-dependent LO pairing EDF to the mean fields on the odd-even staggering of radii.

1 Introduction

Pairing correlations affect virtually all aspects of phenomena in nuclear matter and finite nuclei [1–5], from the phases of matter to be found in neutron stars, over the odd-even staggering of nuclear masses, the energy difference between various minima and/or maxima of deformation energy surfaces, the generic difference between the spectra of low-lying states of even-even, odd-mass, and odd-odd nuclei, the moments of inertia of collective rotation and other modes of large-amplitude collective motion, to nuclear reactions, most prominently pair transfer.

Methods based on a phenomenological energy density functional (EDF) that models the effective in-medium interaction provide a widely-used framework to describe the aforementioned phenomena [6, 7]. Many different forms of EDFs are employed in the literature. For some of these, the particle-hole (ph) and particle-particle (pp, also often called pairing or anomalous)

parts of the EDF are generated from the same underlying pseudo-potential with common coupling constants consistently derived from the same parameters, but in the majority of cases the ph and pairing parts of the EDF are constructed independently from one another with unconnected coupling constants. Gogny interactions are an example of the former, whereas the vast majority of parametrisations of the Skyrme EDF are examples of the latter. But even when using separate phenomenological functionals for the ph and pairing parts of the EDF, in order to describe data, the parameters of the pp EDF cannot be chosen independently from those of the ph part of the EDF. The main reason is that the magnitude of pair correlations found in a nuclear system is correlated with the density of single-particle levels [2] that in turn is mainly determined by the ph part of the EDF. The global trend of the density of single-particle levels around the chemical potential is determined by the effective mass [8], and it is well-known that parameter sets of the ph EDF that yield different effective masses require different strength of the pairing interaction [6, 8, 9].

The actual shell structure of finite nuclei, however, always deviates from these global trends, and no available ph EDF is capable of describing all details of the phenomenological level sequences [10–14]. When adjusting the parameters of the pairing EDF to observables from a few given nuclei calculated for different parametrisations of the ph EDF that have the same effective mass, one may still end up with rather different pairing strength for each because the underlying mean fields differ in their (imperfect) reproduction of the single-particle spectra.

This can pose consistency problems when constructing series of parametrisations that, in a controlled way, differ in some property that affects single-particle spectra. We think it is therefore opportune to investigate if the parameters of the pairing EDF can be adjusted in a more robust way that is only sensitive to the global trends of single-particle spectra, but not their details.

There have been attempts to construct non-empirical parametrisations of the pairing EDFs through the direct mapping of two-body matrix elements obtained within a microscopic method on those defining the EDF without passing through many-body observables [15–17]. While such studies greatly help to understand the origin and global features of the effective in-medium pairing interaction, for the time being the results do not yet have the predictive power needed for detailed nuclear structure studies.

Another possibility that has been used in the past is to reproduce phenomenological data for the nucleon-nucleon scattering length in the vacuum [18–20]. Such

procedure, however, has also its limits as it does not control the in-medium aspects of the effective pairing interaction.

An alternative possibility is offered by the pairing properties of homogeneous infinite nuclear matter (INM). The continuous single-particle spectrum of INM only depends on the (in general momentum-dependent) effective mass of nucleons in the nuclear medium that varies smoothly with density, proton-neutron asymmetry and spin polarisation. With this, homogeneous INM provides a robust framework for the study of the features of pairing interactions that is free of the complications of finite nuclei with their discrete single-particle spectra whose bunching around the chemical potential that strongly varies with proton and neutron number and also deformation.

Calculations of paired INM also offer the possibility to adjust the parameters of the EDF to some reference pairing gaps obtained with more microscopic models that construct a correlated wave function of paired INM [21–23]. When aiming at the predictive EDF description of pairing correlations in nuclei, however, it has to be recalled that the pairing gap is affected by the coupling of nucleon pairs to excitation modes that have a different nature in infinite matter [24–27] and systems with a surface such as finite nuclei [2, 28–33]. For the purpose of this study, we will not touch upon this issue but address the question of how the simplicity of HFB calculations of paired INM can be used to transfer the predictive power of a given reference pairing EDF constructed for a specific ph EDF to calculations of finite nuclei with a different ph EDF. The main goals of this study are

1. the set-up of the tools for the calculation of isospin-asymmetric paired INM under conditions that match the schemes used to calculate paired finite nuclei with the Skyrme ph EDF, used in both its standard NLO and extended N2LO forms;
2. the analysis of the effect of each of the parameters of the widely used density-dependent local LO $T = 1$ pairing EDF on pairing correlations in INM;
3. the analysis of the connection between pairing correlations in INM and finite nuclei, and how this link can be used to adjust the parameters of LO pairing EDFs that have comparable performance irrespective of the underlying ph mean fields;
4. the analysis of results for three observables that are known to be sensitive to pairing correlations for isotopic chains of spherical and deformed nuclei obtained with symmetry-breaking 3d HFB calculations, which are the odd-even staggering of masses, the odd-even staggering of charge radii, and the ro-

tational moment of inertia in the yrast band of even-even nuclei.

Along the way, we will also investigate a number of consequences of some choices frequently made for the *particle-hole* EDF on the performance of the *pairing* EDF, in particular concerning spin-gradient terms in the ph Skyrme EDF and the contribution from density-dependent pairing EDFs to the ph mean fields.

We also confirm the earlier observation that for some regions of its parameter space the $T = 1$ density-dependent LO pairing EDF produces a nonphysical instability towards Bose-Einstein condensate of di-nucleons that jeopardises HFB calculations for weakly-bound nuclei, and this in spite of producing realistic pairing correlations for well-bound nuclei.

2 The energy density functional

2.1 The mean-field EDF

Calculations presented in what follows are performed using parametrisations of the standard Skyrme EDF at next-to-leading order (NLO) and of an extended Skyrme EDF at next-to-next-to-leading order (N2LO). The generator of the NLO Skyrme EDF contains two-body terms with up to two gradients, to which the generator of the N2LO Skyrme EDF adds terms with four gradients.

Throughout this paper, we use the notation and conventions of Ref. [34]. The complete expression for the Skyrme EDF, which for the calculations of odd-mass nuclei and rotational bands comprises all time-even and time-odd terms, the local densities as well as potentials can be found in that reference.

For our study we consider the SLy4 [35], 1T2T(0.70), 1T2T(0.80) (which is also called SLy7*), and 1T2T(0.85) parametrisations [9] of the EDF at NLO as well as the SN2LO1 parameter set [36] of the EDF at N2LO. All of these were adjusted with similar fitting protocols. Compared to the widely-used SLy4, the recent 1T2T(X) parameter sets have a more realistic surface energy [9]. They differ in their isoscalar effective k -mass that has been set to the values $m_0^*/m = 0.7, 0.8,$ and 0.85 as indicated between the parentheses. SN2LO1 is the first local N2LO parametrisation that has been adjusted to describe properties of finite nuclei [34, 36].

SLy4 and SN2LO1 follow the widely-used practice of considering only the one-body part of the centre-of-mass (CM) correction, whereas the 1T2T(X) employ the full one-body and two-body contributions [9].

For the 1T2T(X) and SN2LO1 parameter sets the complete set of particle-hole terms obtained from the respective Skyrme generator is kept in the ph part of

the EDF, including the spin-tensor terms and all time-odd terms, with coupling constants as obtained from a Skyrme generator. By contrast, for SLy4 the spin-tensor terms are omitted, as is done for many parametrisations of the NLO Skyrme EDF. For reasons of Galilean invariance and internal consistency, the time-odd terms that contain two gradients and two Pauli matrices are then also usually neglected as done in Refs. [13, 37–39]. As explained in Appendix E, this choice made for SLy4 has some unexpected consequences for properties of finite nuclei that are relevant for our study.

When keeping the time-odd terms of the Skyrme EDF with their native coupling constant, many standard parametrisations exhibit finite-size instabilities in the spin channels at densities probed by finite nuclei [40–42]. The presence of these instabilities jeopardises the possibility to converge blocked configurations and self-consistently cranked calculations for collective rotational bands. Such nonphysical behaviour can be avoided when adjusting the parameter sets with a constraint on the response properties of infinite matter [43], which has been done during the adjustment of the 1T2T(X) and SN2LO1. For SLy4, the absence of spin-gradient terms in the EDF sidesteps this problem [40].

Running the calculations for the present study, however, we noticed that some of the calculations of high-spin states of Yb isotopes presented in Sec. 5 diverge when being run with SN2LO1. Further analysis revealed that SN2LO1 is on the edge of the onset of a finite-size spin instability in the $T = 0$ channel. In the notation of Ref. [34], a small reduction of the coupling constant of the time-odd isoscalar spin-gradient term $A_{0,o}^{(2,1)} \mathbf{D}_0^{1,\sigma}(\mathbf{r}) \cdot \Delta \mathbf{D}_0^{1,\sigma}(\mathbf{r})$ from its Skyrme-force generated value $A_{0,o}^{(2,1)} = 32.925 \text{ MeV fm}^5$ to 28.0 MeV fm^5 removes the problem, at least for the resolution of the coordinate-space mesh used for our calculations. The coupling constant of this term can be changed without compromising the Galilean invariance of the Skyrme EDF, but this modification introduces a small violation of the exchange symmetry of the EDF (in addition to those already present because of density-dependent terms and the use of different EDFs for the particle-hole and particle-particle channels) [44–46]. All calculations of time-reversal-invariance breaking configurations reported here were done with this modification of the SN2LO1 parameter set that leaves time-reversal-conserving states unaffected.

For all parameter sets, in calculations of finite nuclei the Coulomb exchange energy [47] is calculated in Slater approximation [48], while the Coulomb pairing energy [47] is neglected. The strategy for the adjustment of the parameters of the pairing EDF is the main subject of our study.

2.2 The pairing EDF

Using the notation and definitions of Ref. [34] for the local isoscalar density $D_0^{1,1}(\mathbf{r})$ and the local pair densities $\tilde{D}_q^{1,1}(\mathbf{r})$ and $\tilde{C}_q^{1,1}(\mathbf{r})$ of protons and neutrons, the local $T = 1$ LO pairing EDF of Ref. [37] reads

$$E_{\text{pair}} = \int d^3r \frac{V_0}{4} \left[1 - \eta \left(\frac{D_0^{1,1}(\mathbf{r})}{\rho_{\text{ref}}} \right)^\sigma \right] \times \sum_{q=n,p} \left[\tilde{D}_q^{1,1*}(\mathbf{r}) \tilde{D}_q^{1,1}(\mathbf{r}) + \tilde{C}_q^{1,1*}(\mathbf{r}) \tilde{C}_q^{1,1}(\mathbf{r}) \right]. \quad (1)$$

The term bilinear in $\tilde{D}_q^{1,1}(\mathbf{r})$ represents the time-even part of the EDF, whereas the term bilinear in $\tilde{C}_q^{1,1}(\mathbf{r})$ is the time-odd part, a distinction that cannot be made in traditional notation [34]. This EDF represents the anomalous part of the HFB expectation value of the density-dependent $S = 0$, $T = 1$ two-body contact pairing interaction

$$v_{\text{pair}}(\mathbf{r}_1 \sigma_1 \tau_1, \mathbf{r}_2 \sigma_2 \tau_2, \mathbf{r}'_1 \sigma'_1 \tau'_1, \mathbf{r}'_2 \sigma'_2 \tau'_2) = V_0 \hat{H}_{S=0} \left[1 - \eta \left(\frac{D_0^{1,1}(\mathbf{R}_{12})}{\rho_{\text{ref}}} \right)^\sigma \right] \delta_{\mathbf{r}_1, \mathbf{r}_2} \delta_{\mathbf{r}_1, \mathbf{r}'_1} \delta_{\mathbf{r}_2, \mathbf{r}'_2}, \quad (2)$$

where $\mathbf{R}_{12} = (\mathbf{r}_1 + \mathbf{r}_2)/2$ is the position of the centre-of-mass of the two nucleons at \mathbf{r}_1 and \mathbf{r}_2 . The operator $\hat{H}_{S=0} = \frac{1}{2} (1 - \hat{P}_{12}^\sigma)$, where \hat{P}_{12}^σ is the spin-exchange operator, projects on $S = 0$ two-body states [49], which for a gradientless two-body contact force implies simultaneous projection on $T = 1$. For historical reasons, there is a redundant factor $\rho_{\text{ref}} = 0.16 \text{ fm}^{-3}$ in the density-dependence that represents the saturation density of INM, such that η parametrises the mixture between volume ($\eta = 0$) and surface ($\eta = 1$) character of the pairing interaction.

Besides the overall strength V_0 , this pairing EDF has two additional parameters that affect the spatial dependence of the pairing potential in finite nuclei. The parameter already mentioned η controls the ratio between pure volume ($\eta = 0$) and pure surface pairing ($\eta = 1$), with the intermediate case $\eta = 1/2$ usually being called ‘‘mixed pairing’’. By contrast, for $\eta > 0$, the parameter σ controls the width of the peak of the pairing potential at the nuclear surface, see the illustrations in Sec. 4, where the effect of these two parameters on the density-dependence of the pairing gap in INM will be analysed.

Many authors use a generalisation of the EDF of Eq. (1) for which different strength parameters V_p and V_n are used for protons and neutrons [13, 39, 50–53] that

slightly improves the description of empirical data. Although this choice is widely used in studies of finite nuclei, it will not be considered here because using such an EDF for the study of pairing correlations in INM leads to different pairing gaps of protons and neutrons in matter with $\rho_p = \rho_n$ that therefore would not be symmetric. We therefore stick to a form of the pairing EDF with a single strength V_0 .

Some authors have instead added a dependence on the isovector density [23, 54–57] to the pairing EDF of Eq. (1). While this is clearly needed to simultaneously reproduce microscopic results for pairing gaps in symmetric and neutron matter [23, 58–62], it turns out that the available experimental information on pairing gaps across the chart of nuclei is not sufficient for the reliable determination of a possible isovector density dependence of the pairing EDF [56]. For reasons that will become clear in the further discussion, for the present study we will stick to the simpler form of Eq. (1).

Before analysing the effect of the various parameters of the pairing EDF (1) on the pairing gaps in INM, we recall that for the observed odd-even staggering of masses of heavy nuclei there is no clear-cut difference in global performance between volume and surface character of this pairing EDF when the strength V_0 is adjusted within the same protocol [51, 63]. By contrast, the evolution of moments of inertia in rotational bands slightly prefers a surface character [37, 39]. A phenomenological difference between the surface and volume character of the pairing EDF becomes also evident in pair transfer reactions [64, 65], but the comparison with data requires beyond-mean-field techniques, as discussed for example in Refs. [66, 67].

Unless explicitly stated otherwise, for all calculations discussed in what follows, the contribution of the pairing EDF to the mean-field potentials is kept and added to the terms obtained from the variation of the Skyrme EDF

$$F_q^{1,1}(\mathbf{r}) = \frac{\delta \mathcal{E}_{Sk}}{\delta D_q^{1,1}(\mathbf{r})} - \frac{V_0}{4} \frac{\eta \sigma}{\rho_{\text{ref}}^\sigma} \sum_q \tilde{D}_q^{1,1*}(\mathbf{r}) \tilde{D}_q^{1,1}(\mathbf{r}) [D_0^{1,1}(\mathbf{r})]^{\sigma-1}. \quad (3)$$

The second term brings a small positive contribution to the single-particle potentials $F_q^{1,1}(\mathbf{r})$ that depends on the magnitude of pairing correlations as measured by the size of the pair density $\tilde{D}_q^{1,1}(\mathbf{r})$. With pairing correlations being in general stronger in even isotopes than in odd ones, this introduces a small odd-even effect on the potentials’ depth that through self-consistency leads to a small odd-even effect of nuclear radii [68–75] that will be analysed in Sec. 5.2.

The contact interaction (2) has an infinite range and a non-decreasing strength in momentum space and therefore couples too strongly bound nucleons to states at arbitrarily large momentum. This leads to a divergence of the HFB equations with increasing number of active single-particle levels, which can be avoided by either renormalising the pairing strength for a given model space, or by introducing a cutoff in energy [76–78].

There are several possible strategies for introducing a cutoff. Their numerical efficiency depends on the numerical representation and the algorithm chosen to solve the HFB equations. For reasons of its simplicity when using the two-basis method in coordinate space as done here, we use a cutoff that acts in the basis that diagonalises the single-particle Hamiltonian \hat{h} [37, 48, 50, 79, 80]. In this basis, the pairing energy and the matrix elements of the pairing field are

$$E_{\text{pair}} = \frac{1}{2} \sum_{ijkl} v_{ijkl} \kappa_{ij}^* \kappa_{kl}, \quad (4)$$

$$\Delta_{ij} = \sum_{kl} v_{ijkl} \kappa_{kl}. \quad (5)$$

Using the cutoff factors f_i , these quantities can be regularized and expressed in the form [81]

$$E_{\text{pair}} = \frac{1}{2} \sum_{ijkl} v_{ijkl} f_i \kappa_{ij}^* f_j f_k \kappa_{kl} f_l, \quad (6)$$

$$\Delta_{ij} = \frac{1}{2} f_i f_j \sum_{kl} v_{ijkl} f_k \kappa_{kl} f_l. \quad (7)$$

The cutoff factors f_i can be absorbed into the definition of the local pair densities [34], see Appendix B.2 for the special case of INM calculations.

One possible functional form for the cutoff is a root of a Fermi function parametrised by a range E_{cut} and the width of the interval over which the cutoff falls to zero [79, 80] that cuts above and below the chemical potential λ_q

$$f_i(\varepsilon_i) = [1 + e^{(\varepsilon_i - \lambda_q - E_{\text{cut}})/\mu}]^{-1/4} \times [1 + e^{(-\varepsilon_i + \lambda_q - E_{\text{cut}})/\mu}]^{-1/4}. \quad (8)$$

The same cutoff is used for calculations of INM and finite nuclei.

A widely-used reference parametrisation of the pairing EDF (1) with the cutoff (8) and originally adjusted in Ref. [37] to describe the evolution of the moment of inertia of the yrast superdeformed band of ^{194}Hg in calculations with the SLy4 parametrisation of the NLO Skyrme EDF, is given by $V_0 = -1250 \text{ MeV fm}^3$, $\eta = \sigma = 1$, $\rho_{\text{ref}} = 0.16 \text{ fm}^{-3}$, $E_{\text{cut}} = 5 \text{ MeV}$, $\mu = 0.5 \text{ MeV}$. This choice of parameters has also been very

successfully used together with other parametrisations of the Skyrme EDF with same effective mass that were adjusted with slight variations of the same fit protocol [9, 82]. For the rest of this paper, we will call this specific parametrisation of the EDF (1) ‘‘ULB pairing’’ as already done in Ref. [77].

To avoid the occasional breakdown of pairing correlations in finite nuclei, the original ULB pairing was adjusted within a Lipkin-Nogami (LN) scheme [37]. The LN scheme has, however, the disadvantage that it is non-variational and therefore might not converge to the energetically lowest configuration. For the calculations of finite nuclei reported here we use instead the stabilisation of the pairing EDF as proposed in Ref. [83]

$$E_{\text{pair}}^{\text{stab}} = E_{\text{pair}} \left(1 + \frac{E_{\text{cut},b}^2}{E_{\text{pair}}^2} \right) \quad (9)$$

with E_{pair} given by Eq. (6) and $E_{\text{cut},b} = 0.3 \text{ MeV}$ for the cutoff parameter. Neither the LN scheme nor the stabilisation of Ref. [83] can however be meaningfully used for INM calculations.

There is no observable that directly allows for quantifying the amount of pairing correlations present in a given system. Some quantities that can nonetheless be used to quantify pairing from the change of some observable between two different states are discussed in Sec. 5.1. The amount of pairing correlations predicted by the HFB calculation can be quantified with weighted averages of the matrix elements Δ_k . One possibility is using $\kappa_{i\bar{j}}$ as the weight factor [50, 83, 84], which in the HF basis of a fully paired time-reversal invariant quasi-particle vacuum yields

$$\langle uv\Delta \rangle_q \equiv \frac{\sum_{i,j>0} \kappa_{i\bar{j}} f_i f_j \Delta_{\bar{j}i}}{\sum_{i,j>0} \kappa_{i\bar{j}} f_i f_j}. \quad (10)$$

In the canonical basis $\kappa_{i\bar{j}} = v_i u_j \delta_{\bar{j}i}$, which explains the symbol used. When the cutoff is defined in the HF basis as done here, however, there is no advantage of summing in the canonical basis. Note that only one matrix element contributes per pair, otherwise the denominator would be zero since $\kappa_{i\bar{j}} = -\kappa_{\bar{j}i}$. Both the numerator and the denominator should include the cutoff factor as done in [83] in order to limit the sum to levels that can contribute to pairing correlations, which is not always done. For the pairing EDF of Eq. (1) with cutoffs (6) this gap can also be expressed with pair densities that absorb the cutoff factors (B.53)

$$\langle uv\Delta \rangle_q = \frac{\int d^3r \tilde{D}_q(\mathbf{r}) \tilde{F}_q^{1,1}(\mathbf{r})}{\int d^3r \tilde{D}_q(\mathbf{r})}. \quad (11)$$

In this expression, the additional relative phases of the single-particle states remove all ambiguities about the single-particle states that have to be summed over.

An alternative is to construct an average gap weighted by ρ_{ij} [8, 50, 85], which, in the HF basis of a fully paired time-reversal invariant quasiparticle vacuum, leads to

$$\langle v^2 \Delta \rangle_q \equiv \frac{\sum_{i,j>0} \rho_{ij} f_i f_j \Delta_{\bar{i}}}{\sum_{i,j>0} \rho_{ij} f_i f_j}. \quad (12)$$

The sum is again only over half of the single-particle states, as otherwise in this case the numerator would now become zero. Note that including or not the cutoff factors f_k in the denominator of Eq. (12) can make a huge quantitative difference for $\langle v^2 \Delta \rangle_q$ when using a cutoff that acts both above and below the chemical potential as done here. The reason is that deeply-bound single-particle states with $\rho_{ii} \simeq 1$ for which the cutoff leads to $\Delta_{\bar{i}} \simeq 0$ would contribute to the sum in the denominator, but not to the sum in the numerator. In analogy to Eq. (11), expression (12) can also be rewritten in terms of an integral over the pair potential times a density in the nominator and an integral over the same density in the denominator. The density in question, however, is a normal density that contains the pairing cutoff factors, which is an object that unlike $\bar{D}_q(\mathbf{r})$ is not needed for the calculation of the total energy or any other quantity.

2.3 HFB calculations of finite nuclei

Unless specified otherwise, the calculations for finite nuclei reported here are performed with the MOCCA code [86, 87] that solves the HFB equations with the two-basis method as described in Ref. [81] in a 3d coordinate-space representation with Lagrange-mesh techniques that provide a very high numerical accuracy for derivatives and integrals even when working with a coarse discretisation [88]. As often done, we impose a point-group symmetry on the single-particle states that are chosen to be eigenstates of the signature \hat{R}_z , parity \hat{P} and time-simplex \check{S}_y^T , which introduces three plane symmetries for the densities, as discussed in Appendix D of Ref. [34]. Ground states of even-even nuclei are calculated imposing in addition time-reversal invariance, whereas the calculations of blocked one-quasiparticle (1qp) configurations of odd nuclei and rotational states of even-even nuclei are calculated allowing for time-reversal-breaking configurations.

The 1qp configurations of odd nuclei are constructed through self-consistently blocking the quasiparticle that has the largest overlap with a given eigenstate of the single-particle Hamiltonian. We limit ourselves here to nuclei for which a fully paired non-blocked calculation of the “false vacuum” with odd neutron number yields either a spherical or axially-symmetric configuration

such that the blocked quasiparticles have a half-integer expectation value of $\langle \hat{j}_z \rangle = K$ in the false vacuum. This is the angular-momentum quantum number that we attribute also to the blocked many-body configuration.

Because of rearrangement and polarisation effects in self-consistent HFB calculations, however, at convergence of a blocked HFB calculation with a 3d code the many-body expectation value of total angular momentum $\langle \hat{J}_z \rangle$ will in general slightly differ from the single-particle expectation value of the angular momentum $\langle \hat{j}_z \rangle$ of the blocked neutron in the canonical basis, and both will in general differ from the value of K in the false vacuum used to initialise the calculation. This particularly becomes an issue when there are near-degenerate (or energetically lower) quasiparticles with same signature and parity that can mix with the targeted one in a 3d calculation. To stabilise the convergence of the blocked HFB calculations towards the targeted configuration and to facilitate comparison with experiment, we impose the condition $\langle \hat{J}_z \rangle = K$ with a principal-axis cranking constraint that adjusts the rotational frequency ω_z to the targeted value of $\langle \hat{J}_z \rangle$.

For the well-deformed Yb isotopes that can be assumed to satisfy the strong-coupling limit where $K = J$ [49, 91], the nucleus is oriented in the numerical box such that its long axis is aligned with the z axis. Only the $\langle \hat{j}_z \rangle > 0$ level from each Kramers-degenerate pair with single-particle energy near the chemical potential of neutrons in the false vacuum is blocked; blocking its partner state would converge to the time-reversed many-body configuration that has the same energy, but an angular momentum that points into the opposite direction.

For the spherical Sn and Pb isotopes, only the state with projection $\langle \hat{j}_z \rangle = j$ out of a given j -shell is blocked. It is to be noted that blocking a different substate of a given spherical j shell with half-integer $|K| < j$ in the false vacuum with the same procedure yields in general a slightly different total energy at convergence. This is because of the broken alispin-symmetry in a code that imposes point-group symmetries as done here [92] such that blocking different magnetic substates of a given j -shell cannot generate configurations whose current and spin density distributions are related by a global rotation.

Some calculations of even-even Sn and Pb isotopes are performed with a spherical code [93] that uses the same numerical representation as MOCCA, i.e. it also solves the HFB equations with the two-basis method in a Lagrange-mesh coordinate-space representation, but in this case for a radial mesh. For spherical nuclei this code and MOCCA yield almost identical results within a few keV for binding energies.

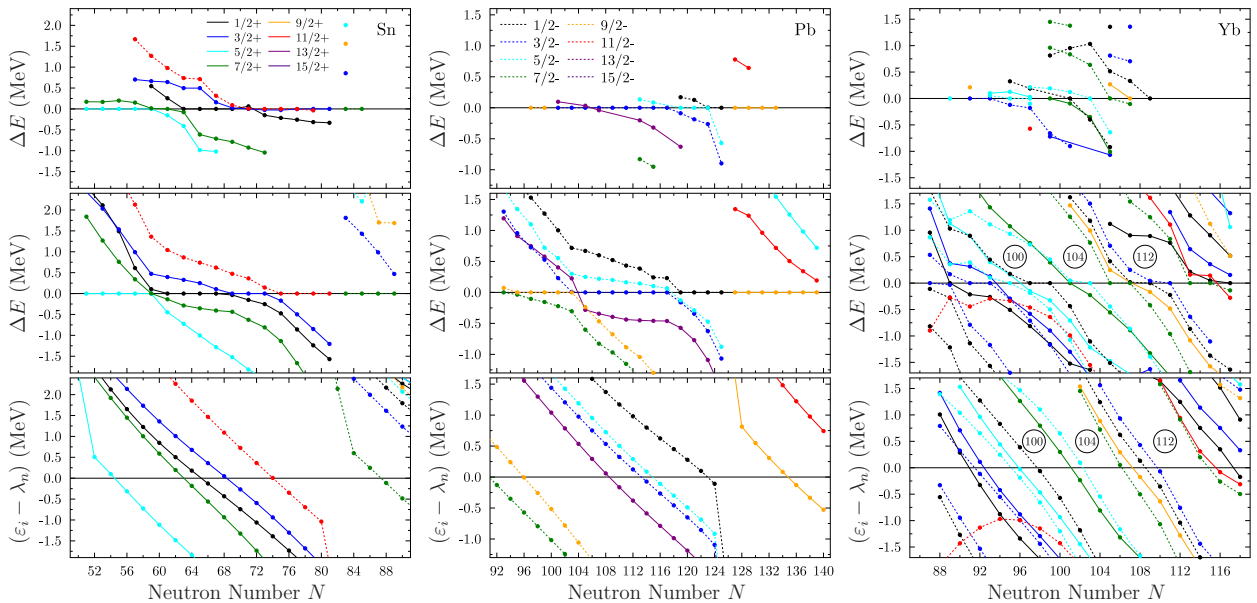


Fig. 1 Total energies ΔE of 1qp configurations in odd-mass Sn, Pb, and Yb isotopes relative to the ground state extracted from [89, 90] (upper row) compared with calculations with 1T2T(0.80) (also known as SLy7*) (middle row) for states with $K = \langle \hat{J}_z \rangle$ and parity as indicated. Following the convention of Ref. [13], the sign indicates if the dominant single-particle component of the blocked qp is above (positive) or below (negative) the chemical potential (see text). Solid (dotted) lines indicate configurations of positive (negative) parity, whereas colour indicates angular momentum. The lower row displays the difference between the eigenvalues of the single-particle Hamiltonian ε_i and the chemical potential of neutrons λ_n in the even-even isotopes in between. For Yb isotopes, several deformed neutron shell closures predicted by 1T2T(0.80) are indicated.

For the purpose of this study we also have set up a new tool to calculate paired isotropic homogeneous infinite matter that will be described in Sec. 3 and Appendices A-D.

2.4 The origin of ambiguities when adjusting the parameters of the pairing EDF to finite nuclei

Whatever the chosen form of the pairing EDF, to be predictive, its parameters have to be adjusted to some selected observables. For a given nucleus, pairing correlations depend very sensitively on details of the single-particle spectrum around the chemical potential. It is well-known, however, that even the best-performing parametrisations of any form of nuclear EDF have deficiencies with respect to predicting all details of shell structure [6, 10–14]. This is illustrated by Fig. 1 for the Skyrme NLO parameter set 1T2T(0.80) (also known as SLy7*). The calculation is done with LO^{ULB} pairing parameters adjusted as explained in Sec. 4.

The upper two rows of panels of the figure show results obtained for low-lying states of odd-mass isotopes in the Sn, Pb, and Yb chains that can be interpreted as being dominantly non-collective one-quasi-particle configurations. The upper row displays experimental data for which such configuration is indicated in the ENSDF database [90], whereas the middle row displays total en-

ergies from fully self-consistent calculations of blocked 1qp configurations as described in Sec. 2.3.

In both cases, the total energies of these 1qp configurations are plotted relative to the respective ground state of each nucleus, where for the calculated 1qp states the sign of the energy indicates if in the respective false vacuum the blocked single-particle state is above (positive energy) or below (negative energy) the chemical potential. For the experimental data the sign is decided from the assumption that the energies decrease with increasing N . This might not be the case for all levels, a notable exception being the $11/2^-$ in the light Yb isotopes that is pushed up from below the chemical potential by a change in deformation. Such convention [13] for plotting the energies of the 1qp configurations has the advantage that it can be read in the same way as a spectrum of single-particle energies as a function of N .

The definition of single-particle energies is in general model dependent. In what follows, we use this notion for the eigenvalues ε_i of the single-particle Hamiltonian \hat{h} . The lower panels of Fig. 1 show for each isotopic chain the spectrum of the neutron single-particle energies ε_i from which, for easier comparison with the upper panels, the chemical potential λ_q is subtracted.

When being calculated with 1T2T(0.80), over the range of isotopes shown, the HFB ground states of even-even Sn and Pb isotopes take a spherical shape, $\beta_{20} =$

0.0, whereas the Yb take an axial prolate shape. In all cases, this is consistent with the available spectroscopic information about these isotopic chains. The calculated ground-state quadrupole deformation β_{20} of the even-even Yb isotopes slowly increases from 0.14 for $N = 86$ to 0.32 for $N = 94$ and then remains nearly constant up to $N = 106$, beyond which β_{20} slightly drops to values around 0.28. The available data [89,90] for $88 \leq N \leq 106$ have a very similar trend. In the calculations, the light Yb isotopes up to about $N = 92$ are quite γ -soft, however, such that a single 1qp configuration might not capture well the structure of the bandheads of these nuclei. Because of the blocked quasiparticle and the polarisation it induces, none of odd-mass Sn and Pb isotopes can remain strictly spherical, but in all cases discussed here the deformation of the self-consistent 1qp configurations remains close to the one of the adjacent even-even nuclei.

The blocked quasiparticle configuration of lowest total energy does not necessarily correspond to the single-particle level ε_i closest to the chemical potential λ_q . When there are near-degenerate configurations, the lowest one is determined by the balance between distance of the dominant single-particle level from λ_q , the size of the dominant matrix elements of Δ_{ij} , and the size of polarisation effects induced by the blocked quasiparticle. Also, because of these polarisation and self-consistency effects when minimising the total energy, each 1qp configuration in a given nucleus adopts a slightly different deformation. This effect tends to compress the spectrum obtained from total energies that in the end differs significantly from the spectrum of eigenvalues E_k of the HFB Hamiltonian \mathcal{H} in the false vacuum, that in turn also differs from the spectrum of single-particle energies ε_i .

When comparing the calculated spectra of total energy differences between different states of odd nuclei with experimental data, it is evident that there are significant deviations concerning the relative distance of levels. These deviations between the total energies can be attributed to systematic deficiencies of the single-particle spectra. For the Sn chain, it can be deduced that the $1h_{11/2-}$ intruder level should be much closer to the normal-parity levels, and also that the relative distances between the normal-parity levels should be slightly different, in particular the $2d_{5/2+}$ should be higher up. Similar discrepancies, although somewhat less dramatic, are found for Pb isotopes. What is common for the Sn and Pb chains is that the calculated spectrum is much to spread out for isotopes just above the spherical shell closures, i.e. $N = 50$ and 82 for Sn and $N = 126$ for Pb. In fact, for Pb isotopes with $N > 126$, the single-particle energies $\varepsilon_i - \lambda_n$ of

the $3d_{5/2+}$ and $1j_{15/2-}$ shells above the $N = 126$ gap remain outside the energy interval shown, taking the values of 1.7 and 1.6 MeV, respectively for the Pb isotope with $N = 140$.

For the deformed Yb isotopes, for which the 1qp configurations constitute the band heads of low-lying rotational bands, only a small subset of the possible bands has been identified for most odd-mass isotopes, which complicates the comparison with theory. The somewhat erratic behaviour of the relative distance between the calculated total energies of the lightest isotopes is a consequence of their rapidly changing deformation, from about $\beta_2 \simeq 0.17$ for $N = 87$ to $\beta_2 \simeq 0.31$ for $N = 93$. The calculations with 1T2T(0.80) predict several quite pronounced deformed neutron shell closures at $N = 100, 104$ and 112 that are indicated in Fig. 1. Experimental data for two-neutron separation energies rather point towards deformed shell effects at $N = 98$ and $N = 104$ instead. The sparse data for the heavier Yb isotopes also point towards some structural change at about $N \simeq 108$.

For the majority of odd-mass isotopes displayed on Fig. 1 neither the angular momentum of the ground-state nor the bunching of low-lying 1qp states is always well described, which is a common feature of all parametrisations of all types of nuclear EDF models. Although these often give a fair description of global features of shell structure and predict the configuration with correct J to be in general one of the low-lying states [10], the many deviations in detail can have consequences when the fit protocol of the pairing interaction relies on the odd-even mass staggering of masses or average pairing matrix elements. First, the matrix elements of Δ_{ij} depend on the spatial wave function, so blocking the incorrect configuration implies that the matrix elements that make the largest difference have not the correct size. In addition, levels with incorrect distance from the chemical potential will in general not have the correct occupation numbers. In general, the parameters of the pairing EDF will partially absorb these imperfections when adjusting them to properties of finite nuclei, which then leads to problems when extrapolating the such adjusted pairing EDF to other nuclei or to other phenomena.

We found similar deviations from data for SLy4, 1T2T(0.70), 1T2T(0.85), and SN2LO1, and on general grounds this can be expected for virtually all existing parametrisations of the nuclear EDF, but there can be quite large differences in performance for a given level in a given nucleus.

3 HFB study of paired homogeneous infinite nuclear matter

As a robust alternative to calculations of finite nuclei, there also is the possibility to adjust the parameters of the pairing EDF to properties of the model system of homogeneous infinite nuclear matter.

3.1 Historical remarks

After first perturbative calculations of the pairing properties of INM [94, 95], to the best of our knowledge, the first full self-consistent solution of the HFB equation for INM taking into account the feedback of pairing correlations onto the mean fields was reported in Ref. [96]. Solving the simpler BCS pairing problem of INM for a fixed single-particle spectrum nevertheless remains common practice. Over the years, there have been numerous BCS and HFB studies using bare NN interactions such as Refs. [4, 97–102], which, however, in the context of a modelling from first principles is only the first step towards more complete microscopic calculations of paired INM that also take into account other correlations [103–108].

The pairing properties of INM have also been studied for the widely-used effective non-relativistic EDFs of Gogny [109, 110], M3Y [110], and Skyrme [111, 112] type, as well as for relativistic mean-field models [113, 114]. There also are numerous studies of the pairing properties in INM obtained with specifically tailored phenomenological pairing interactions [15–17, 21–23] that use one of these EDFs as the ph interaction to determine the underlying mean fields of the nucleons, which is also what will be done here.

3.2 HFB calculations of INM

Our study is limited to homogeneous non-polarised INM, which is completely characterised by two parameters. These are the total density ρ and the isospin asymmetry I , which are related to proton and neutron densities through

$$\rho = \rho_n + \rho_p = D_n^{1,1} + D_p^{1,1}, \quad (13)$$

$$I = \frac{\rho_n - \rho_p}{\rho_n + \rho_p} = \frac{D_n^{1,1} - D_p^{1,1}}{D_n^{1,1} + D_p^{1,1}}, \quad (14)$$

or

$$\rho_n = D_n^{1,1} = \frac{1}{2}(1 + I)\rho, \quad (15)$$

$$\rho_p = D_p^{1,1} = \frac{1}{2}(1 - I)\rho. \quad (16)$$

Throughout this paper, we make the distinction where the densities ρ_p , ρ_n , and ρ in traditional notation represent the targeted parameters of INM, whereas the local densities $D_q^{A,B}$ in the notation of Ref. [34] are those that enter the Skyrme EDF and that are numerically calculated. With these symmetries, the HFB equations [1, 47, 115]

$$\begin{pmatrix} h - \lambda & \Delta \\ -\Delta^* & -h^* + \lambda \end{pmatrix} \begin{pmatrix} U \\ V \end{pmatrix} = E \begin{pmatrix} U \\ V \end{pmatrix} \quad (17)$$

can be mapped onto a set of pairwise coupled equations for given mean fields h and Δ and momenta, which enormously simplifies the numerical solution of the problem compared to the treatment of finite nuclei. Contrary to the case of finite nuclei, in INM calculations the chemical potential λ_q that enters the HFB equation (17) as a Lagrange parameter is used to adjust the density ρ_q , and not an average particle number. The necessary steps to solve the HFB equations for 1S_0 pairing correlations in the context of Skyrme EDFs are detailed in the Appendices. We outline here just the specificities of some of the objects that are relevant for the further discussion.

In a plane-wave basis the single-particle Hamiltonian h of INM that enters Eq. (17) is diagonal, and for a N2LO Skyrme EDF its eigenvalues $\varepsilon_{\mathbf{k}\sigma q}$ that we call single-particle energies are given by

$$\begin{aligned} \varepsilon_{\mathbf{k}\sigma q} = & \left(\frac{\hbar^2}{2m} + F_q^{(\nabla, \nabla)} \right) \mathbf{k}^2 + F_q^{1,1} \\ & + \sum_{\mu} F_{q, \mu\mu}^{\nabla, \nabla} k_{\mu}^2 + F_q^{\Delta, \Delta} \mathbf{k}^4, \end{aligned} \quad (18)$$

see Appendix B.4 for details. In the presence of N2LO terms, this expression cannot be rewritten as the sum of a kinetic term with k -dependent effective mass and a k -independent potential, see Appendix B.5.

As an alternative to ρ_p and ρ_n , INM can also be characterised in terms of the Fermi momenta¹ $k_{F,q}$ of protons and neutrons in a non-paired Fermi gas that has the same density ρ and asymmetry I as the paired INM. Because of the well-known relation

$$k_{F,q} = (3\pi^2 \rho_q)^{1/3}, \quad (19)$$

for a non-interacting Fermi gas [116, 117] that also applies to the HF solution of INM, $k_{F,q}$ can be used as a proxy for the density ρ_q . At the corresponding Fermi energy $\varepsilon_{F,q}$, the occupation probabilities of an interacting Fermi gas sharply fall from one to zero.

¹Strictly speaking, $k_{F,q}$ is a wave vector and not a momentum that would be $p_{F,q} = \hbar k_{F,q}$, but we will follow here the usual practice in the low-energy nuclear physics literature.

By contrast, in the paired phase obtained from a HFB calculation, the occupation numbers $v_{k,q}^2$ have a smooth distribution that falls off from one to zero over a range of single-particle energies characterised by the gap Δ_q , with the occupation number taking the value 1/2 at the chemical potential λ_q . For the discussion of our results, we found it useful to define the momentum $k_{\lambda,q}$ for which the single-particle energy defined through Eq. (18) equals the chemical potential

$$\varepsilon_{k_{\lambda,q}\sigma q} = \lambda_q, \quad (20)$$

such that $v_{k_{\lambda,q},q}^2 = u_{k_{\lambda,q},q}^2 = 1/2$. Not all authors seem to make such distinction, though. To avoid any confusion, we propose to use different symbols for these two quantities.

We note that the definition of $k_{\lambda,q}$ through Eq. (20) can also apply to the case of solutions with $\lambda_q < F_q^{1,1}$ that for some parametrisations of the effective $T = 1$ pairing EDF can be found at very low density ρ [118]. An example will be discussed in Sec. 3.3.

Other characteristic properties of paired INM are the values of the matrix elements Δ_k for the nucleon species q at either $k_{F,q}$ or $k_{\lambda,q}$ that will be denoted as $\Delta_q(k_{F,q})$ and $\Delta_q(k_{\lambda,q})$, respectively.

We recall that the reason why INM is usually discussed in terms of characteristic momenta instead of characteristic energies (such as the chemical potential) is that, for INM, momentum is a quantum number of the plane wave states that is independent on the specific solution of the HFB calculation. This has to be contrasted with $\varepsilon_{F,q}$ and λ_q that are multivariate functions of ρ and I whose precise form is determined by the parametrisation of the EDF.

It is to be noted that in the literature on paired condensed matter $\varepsilon_{F,q}$ usually represents the Fermi energy of a *non-interacting* Fermi gas,² $\varepsilon_{F,q} = \hbar^2 k_{F,q}^2 / (2m) = \hbar^2 (3\pi\rho_q)^{2/3} / (2m)$ [119]. For the discussion of nuclear matter calculated in the HFB approach, this is not very practical as nucleons then adopt an effective mass that is usually significantly different from the bare mass, and also are subject to the mean fields. In the nuclear physics literature, one sometimes finds a hybrid convention where the effective mass at the Fermi momentum is used to calculate the single-particle spectrum and therewith $\varepsilon_{F,q}$, but all other terms in the single-particle Hamiltonian (including a possible k dependence of the effective mass and single-particle potential) are neglected. For Skyrme NLO EDFs doing so just leads to a global constant shift of the single-particle energies in INM. But for higher-order Skyrme

²The same convention is also sometimes used in nuclear physics papers, examples being Refs. [68–72, 76].

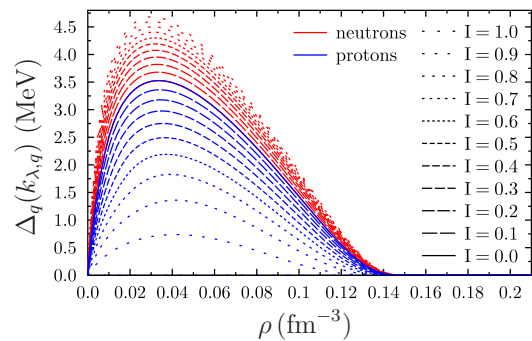


Fig. 2 Gap $\Delta_q(k_{\lambda,q})$ of protons and neutrons at the respective $k_{\lambda,q}$ in paired INM calculated with SLy4+ULB at asymmetries between $I = 0$ (symmetric matter) and $I = 1$ (neutron matter) in steps of 0.1 as a function of the total density ρ .

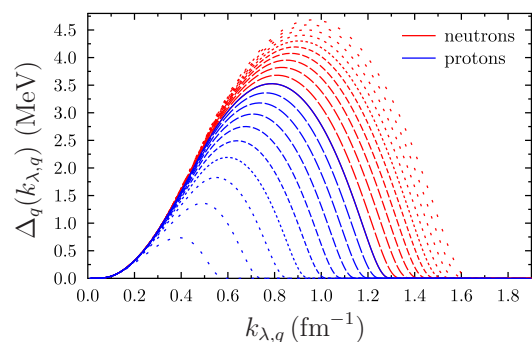


Fig. 3 Same as Fig. 2, but as a function of the $k_{\lambda,q}$ of the respective nucleon species.

EDFs and EDFs with finite-range interactions for which the effective mass and the effective potential are k dependent, the single-particle spectrum in such reference Fermi gas is not the same as the one obtained in a full HF calculation. First, the change of the effective mass with k is missing, and second, the effective mass does in general not absorb the entire k -dependence of the single-particle Hamiltonian. This is sketched for N2LO Skyrme EDFs in Appendix B.5.

3.3 Pairing correlations from SLy4 + ULB

In this subsection, we illustrate some properties of pairing correlations in INM obtained with the SLy4+ULB parametrisation as defined in Sec. 2.2. Figures 2 and 3 display the pairing gap $\Delta_q(k_{\lambda,q})$ of protons and neutrons at the respective $k_{\lambda,q}$ as a function of total density for asymmetries ranging from $I = 0$ (symmetric matter) to $I = 1$ (neutron matter), either as a function of ρ or as a function of $k_{\lambda,q}$. Plotting these as either a function of ρ or of $k_{\lambda,q}$ highlights different aspects of the curves.

For this parametrisation of the EDF, pairing correlations are only found at sub-saturation density, which

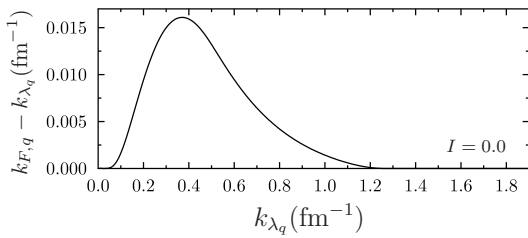


Fig. 4 Difference between $k_{F,q}$ and $k_{\lambda,q}$ in symmetric INM calculated with SLy4+ULB.

is expected for a parametrisation of the pairing EDF that by construction is of pure surface character and therefore necessarily vanishes at $\rho_{\text{ref}} = 0.16 \text{ fm}^{-3}$. That the pairing becomes weak around saturation density is however a common feature of all more microscopic calculations of the pairing gap in INM [2, 4, 97–108] and was the original motivation to construct effective pairing interactions of surface character [28, 68–71].

For symmetric matter ($I = 0$), the gaps of protons and neutrons are equal, whereas the proton gap is trivially identical to zero in neutron matter ($I = 1$). For this parametrisation, the neutron pairing becomes stronger in neutron-rich matter, whereas proton pairing becomes weaker.

There is no direct empirical information on the pairing gap in INM at any density. BCS and HFB calculations with bare two-nucleon interactions give all very similar predictions for the density dependence of the 1S_0 pairing gap [4, 97–101] with a maximum value of about 3 MeV for both symmetric and pure neutron matter. There are only small differences in detail concerning the absolute and relative size. Adding N2LO three-body forces to N3LO two-body potentials from chiral effective field theory reduces the BCS gap in neutron matter by a few 100 keV [102]. In more refined microscopic calculations based on bare interactions, the pairing gap in INM is however significantly modified by correlations. But unfortunately, the different methods for the many-body treatment – that often are also used with a different Hamiltonian – each lead to significantly differing predictions [103–108]. Almost all of these calculations only address neutron matter, and find that the position of the peak of the gap is shifted to values between $k = 0.6$ and 0.9 fm^{-1} with a maximum value between 1.0 and 2.5 MeV.

To have an effective description of the fully correlated system through a simple HFB calculation, the impact of correlations on the pairing gap has to be mimicked by the EDF. When aiming at the efficient EDF description of homogeneous INM, then one should of course compare with the gap obtained from the most complete microscopic calculation, which is what is done

in Refs. [23, 58–62]. However, if the aim is to use INM as a proxy for pairing correlations that reproduce experimental results for finite nuclei within an HFB calculation – which is what we aim at – then the gap from a microscopic calculation might not be a useful reference. Indeed, as we will illustrate in Sec. 5, a LO pairing EDF that yields the same HFB gaps in INM as SLy4+ULB gives a very satisfying description of pairing correlations in heavy nuclei.

In spite of the difficulty to identify a reliable reference, the significant increase of the HFB gap from SLy4+ULB when going from symmetric to neutron matter found in Figs. 2 and 3 is probably not very realistic. This possibly points to the need to augment the pairing EDF of Eq. (1) by a dependence on the isovector density as done in Refs. [23, 54–57]. This question, however, cannot be decoupled from the evolution of the effective masses of protons and neutrons in asymmetric matter, for which microscopic calculations indicate that for SLy4 they split the wrong way round [120].

Figure 4 displays the difference between $k_{F,q}$ and $k_{\lambda,q}$ in symmetric matter. In the absence of pairing correlations, both are identical by construction. In the domain where a paired solution of the HFB equations is found, the difference remains very small compared to their absolute size.

Figure 5 displays the matrix elements Δ_k entering the HFB equations and the product of the resulting occupation amplitudes $u_k v_k$ in symmetric matter as a function of k at a few representative densities, while Fig. 6 shows Δ_k , $u_k v_k$, and the occupation probabilities v_k^2 as a function of the distance of the single-particle energy ε_k to the chemical potential λ_q .

For a LO pairing EDF obtained from a gradientless contact generator (2) such as the ULB pairing EDF, without a cutoff the values of Δ_k of a given nucleon species in INM would take the same constant value for all k that then would be equal to the gap $\Delta_q(k_{\lambda,q})$ plotted in Figs. 2 and 3. The k -dependence of Δ_k that can be seen in Fig. 5 is the consequence of the cutoff (8) that acts above and below the chemical potential λ_q . Because of the quadratic dependence of the single-particle energies ε_k on k and the very different potential depth at different densities, the curves for Δ_k appear to be distorted when being plotted as a function of k in Fig. 5. By contrast, when plotted as a function of $\varepsilon_k - \lambda_q$ as in Fig. 6, these curves are all equally centred at zero.

The constancy of Δ_k inside the pairing window implies that when using a gradientless pairing EDF like the one of Eq. (1), in the usual BCS pairing regime of INM the values of $\Delta_q(k_{F,q})$ and $\Delta_q(k_{\lambda,q})$ are in general equal, in spite of $k_{\lambda,q} \neq k_{F,q}$. For more elaborate pairing EDFs that yield a k -dependence of Δ_k , such as

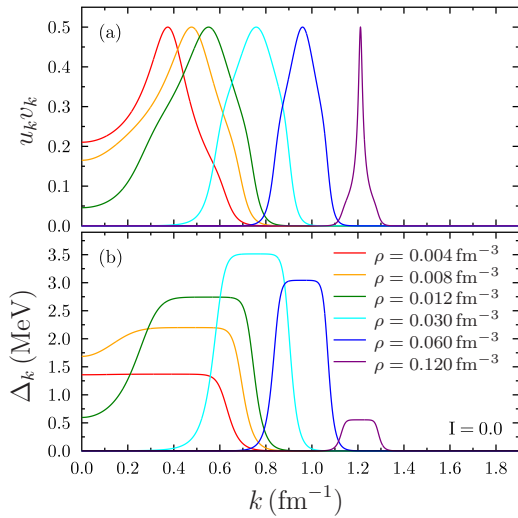


Fig. 5 Product of occupation amplitudes $u_k v_k$ (panel a) and matrix elements Δ_k (panel b) and as a function of k in a calculation with SLy4+ULB in symmetric INM at the densities as indicated.

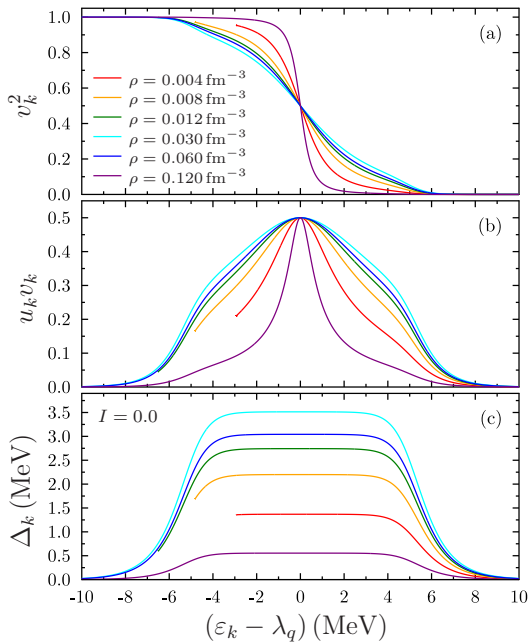


Fig. 6 Occupation probabilities v_k^2 (panel a), product of occupation amplitudes $u_k v_k$ (panel b), and matrix elements Δ_k (panel c) as a function of $\varepsilon_k - \lambda_q$ in a calculation with SLy4+ULB in symmetric INM at the densities as indicated.

the ones obtained from contact interactions with gradient terms or from a finite-range generator, the situation will of course be different.

At $\rho = 0.004 \text{ fm}^{-3}$, with $F_q^{1,1} = -4.447 \text{ MeV}$ the potential is so shallow that the entire range of the single-particle spectrum up to the chemical potential $\lambda_q = -1.520 \text{ MeV}$ falls into the pairing window, which explains why the corresponding curve in Fig. 6 starts

only in the middle of the plot. At $\rho = 0.008 \text{ fm}^{-3}$, the distance between $F_q^{1,1} = -8.125 \text{ MeV}$ and $\lambda_q = -3.301 \text{ MeV}$ is just large enough so that the lowest single-particle levels are located where the cutoff starts to fall off, whereas at $\rho = 0.012 \text{ fm}^{-3}$, single-particle levels at $k = 0$ are already in the tail of the cutoff. At higher density, the distance between the bottom of the potential $F_q^{1,1}$ and the chemical potential quickly grows to several tens of MeV such that for low-lying single-particle levels the cutoff puts the values of Δ_k to zero.

The occupation $v_{k,q}^2$ of a single-particle level at the chemical potential $\varepsilon_{k,q} = \lambda_q$ is $1/2$, see Eq. (A.44). If the pairing gap Δ_k remains constant over this interval, as is the case for the LO pairing EDF, then it follows from the same equation that the energy range over which the occupations fall from 0.9 to 0.1 equals $8/3$ times the value of $\Delta_q(k_{\lambda,q})$, which thereby directly indicates the magnitude of pairing correlations.

Because $\Delta_k = 0$ implies $v_k = 1$ and $u_k = 0$ for levels below the chemical potential and $v_k = 0$ and $u_k = 1$ for levels above the chemical potential, see Eqs. (A.44) and (A.45), the distribution of $u_k v_k$ cannot exceed the range over which the Δ_k are non-zero. The cutoff used here has been tailored for calculations of finite nuclei, for which the pairing gap rarely exceeds 1.5 MeV . The gap in INM, however, can become much larger, which then leads to the shoulder in the distribution of the $u_k v_k$ at about $\lambda_q \pm 5 \text{ MeV}$, beyond which the $u_k v_k$ fall off very quickly.

Panel (b) of Fig. 7 displays the energy per particle E/A as a function of total density for asymmetries ranging from $I = 0$ (symmetric matter) to $I = 1$ (neutron matter) as a function $k_{\lambda,n}$. Panel (a) of the same figure displays the pairing correlation energy per particle, i.e. the gain in E/A when running a HFB calculation instead of a HF calculation,

$$\frac{E_{\text{corr}}}{A} = \frac{E_{\text{tot}}^{\text{HFB}}}{A} - \frac{E_{\text{tot}}^{\text{HF}}}{A} \quad (21)$$

at either the same ρ and I , or at $k_{\lambda,q} = k_{F,q}$. These two choices for the HF reference calculation are not equivalent because for paired states there is no relation between $k_{\lambda,q}$ and the nucleonic densities. It is clearly the former of these two choices that should be made.

As for this parametrisation the pairing correlations disappear at saturation density in both symmetric and isospin-asymmetric matter, taking into account pairing correlations cannot affect the usual nuclear matter properties of SLy4 at saturation density. But even when using a pairing EDF for which there still is a paired solution at saturation density, the effect of pairing on all widely-discussed INM properties at the saturation

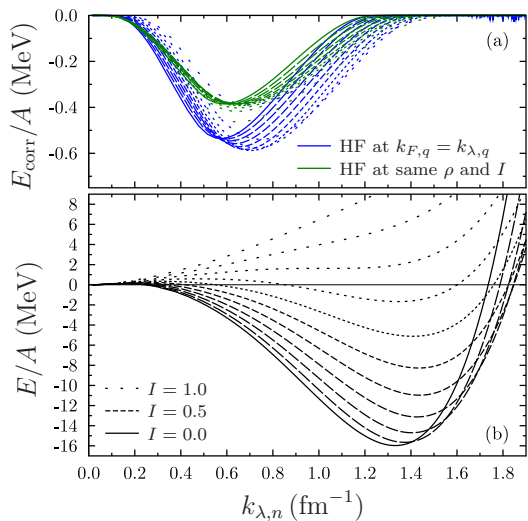


Fig. 7 Panel (b): Energy per particle E/A in paired INM calculated with SLy4+ULB at asymmetries between $I = 0$ (symmetric matter) and $I = 1$ (neutron matter) in steps of 0.1 plotted as a function of $k_{\lambda,n}$, where linestyle are the same as in Fig. 2. Panel (a): corresponding pairing correlation energy per particle E_{corr}/A , i.e. the difference in E/A between a HFB and a HF calculation, calculated either at same ρ and I or at $k_{\lambda,q} = k_{F,q}$.

point remains small, see Ref. [121]. By contrast, pairing correlations can significantly affect the energy per particle of homogeneous INM at sub-saturation density, in particular in the region where INM becomes bound at small asymmetries, see also Ref. [57]. Indeed, for the ULB pairing interaction the pairing correlation energy per particle peaks at densities at which the total binding energy per particle in paired INM is of comparable size. The detailed behaviour might of course sensitively depend on the choice of the EDF and its parametrisation, a few examples for which just the parameters of the pairing EDF (1) are modified are discussed in Sec. 3.4.

We have to recall, however, that, because of the so-called “spinodal” finite-size instability [42, 122], there actually is no stable low-density phase of homogeneous INM symmetric matter or matter at small asymmetry. HFB calculations of such matter at sub-saturation densities serve as a laboratory for the controlled analysis of pairing interactions, but have no direct application to a system that could be found in nature.

3.4 Role of the parameters in the pairing EDF

As the next step, we will compare the role of the parameters V_0 , η and σ of the LO pairing EDF (6) for the pairing correlations found in finite nuclei and infinite matter.

Table 1 Parameters of the pairing EDF (1) with varied parameter η at fixed $\sigma = 1.0$ that with SLy4 yield the same average neutron gap $\langle uv\Delta \rangle_n$ for ^{120}Sn as the original ULB parametrisation with $\eta = 1.0$.

	V_0 (MeV fm ³)	η	σ
surface	-1250.0	1.00	1.0
	-873.2	0.75	1.0
mixed	-670.0	0.50	1.0
	-543.2	0.25	1.0
volume	-456.7	0.00	1.0

We start with the analysis of the role of the parameter η that regulates between the “surface” ($\eta = 1$) and “volume” ($\eta = 0$) character of the pair potential. In order to have comparable results, we constructed a series of parametrisations with decreasing η that together with SLy4 give the same average neutron pairing gap as defined through Eq. (10) of $\langle uv\Delta \rangle_n = 1.924$ MeV for ^{120}Sn as the original ULB parametrisation of the pairing EDF. The same parametrisation (8) of the cutoff is used in all cases, the contribution (3) of the pairing EDF to the normal potentials $F_q^{1,1}(\mathbf{r})$ is kept, and all calculations of ^{120}Sn are done with the pairing stabilisation (9) at fixed $\sigma = 1$ using the spherical HFB code mentioned above. The resulting parameters are listed in Table 1. With decreasing η , the overall pairing strength becomes much smaller. We recall that for fixed η and σ the size of V_0 inversely scales with the pairing cutoff and can become much smaller when renormalising the pairing strength to a larger pairing window.

Figure 8 displays the pairing potential of neutrons $\tilde{F}_n^{1,1}(\mathbf{r})$, the contribution of the pairing EDF to the normal potential $F_n^{1,1}(\mathbf{r})$ of neutrons, the pair density $\tilde{D}_n^{1,1}(\mathbf{r})$ of neutrons as well as the neutron and total normal densities, $D_n^{1,1}(\mathbf{r})$ and $D_0^{1,1}(\mathbf{r})$, for ^{120}Sn calculated with SLy4 and all parametrisations of the pairing EDF defined in Table 1.

In the case of pure volume pairing ($\eta = 0$), $\tilde{F}_n^{1,1}(r)$ is simply proportional to the neutron pair density $\tilde{D}_n^{1,1}(r)$ and the contribution of the pairing EDF to the normal potential (3) vanishes. By contrast, in the case of surface pairing ($\eta = 1$), the contribution of the pairing EDF to the normal potential of neutrons is proportional to the square of the neutron pair density $\tilde{D}_n^{1,1}(r)$. Note that for an attractive pairing interaction of the form (1), its contribution to the normal potentials (3) is strictly positive, i.e. repulsive.

The pairing potential $\tilde{F}_n^{1,1}(r)$ of neutrons illustrates the expected change in radial dependence when going from $\eta = 1$ to $\eta = 0$: For $\eta = 1$, the pair potential prac-

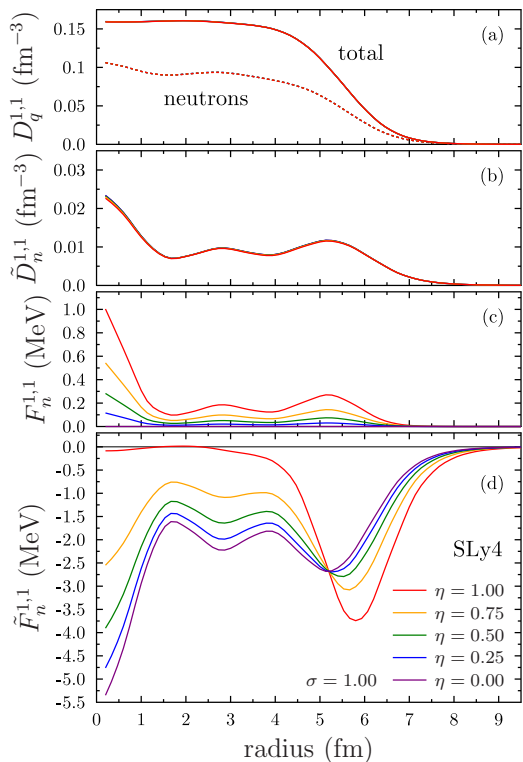


Fig. 8 Normal density of neutrons and nucleons (panel a), pair density of neutrons (panel b), contribution of the pairing EDF to the normal potential of neutrons (panel c), and pair potential of neutrons (panel d) for ^{120}Sn calculated with SLy4 and five variants of the pairing EDF (1) with different value of the parameter η that regulates between surface and volume character of the EDF. The red curve represents the original ULB parametrisation.

tically vanishes in the nuclear interior and has a peak at the nuclear surface where the total density falls to zero. We recall that because of the volume element $4\pi dr r^2$, a pair potential peaked inside the nuclear volume has to be larger than a surface-peaked one in order to give the same matrix element for a single-particle state that is spread over the entire nucleus.

The single-particle orbits, however, are not equally spread over the nucleus; therefore surface-peaked and volume-type pair potentials will in general lead to different individual matrix elements Δ_{km} [50]. Within a given major shell, a surface-peaked pair potential typically gives larger Δ_{km} between high- ℓ single-particle states, whereas a volume-type pair potential gives larger Δ_{km} between low- ℓ states.

Still, as long as all pairing parameter sets yield the same average neutron gap $\langle uv\Delta \rangle_n$ for ^{120}Sn , the normal and pair density distributions of this nucleus are nearly identical for all values of η , although there are small differences that cannot be resolved on Fig. 8 originating from slightly different distributions of the occupation

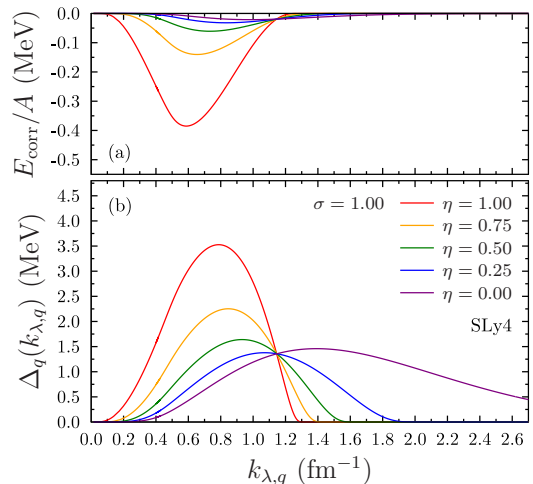


Fig. 9 Gap $\Delta_q(k_{\lambda,q})$ (panel b) and pairing correlation energy per particle E_{corr}/A calculated as the difference in E/A between a HFB and a HF calculation at same ρ and I (panel a), as a function of $k_{\lambda,q}$ for symmetric INM calculated with SLy4 and the same five variants of the pairing EDF (1) with different value of the parameter η as in Fig. 8, using the same colour code.

amplitudes u_k and v_k in each case. Similar results have been obtained before in Refs. [123, 124].

While the parametrisations of Table 1 all give the same average neutron pairing gap for ^{120}Sn , changing the form factor of the pairing EDF from surface to volume character dramatically changes the pairing gaps in INM, see Fig. 9. The width of the curve representing $\Delta_q(k_{\lambda,q})$, its value at the maximum, and also the position of the maximum all change.

With decreasing η , the peak becomes wider, and its maximum is shifted towards larger $k_{\lambda,q}$, which simply follows from the effective pairing strength changing from being zero at saturation density for pure surface pairing ($\eta = 1$) to being independent on the density for pure volume pairing ($\eta = 0$). The highest $k_{\lambda,q}$ on Fig. 9 corresponds to $\rho \simeq 0.63 \text{ fm}^{-3}$, i.e. about four times saturation density. For pure volume pairing, there are still pairing correlations found even at $\rho \simeq 4 \text{ fm}^{-3}$, which is about 25 times saturation density. Curiously, for an unidentified reason all curves cross at about $k_{\lambda,q} \simeq 1.145 \text{ fm}^{-1}$, which corresponds to $\rho \simeq 0.1015 \text{ fm}^{-3} \simeq 0.63 \rho_{\text{sat}}$ with a value of $\Delta_q(k_{\lambda,q}) \simeq 1.35 \text{ MeV}$. In any event, Fig. 9 confirms that producing the same density dependence of $\Delta_q(k_{\lambda,q})$ as found in microscopic calculations of paired INM with an LO contact pairing EDF requires surface-dominated pairing with a value of η near one.

The pairing correlation energy per particle E_{corr}/A also dramatically changes when going from surface to volume pairing, see panel (a) of Fig. 9. As already observed on Fig. 7, for surface pairing, $\eta = 1$, it might

Table 2 Parameters of the pairing EDF (1) with varied power of the density dependence σ for surface pairing with fixed $\eta = 1$ that with SLy4 yield the same average neutron gap $\langle uv\Delta \rangle_n$ for ^{120}Sn as the original ULB parametrisation with $\sigma = 1.0$.

V_0 (MeV fm ³)	η	σ
-1250.0	1.0	1.0
-1333.9	1.0	0.9
-1438.8	1.0	0.8
-1573.7	1.0	0.7
-1753.7	1.0	0.6
-2005.7	1.0	0.5
-2383.9	1.0	0.4
-3014.4	1.0	0.3
-4275.6	1.0	0.2

be as large as 0.4 MeV/A. Decreasing η , however, the pairing correlation energy also dramatically decreases. For pure volume pairing, $\eta = 0$, it does not exceed a few tens of keV at any density.

Instead of varying η at fixed $\sigma = 1$, it is also illustrative to vary σ at fixed $\eta = 1$. Again, we generated a series of parametrisations of the LO pairing EDF (1) that together with SLy4 give the same average pairing

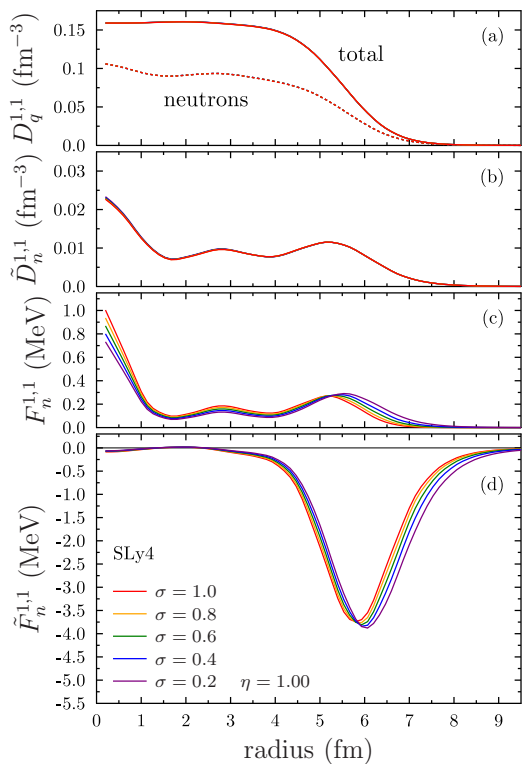


Fig. 10 Same as Fig. 8, but for five variants of the LO pairing EDF with varied power σ of the density dependence from Table 2.

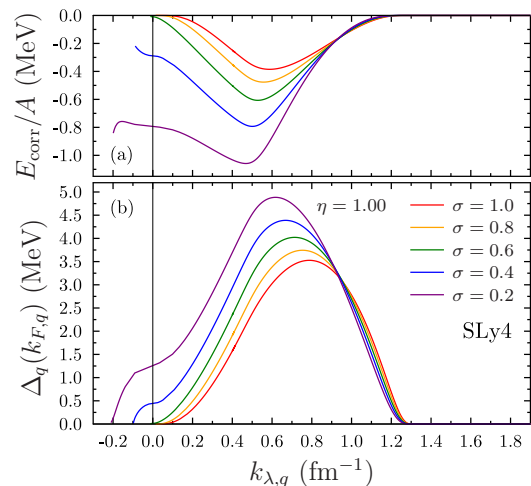


Fig. 11 Gap $\Delta_q(k_{F,q})$ (panel b) and pairing correlation energy per particle E_{corr}/A (panel a) as a function of $k_{\lambda,q}$ for symmetric INM calculated with SLy4 and the same five variants of the pairing EDF (1) with systematically varied power σ of the density dependence used to prepare Fig. 10. Negative values of $k_{\lambda,q}$ represent the imaginary solutions of Eq. (20) that correspond to a chemical potential λ_q below the physical single-particle spectrum that can be found in a Bose-Einstein condensate (see text).

gap of $\langle uv\Delta \rangle_n = 1.924$ MeV for ^{120}Sn as the original ULB parametrisation of the LO pairing EDF. The resulting parameters are listed in Table 2.

Figure 10 displays the neutron and total density, neutron pair density, neutron pair potential, and pairing contribution to the neutron potential $F_n^{1,1}(\mathbf{r})$ of ^{120}Sn for these parameter sets in the same manner as in Fig. 8. Contrary to what was found there for the parameter sets with varying η but same σ , the parameter sets with same η but different σ not only yield very similar results for the densities $D_n^{1,1}(\mathbf{r})$ and $\tilde{D}_n^{1,1}(\mathbf{r})$, but also for the potentials $\tilde{F}_n^{1,1}(\mathbf{r})$ and $F_n^{1,1}(\mathbf{r})$. This indicates that results for well-bound nuclei like ^{120}Sn are rather insensitive to the power of the density dependence. The only visible evolution is that with smaller σ the peak of the pair potential $\tilde{F}_n^{1,1}(\mathbf{r})$ becomes a little wider and is slightly shifted towards larger radii in the nuclear surface.

The gap and pairing correlation energy per particle found with these five parameter sets for symmetric INM are displayed in Fig. 11. With decreasing σ , at low density – or equivalently small (positive) $k_{\lambda,q}$ – both the gap at $k_{\lambda,q}$ and E_{corr}/A increase to the point that one still finds a paired solution at $k_{\lambda,q} = 0$.

The structure of this kind of unusual solution at low density can be easily understood from the corresponding distribution of occupation numbers v_k^2 . Using that the canonical and HF bases are identical in INM, Fig. 12 displays v_k^2 as a function of the single-particle

energy relative to the bottom of the potential well obtained in HFB calculations with SLy4 plus the pairing parameter set with $\sigma = 0.2$ for five different densities. The single-particle state with $\varepsilon_k - F_q^{1,1} = 0$ is the lowest state in the single-particle spectrum with $k = 0$. All distributions of v_k^2 still follow (A.44), but what is different from the usual situation found for finite nuclei and paired INM is that, for $\rho \lesssim 0.007 \text{ fm}^{-3}$, they start at values of v_k^2 that are much smaller than 1. For $\rho \lesssim 0.0003 \text{ fm}^{-3}$, the occupation number at $k = 0$ is even smaller than 0.5, which implies that the chemical potential is outside of the physical single-particle spectrum, $\lambda_q < F_q^{1,1}$. In such case, the formal solutions of Eq. (20) for $k_{\lambda,q}$ become imaginary and do not represent the momentum of a single-particle state anymore. For an NLO EDF like SLy4, there are two solutions of opposite sign. We find that the negative modulus of the such obtained $k_{\lambda,q}$ is a useful quantity to plot the properties of these unusual solutions of the HFB equations, which is what is done in Fig. 11 to plot the gap and E_{corr}/A at small density. As $k_{\lambda,q}$ does not correspond to a physical state, the gap Δ_k cannot be calculated at this momentum. For this reason, Fig. 11 displays the gap at $k_{F,q}$ instead. We mention in passing that plotting $\Delta_q(k_{F,q})$ and other properties of paired INM as a function of ρ or $k_{F,q}$ instead of $k_{\lambda,q}$ completely masks the emergence of these unusual solutions as they are found only for a tiny interval of either of these two coordinates.

The kind of solution of the HFB equations for which $v_{k=0}^2$ is much smaller than 1 can be associated with the formation of a Bose-Einstein condensate (BEC), see Ref. [119] and references therein. In the case discussed here the BEC is formed of bound di-nucleons of same isospin coupled to spin zero.

In similar calculations using the bare strong NN interaction that also consider $T = 0$ pair correlations, a BEC of deuterons is found in the low-density limit of symmetric matter [125]. Di-neutrons, however, are

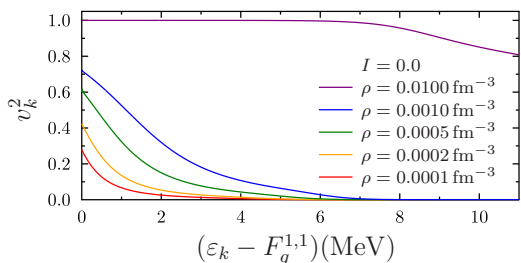


Fig. 12 Occupation numbers v_k^2 for solutions of HFB calculations of symmetric INM with SLy4 and the pairing parameter set with $\sigma = 0.2$ from Table 2 at different small total densities as indicated as a function of single-particle energy relative to the bottom of the potential well $\varepsilon_k - F_q^{1,1}$.

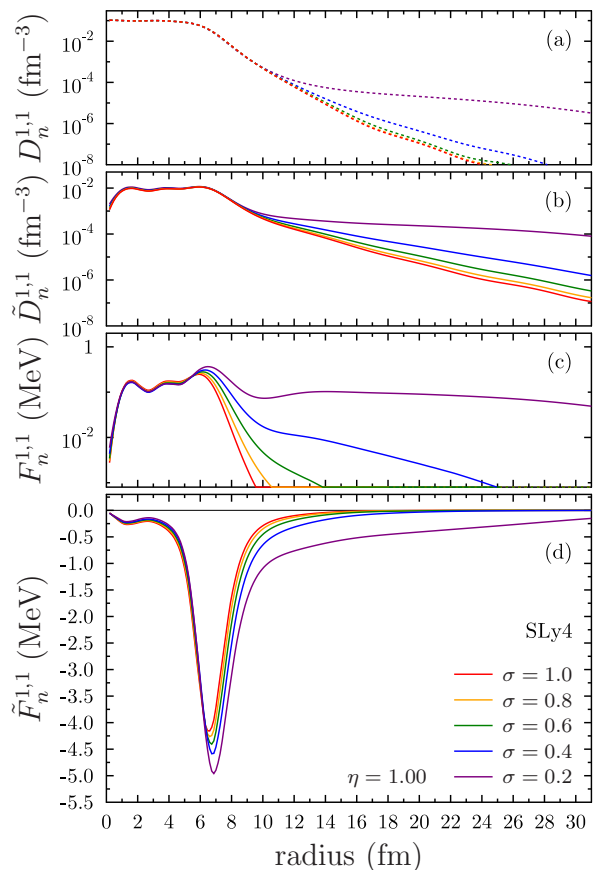


Fig. 13 Same as Fig. 10 but for the weakly-bound ^{160}Sn , plotting all densities and potentials but $\tilde{F}_n^{1,1}$ on a logarithmic scale to better resolve their behaviour at large r .

not bound in nature and therefore should not form a condensate, and neither should hypothetical di-protons without electric charge. The appearance of a BEC in the $T = 1$ channel is therefore the unambiguous signature of a nonphysical property of a given parametrisation of the nuclear EDF. However, it has been repeatedly pointed out that low-density nuclear matter can be expected to come close to a BEC-BCS crossover in the $T = 1$ channel because of the large scattering length in the 1S_0 channel in the vacuum [2–4, 20, 126–128]. The nonphysical transition to a BEC can therefore already happen when some parameter of the pairing EDF is only mildly off its physical value.

The transition from a 1S_0 BCS phase to a BEC has already been found in the study of paired INM with contact pairing interactions adjusted to reproduce gaps from microscopic models [128]. Also, a BEC of di-nucleons has been observed in the surface of finite nuclei in Refs. [129, 130] for specific values of the parameters controlling the density dependence of the LO pairing EDF (1). While there is nothing unusual in the results for ^{120}Sn displayed in Fig. 10, an instability towards a

BEC does clearly jeopardise the properties of weakly-bound nuclei. This is exemplified by Fig. 13 for ^{160}Sn , a weakly-bound nucleus for which the chemical potential λ_n of neutrons takes a value of about -630 keV for all pairing parametrisations. For the two parameter sets from Table 2 with either $\sigma = 0.4$ or 0.2 that lead to a BEC in symmetric INM in Fig. 11, the normal and pair density of neutrons develop a long queue that then feeds back to the potentials, thereby amplifying the condensation of di-neutrons at large distances. Like in INM at low density, a dilute gas of di-neutrons is forming outside of the nucleus that fills the entire size of the numerical box.

The phenomenon of a BEC of neutrons outside of a weakly-bound nucleus that can emerge in an HFB calculation with an unrealistic pairing interaction has to be clearly distinguished from the phenomenon of a spurious neutron gas that forms in HF+BCS calculations of weakly-bound nuclei even with realistic pairing interactions [85, 131]. In a full HFB calculation, when all nuclear potentials fall to zero at large distance for a system with negative chemical potential λ_q , it can be shown that all states in the canonical basis are also localised, from which then follows that all densities and pair densities are localised either [131]. In the HF+BCS approximation, this formal feature is lost [131]. By contrast, for a BEC solution of the HFB equations, the condition that the potentials fall off to zero is not satisfied anymore for the self-consistent solution as evidenced by Fig. 13.

We have to note, however, that finding or not evidence of such solution in calculations of finite nuclei sensitively depends on the numerical settings that are used, which in our case are the box size, distance between points on the mesh, and the number of single-particle states explicitly kept. In too small a basis, the long tail of the nonphysical solution might not be fully resolved. And indeed, the HFB calculations used to prepare Fig. 13 were run in a much larger box with smaller step size and keeping significantly more HF states than usually necessary to converge physical solutions with respect to the numerical representation when using the two-basis method in coordinate space. The onset of signatures of a BEC in finite nuclei might also depend on choices made for the pairing cutoff. The origin of finding a BEC for specific parametrisations of the nuclear EDF will be investigated elsewhere.

4 Adjusting the pairing strength of a density-dependent contact pairing interaction

4.1 General considerations

Having set up the tool to calculate the pairing gap in INM, we now come back to the question of adjusting the parameters of the pairing EDF for arbitrary parametrisations of the Skyrme ph EDF. In what follows, we will illustrate under which conditions the pairing gap in INM $\Delta_q(k_{\lambda,q})$ can be used as a proxy to adjust the parameters of the LO pairing EDF (1) in such a way that one finds very similar global trends of pairing correlations in HFB calculations of finite nuclei with any (realistic) parametrisation of the underlying Skyrme EDF.

For the specific simple LO form of EDF (1), all terms contribute to the gap in INM. To be predictive, the adjustment protocol has to rely on a reference calculation for the pairing gap in INM with an effective interaction that well describes pairing correlations in finite nuclei. This reference calculation has to be made with an effective interaction that has no (dominant) terms that are only active in finite nuclei. Generalisations to cases where the target EDF and possibly also the reference EDF contains terms that are only active in finite nuclei are possible, but will not be considered here. Also, in the absence of an explicit dependence on isospin of the LO pairing EDF (1), we only consider symmetric INM. Again, generalisations are possible, but would require a reference calculation with a realistic isospin dependence.

We tested several possibilities for such reference calculations, two of which will be discussed here. The discussion of Figs. 9 and 11 has already made it evident that adjusting the pairing strength to $\Delta_q(k_{\lambda,q})$ at just one density cannot be sufficient. Instead, the full density-dependence, or, equivalently, the full $k_{\lambda,q}$ dependence, of the gap has to be used as pseudo-data in the parameter adjustment, as each of the three parameters of the LO EDF controls a different aspect of this curve.

For reasons that will become clear in what follows, we could not identify a reference calculation for asymmetric INM of which we can be sure to be predictive for asymmetric nuclei and which can be expected to be reproducible with a LO pairing EDF even when including an isovector dependence, which motivated us to stick to the standard form of Eq. (1). This does, however, not mean that after a parameter adjustment that leads to the same gaps in symmetric matter all parameter sets will also give the same predictions for asymmetric matter: different parametrisations of the Skyrme ph EDF can have very different isovector effective mass, which

Table 3 Parameter sets LO^{ULB} of the LO pairing EDF (1) obtained adjusting the pairing gaps in symmetric INM obtained for the underlying particle-hole Skyrme EDF as indicated to reproduce the pairing gaps from SLy4+ULB in symmetric INM. The second column lists the isoscalar effective mass of the respective Skyrme parametrisation at the saturation point. The original SLy4+ULB values are given for comparison.

	m_0^*/m	V_0 (MeV fm ³)	η	σ
SLy4	0.695	-1250.0	1.000	1.000
1T2T(0.70)	0.700	-1250.9	1.000	0.993
1T2T(0.80)	0.800	-1267.0	1.012	0.896
1T2T(0.85)	0.850	-1275.3	1.017	0.859
SN2LO1	0.709	-1251.0	1.009	1.013

then can make a difference for the evolution of the proton and neutron pairing gaps in asymmetric matter.

4.2 Adjusting parameters to infinite nuclear matter pairing gaps from SLy4+ULB

One successful procedure that we could identify consists in adjusting the parameters of the LO pairing EDF (1) to the gaps obtained from HFB calculations of symmetric INM with SLy4+ULB as discussed in Sec. 3.3. As pseudo-data, we use the value of $\Delta_q(k_{\lambda,q})$ at 11 points between $k_{\lambda,q} = 0.2 \text{ fm}^{-1}$ and $k_{\lambda,q} = 1.2 \text{ fm}^{-1}$ in steps of 0.1 fm^{-1} . Depending on the combination of pairing parameters, for both larger and also smaller values of $k_{\lambda,q}$ there might not be a paired solution of the HFB equations, which would jeopardise the parameter adjustment. Conversely, using a smaller interval might not sufficiently fix the low- and/or high-density behaviour of the gap from the reference calculation. All gaps enter the penalty function with the same weight.

The pairing parameters resulting from such fit for the 1T2T(0.70), 1T2T(0.80), 1T2T(0.85), and SN2LO1 parameter sets described in Sec. 2.1 are listed in Table 3. Whenever possible, we will use the shorthand LO^{ULB} to refer to them in what follows. Figure 14 compares the gaps in symmetric INM obtained with these parametrisations with the results from SLy4+ULB that defined the penalty function. In all cases the SLy4+ULB gaps are very well reproduced. In general, this requires the readjustment of all three parameters of the pairing EDF. The reason for this can be easily deduced when comparing the results obtained with readjusted pairing parameters with calculations that use the original ULB pairing parameters that are also displayed with dotted lines on Fig. 14: when not readjusting the pairing parameters to the specific ph interaction, with increasing

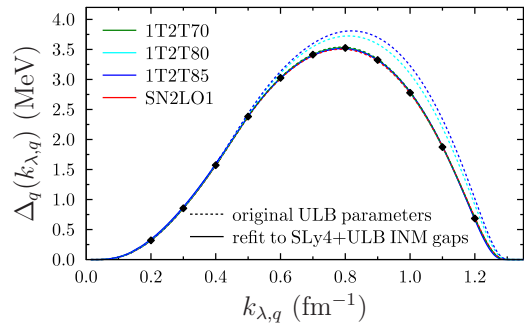


Fig. 14 Gap at $k_{\lambda,q}$ in symmetric INM for the parameter sets of the ph Skyrme EDF as indicated and LO^{ULB} pairing parameters. Markers indicate results obtained with SLy4+ULB pairing. For each Skyrme parametrisation, results obtained with two different parametrisations of the pairing EDF are shown: one where the original ULB parameters of Ref. [37] are used (dotted lines), and one where the parameters were readjusted to reproduce the SLy4+ULB gaps in symmetric INM as indicated in Table 3 (solid lines). In the latter case the calculated curves almost perfectly fall on top of each other.

effective mass the curve representing the gap becomes wider, its peak is shifted towards larger k_{λ} , and the peak value increases. As illustrated in Sec. 3.3, the width of the curve and position of the peak are controlled by η and σ , whereas V_0 mostly influences the maximum value. Therefore, the values of all three parameters have to be readjusted.

It turns out that the parameter η controlling the volume-to-surface behaviour remains almost constant near 1, whereas the power of the density dependence σ becomes significantly smaller for Skyrme parameter sets with larger effective mass. At the same time, the global strength V_0 also increases with effective mass. This might appear counter-intuitive, because larger effective mass requires weaker pairing. V_0 indeed has to be reduced when keeping $\sigma = \eta = 1$ fixed as done in Ref. [9]. However, as indicated by Table 2, reducing σ at fixed effective mass requires a substantial increase in V_0 . Combining these two trends, the reduction of σ when increasing m_0^*/m is accompanied by a mild growth of V_0 . Note that for different parameter sets of the standard Skyrme NLO EDF with identical saturation density and isoscalar effective mass m_0^*/m (and identical $\hbar^2/2m$), our adjustment procedure leads to exactly the same pairing parameters. The reason is that in that case m_0^*/m depends on only one coupling constant, which is determined by the effective mass at saturation. Indeed, evaluating Eq. (B.65) for a NLO EDF and symmetric matter, one finds for the inverse effective mass that $m/m_0^* = 1 + \frac{2m}{\hbar^2} A_{0,e}^{(2,2)} D_0^{(\nabla,\nabla)}$, such that all standard NLO parameter sets with same $2m A_{0,e}^{(2,2)}/\hbar^2$ have exactly the same density-dependence of the k -independent m_0^*/m in symmetric INM, and therefore

Table 4 Parameter sets LO^{D1S} of the LO pairing EDF (1) obtained adjusting the pairing gaps in symmetric INM obtained for the underlying particle-hole Skyrme EDF as indicated that reproduce the pairing gaps from D1S. The second column lists the isoscalar effective mass of the respective Skyrme parametrisation at the saturation point.

	m_0^*/m	V_0 (MeV fm ³)	η	σ
1T2T(0.70)	0.700	-1358.0	0.783	0.379
1T2T(0.80)	0.800	-1397.4	0.823	0.361
1T2T(0.85)	0.850	-1415.8	0.839	0.353
SN2LO1	0.709	-1334.3	0.783	0.400

exactly the same constant level density at any given ρ in symmetric matter irrespective of differences in the corresponding equation of state. Our adjustment protocol therefore reproduces the global scaling of the pairing gap with effective mass that is naively expected for the relation between the average level density of single-particle states and the pairing gap [8]. This relation was implied in many publications that used the original ULB parameters adjusted for SLy4 also for HFB calculations with SLy5, SLy6, SLy7 [35], f_0 , f_+ , f_- [120], the *TIJ* [11], SLy5* [43], the SLy5sx [82], and 1F2F(0.70), 1T2F(0.70), 1T2T(0.70) [9] that all have an effective mass of $m_0^*/m \simeq 0.7$, see for example Refs. [34, 40, 82, 132].

The connection between effective mass and pairing parameters becomes less direct when working with extended forms of the EDF. When complementing the pairing EDF with a dependence on the isovector density and adjusting the pairing gap also for asymmetric matter, the resulting parameters governing the isovector dependence of the pairing EDF would be different as these parameter sets of the Skyrme ph EDF have different isovector effective masses. Also, the above discussed feature is very specific to the widely-used standard form of the NLO EDF and neither holds for extended NLO parameter sets that are complemented with either density-dependencies of the gradient terms or three-body gradient terms, nor for parametrisations of Skyrme EDFs of higher order in gradients such as SN2LO1 for which several terms contribute to m_0^*/m , see Eq. (B.65). Still, the pairing parameters of SN2LO1 listed in Table 3 remain close to those of SLy4 and 1T2T(0.70) that have an almost identical effective mass.

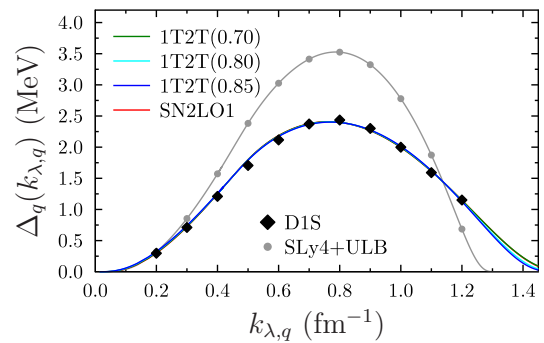


Fig. 15 Gap $\Delta_q(k_{\lambda,q})$ at the chemical potential of protons and neutrons in symmetric INM for the parameter sets of the ph Skyrme EDF as indicated combined with the respective LO^{D1S} pairing parameters as listed in Table 4. For most values of $k_{\lambda,q}$ the curves cannot be distinguished on the scale of the plot. The $\Delta_q(k_{\lambda,q})$ obtained with the original D1S parametrisation of the Gogny force taken from Ref. [118] are represented by filled black diamonds. The grey line displays the gap obtained with SLy4+ULB for comparison.

4.3 Adjusting parameters to infinite matter pairing gaps from Gogny D1S

A second possibility for a reference calculation of pairing gaps for the adjustment of the parameters of the LO pairing EDF that we explored consists in taking results from HFB calculations with the D1S parametrisation of Gogny's force [133]. Unlike the vast majority of parametrisations of the Skyrme EDF, parametrisations of the Gogny force are constructed to simultaneously describe the ph and pp parts of the EDF, and D1S is a widely-used reference pairing interaction [20, 21, 109] that reproduces well the odd-even staggering of masses [13, 134] and rotational moments of inertia [13].

The gaps in symmetric infinite matter obtained from D1S at a few selected values of the density have already been used before to constrain the parameters of the finite-range regularised pseudopotentials of Ref. [135] that, like D1S, aim at a simultaneous description of the ph and pp channels of the effective interaction.

The parameters of the LO pairing EDF are again adjusted to values of $\Delta_q(k_{\lambda,q})$ in symmetric INM calculated at 11 equidistant values for $k_{\lambda,q}$ with the code of Ref. [118]. Results of these fits are listed in Table 4, which will be referred to as LO^{D1S} parameter sets in what follows.

The INM gaps obtained with these parameter sets are compared with the original D1S results in Fig. 15. For all LO^{D1S} parameter sets the $\Delta_q(k_{\lambda,q})$ from D1S are closely reproduced at all densities. Figure 15 also displays the gaps from SLy4+ULB. Compared to these, the $k_{\lambda,q}$ dependence of $\Delta_q(k_{\lambda,q})$ obtained with D1S peaks with a much smaller maximum value of about 2.45 instead of 3.55 MeV, but at the same time falls

off at higher values of $k_{\lambda,q}$ and therefore also higher densities.

Because of the different shape of the curve representing the D1S gaps in INM, it follows from the discussion in Sec. 3.4 that the parameters of the LO pairing EDF that reproduce the gaps from D1S are quite different from those of Table 3 for the LO^{ULB} parameter sets. First, the values of η indicate that reproducing the D1S gaps necessitates a more “mixed” character with about 20% volume contribution, as could be expected from Fig. 8 for a distribution of $\Delta_q(k_{\lambda,q})$ that reaches up to saturation density. Second, with $\sigma \simeq 0.4$, reproducing the D1S gaps requires also a much more peaked density dependence than it is the case for SLy4+ULB, mainly to counterbalance the shift of the maximum of $\Delta_q(k_{\lambda,q})$ towards larger $k_{\lambda,q}$ that accompanies an increased volume character, see Figs. 8 and 11. If the LO^{D1S} parametrisations were of pure surface character as are the parameter sets used to prepare Fig. 11, they would actually produce a nonphysical transition to a BEC. As can be seen from Fig. 15, however, this is not the case for any of the underlying mean fields.

In the next section, results obtained with the two sets of parametrisations will be compared with data that are known to be sensitive to pairing correlations.

5 Pairing correlations in finite nuclei

In one way or another, pairing correlations affect all properties of nuclei. We will discuss here three observables that can be modelled with HFB calculations whose size is known to scale with the strength of the like-particle $T = 1$ pairing correlations, all of which have also already been used for the parameter adjustment of pairing EDFs

1. The odd-even staggering of nuclear masses, or, equivalently, the odd-even staggering of nuclear binding energies, which probes the effect of blocking a quasiparticle on the total energy.
2. The odd-even staggering of nuclear charge radii is sensitive to the change of the potentials in the single-particle Hamiltonian when blocking a quasiparticle [68–75].
3. The moment of inertia of collective rotational bands probes the effect of superfluidity induced by pairing correlations. In general, superfluidity decreases the rotational moment of inertia and thereby increases in-band transition energies.

The odd-even staggering of masses and charge radii is analysed for the chains of spherical Sn and Pb isotopes and the chain of deformed Yb isotopes. For even-even Yb isotopes, we also analyse the yrast rotational states.

5.1 Odd-even staggering of binding energies

5.1.1 Finite-difference pairing gaps

Odd-mass nuclei are systematically less bound than what can be inferred from the average of the binding energies of their even-even neighbours. This leads to a characteristic odd-even staggering of binding energies along isotopic and isotonic chains. The energy shift $\Delta_n(Z, N)$ between the energies of odd-mass nuclei and the curve that smoothly interpolates the total energy of even-even nuclei, denoted as $E(Z, N)$, is associated with the pairing gap. As we focus here on isotopic chains of elements with even proton number Z , for the sake of compact notation the proton number is suppressed in what follows. Approximations for this gap can be extracted from experimental and calculated total energies with finite-difference formulas [8, 38, 50, 136, 137]. Provided that $E(N)$ can be Taylor expanded around a given nucleus with $N = N_0$, the total energy $E(N)$ of the nucleus with N neutrons is given by

$$E(N) = \sum_{n=0}^{\infty} \frac{1}{n!} \left. \frac{\partial^n E(N)}{\partial N^n} \right|_{N_0} (N - N_0)^n + D(N) \quad (22)$$

where $D(N)$ is the contribution to the binding energy that is not smooth and therefore not captured by the derivatives, which in most cases is $D(N) = 0$ for even N and $D(N) = \Delta_n(Z, N)$ for odd N . This expression is the starting point for finite difference-formulas that provide averages of $D(N)$. The minimal form is a three-point gap $\Delta_n^{(3)}(N)$, that is obtained inserting Eq. (22) for $E(N \pm 1)$ into the three-point energy difference

$$\begin{aligned} \Delta_n^{(3)}(N_0) &\equiv \frac{(-1)^{N_0}}{2} \left[E(N_0 - 1) - 2E(N_0) + E(N_0 + 1) \right] \\ &= \frac{(-1)^{N_0}}{2} \left[D(N_0 - 1) - 2D(N_0) + D(N_0 + 1) \right] \\ &\quad + \frac{(-1)^{N_0}}{2} \left. \frac{\partial^2 E(N)}{\partial N^2} \right|_{N_0} + \dots \end{aligned} \quad (23)$$

For even N , $\Delta_n^{(3)}(N)$ is the average of the gap $\Delta_n(N)$ in the two adjacent odd- N isotopes minus the contributions from the derivatives, whereas for odd N , $\Delta_n^{(3)}(N)$ is the gap $\Delta_n(N)$ plus the contributions from the derivatives. The second derivative of $E(N)$, which equals one half the derivative of the two-neutron separation energy with respect to N , can be as large as a few hundred keV [38, 50]. As it contributes with opposite sign to the $\Delta_n^{(3)}(N)$ of odd and even nuclei, the second derivative produces an odd-even staggering of

the $\Delta_n^{(3)}(N)$. This can become problematic when comparing experimental $\Delta_n^{(3)}(N)$ with some theoretical estimate of the pairing gap such as the average gaps of Eqs. (10) and (12). There are two possible definitions of a four-point gap that estimate the shift between the mass surfaces of odd and even nuclei at $N \pm 1/2$ [50], which are rarely used. It has been argued in Refs. [38, 50] that a controlled extraction of $\Delta_n(N)$ is obtained through the five-point difference

$$\begin{aligned} \Delta_n^{(5)}(N_0) &\equiv -\frac{(-1)^{N_0}}{8} \left[E(N_0 - 2) - 4E(N_0 - 1) \right. \\ &\quad \left. + 6E(N_0) - 4E(N_0 + 1) + E(N_0 + 2) \right] \\ &= -\frac{(-1)^{N_0}}{8} \left[D(N_0 - 2) - 4D(N_0 - 1) \right. \\ &\quad \left. + 6D(N_0) - 4D(N_0 + 1) + D(N_0 + 2) \right] \\ &\quad - \frac{(-1)^{N_0}}{8} \left. \frac{\partial^4 E(N)}{\partial N^4} \right|_{N_0} + \dots \end{aligned} \quad (24)$$

For an odd- N isotope, $\Delta_n^{(5)}(N)$ is the weighted average of the gaps of three odd- N isotopes plus the contribution from the fourth and higher derivatives of the background, whereas for even- N isotopes, $\Delta_n^{(5)}(N)$ is the average of the gaps in the two adjacent odd-mass isotopes minus the contribution from the fourth and higher derivatives of the background. Between major shell closures, $\partial^4 E(N)/\partial N^4$ is in general very small. By contrast, any abrupt structural change, such as a shell closure or a shape transition, can lead to a discontinuity of $E(N)$. In such case, $D(N)$ has to absorb the additional binding from the discontinuity when matching $E(N)$ and the Taylor expansion (22). This can generate large peaks in $\Delta_n^{(3)}$ and $\Delta_n^{(5)}$ that have nothing to do with pairing correlations [38, 50].

In an HFB approach, with the exception of magic nuclei, the values of $\Delta_q^{(3)}$ and $\Delta_q^{(5)}$ are in general similar in size as, although not equivalent to, the average gaps defined through Eqs. (10) and (12). This is often used to adjust the calculated values for one of the average gaps of some even-even nuclei to empirical data for some finite-difference gap. Such procedure avoids having to calculate blocked configurations, but is prone to systematic errors that are difficult to control.

5.1.2 Representative examples

As representative examples, we choose the chains of Sn, Yb, and Pb isotopes. For these heavy elements, nucleus-dependent beyond-mean-field effects from symmetry restoration that cannot be easily absorbed into the parameters of the effective interaction can be expected to be less important than for the lighter ones [138–141].

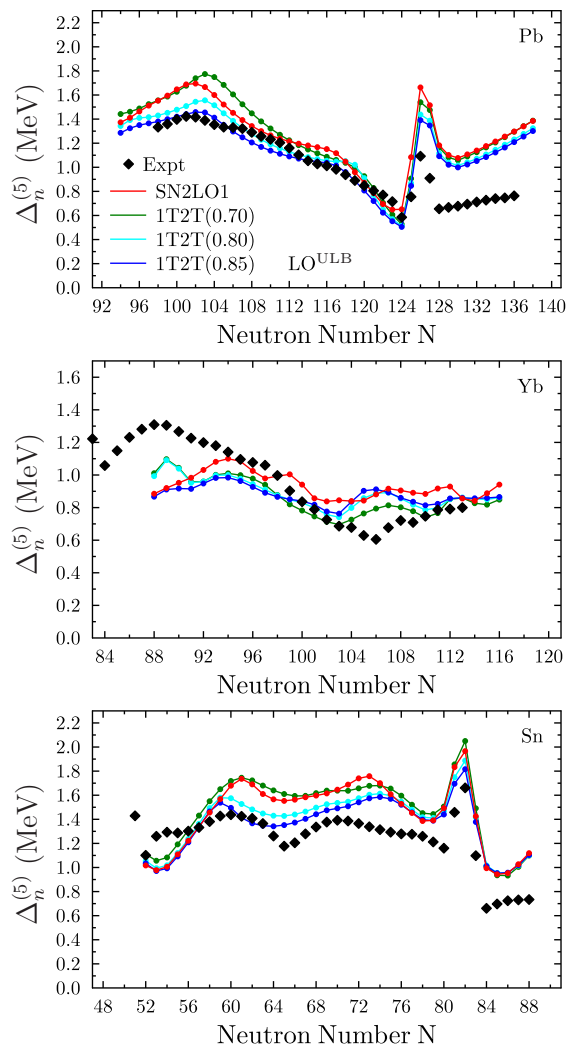


Fig. 16 Five-point neutron pairing gap $\Delta_n^{(5)}$ for the Sn, Pb, and Yb chains calculated with the 1T2T(X) and SN2LO1 parameter sets and LO^{ULB} pairing parameters.

In addition, heavy elements have much longer isotopic chains, which in general helps to identify systematic effects.

Results for the $\Delta_n^{(5)}$ for these three chains obtained with the four Skyrme parametrisations and the corresponding LO^{ULB} pairing parameters are shown in Fig. 16. With a few exceptions that will be addressed in what follows, all parameter sets give very similar results in spite of their different effective mass, and, in case of SN2LO1, also a different functional form. Indeed, for all nuclei results obtained with SN2LO1 remain very similar to those from 1T2T(0.70) that has a nearly identical effective mass.

Up to the $N = 126$ shell closure, the data for $\Delta_n^{(5)}$ of the Pb isotopes are quite well described, with some exceptions for the lightest isotopes for which there are some visible differences for 1T2T(0.70) and SN2LO1.

These deviations can partially be attributed to the different values of the effective mass. Indeed, the spherical $1h_{9/2-}$ and $1j_{13/2-}$ shells in the single-particle spectrum that are closest to the chemical potential for these isotopes change their relative distances and their distance to the $2f_{7/2-}$ below and the $3p_{3/2-}$ above which affects the amount of pairing correlations found in these nuclei. In particular, for 1T2T(0.70) and SN2LO1 the $1h_{9/2-}$ and $1j_{13/2-}$ shells are pulled even further down below the $1j_{13/2-}$ and $3p_{3/2-}$ than is already the case for 1T2T(0.80) in Fig. 1 with the $1h_{9/2-}$ getting also much closer to the $2f_{7/2-}$, whereas for 1T2T(0.85) the changes are in opposite direction. It seems that with decreasing effective mass, the single-particle spectrum of the light Pb isotopes predicted by the four parameter sets used here become more degraded. In fact, none of the parameter sets reproduces the change of ground state spin from $9/2-$ to $3/2-$ at $N = 101$; for 1T2T(0.85) it happens at $N = 103$, whereas SN2LO1, 1T2T(0.70), and 1T2T(0.80) predict that change for $N = 105$. Also, none of the parameter sets predicts the $13/2+$ state to be near-degenerate with the $3/2-$.

That the calculations overestimate the peak at $N = 126$ indicates that the discontinuity in total binding energies of even-even nuclei is too large for this shell closure. This is a consequence of the gap in the single-particle spectrum being too large for all parameter sets.

For the heaviest isotopes beyond $N = 126$, all parameter sets overestimate the experimental $\Delta_n^{(5)}$ by about 300 keV. This is a common feature of many mean-field predictions for pairing gaps in neutron-rich nuclei beyond a spherical shell closure that is also observed for the Sn isotopes, although for these the difference remains about 200 keV.

Interestingly, for the Sn isotopes the experimental data are about 400 keV larger for the isotopes directly above $N = 50$ than for those above $N = 82$. The calculations fall in between, predicting gaps of similar size in both cases that underestimate data for the lightest isotopes and overestimate the data for the heaviest ones. Around the neutron shell closures, the different parametrisations yield very similar gaps, whereas there are now some visible differences for the mid-shell isotopes. These can again at least partially be attributed to a mismatch between calculated and empirical single-particle spectra for these isotopes.

For Sn isotopes, the relative distance of single-particle states between $N = 50$ and $N = 82$ is not correctly described, see Fig. 1. In particular, the $1h_{11/2}$ intruder shell is too high above the normal-parity states, which is a common problem of most, if not all parametrisations of nuclear EDF models.

The trough at $N = 64$ in the experimental data is probably related to the complete filling of the $1g_{7/2+}$ shell, that should be more isolated from the levels around than is the case in the calculations, see Fig. 1. Comparing the 1T2T(x), the relative positions of the neutron single-particle levels around the chemical potential are very similar, with the sole exception being the distance between the $1g_{7/2+}$ and the $3s_{1/2+}$ that grows with effective mass. This explains why 1T2T(0.70) and SN2LO1 also predict a trough at $N = 64$, whereas 1T2T(0.80) does not. However, on the average it is 1T2T(0.85) that best describes the size of $\Delta_n^{(5)}$ around $N = 64$.

For the odd isotopes with $64 < N < 82$, all parameter sets give the same ground-state spin, which, however, agrees with data only for $N = 65, 67$ ($1/2^+$), 71 ($3/2^+$) and $75, 77$ ($11/2^-$), mainly as a consequence of the $2d_{3/2+}$ and $1h_{11/2-}$ shells being too distant from each other, see Fig. 1. For this reason, pairing correlations are probably too much dominated by the intruder $1h_{11/2-}$ shell that becomes the only one with large matrix elements of the pairing tensor. Because of its surface-peaked radial wave function, the pairing matrix elements within the spherical $1h_{11/2-}$ shell are also larger than those of the other shells by about 400 keV, and take absolute values that are similar to the $\Delta_n^{(5)}$. This effect becomes more pronounced with decreasing effective mass of the parameter sets. We therefore believe that the deviations of the $\Delta_n^{(5)}$ from data for many of the Sn isotopes below ^{132}Sn are mainly a direct consequence of the incorrectly predicted shell structure, and not a consequence of a very badly adjusted pairing interaction. However, as indicated by the analysis of Appendix E, these deviations can be amplified by the so-called time-odd terms in the EDF whose size is often correlated with effective mass, see also [142].

That the peak at $N = 82$ is too large is again a consequence of the gap in the single-particle spectrum being too large at this shell closure, but to a lesser extent than for ^{208}Pb . For the heavier isotopes for which there are data, all parameter sets predict that only the $2f_{7/2-}$ shell contributes significantly to pairing correlations. The reason is that it is well separated from the levels below by the major $N = 82$ shell closure, and also from the $3p_{3/2-}$ level above by a $N = 90$ sub-shell closure of about 1.8 MeV, see again Fig. 1. The spectrum of excited states of ^{133}Sn suggests that the level density above the $N = 82$ shell closure should be larger than what is predicted by the models, but correcting for this might lead to even stronger pairing correlations, such that we can only speculate about the origin of this mismatch.

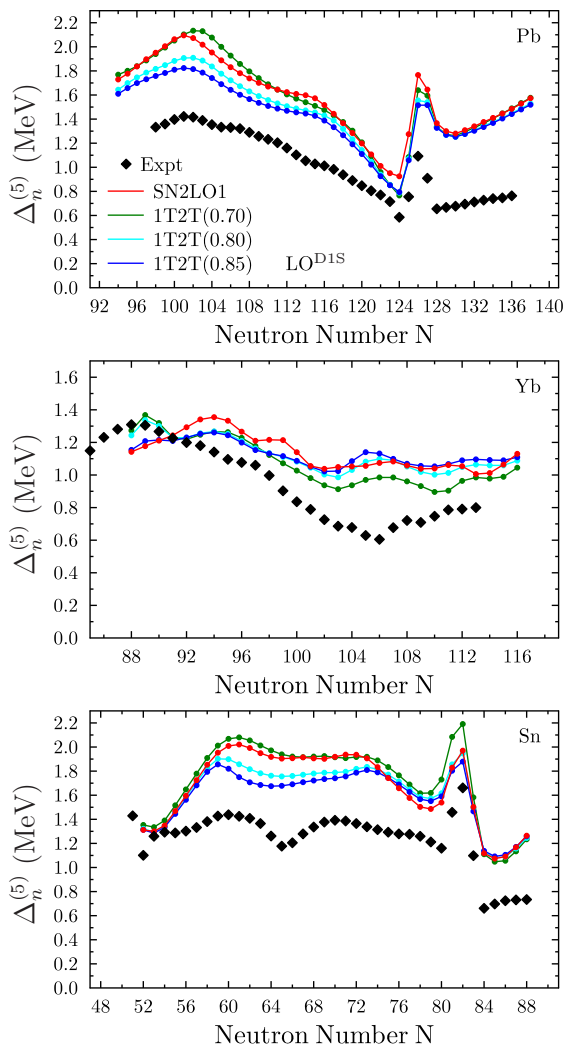


Fig. 17 Same as Fig. 16, but obtained using LO^{D1S} pairing parameters.

For the deformed Yb isotopes, the global trend of the data for $\Delta_n^{(5)}$ is similarly well described by all parameter sets, with only small differences between them. Similarly to what is found for the Sn isotopes, the experimental data are underestimated for neutron-deficient isotopes just above the spherical shell closure (which for Yb is $N = 82$, though), but then well described for the heavier ones, with the exception of the isotopes around $N = 106$ for which the trough in the data is not reproduced and a local maximum at $N = 104$ is predicted instead by all parameter sets. The latter can probably be attributed to the much larger bunching of calculated levels above the $N = 104$ gap than what is found in experiment, see Fig. 1. Similarly, the relative order of levels below the $N = 104$ gap is not correctly described, most obviously for the position of the $7/2^+$ intruder level that falls in between the $N = 100$ and $N = 104$ gaps predicted by the models. The size of matrix ele-

ments $\Delta_{\mu\nu}$ between time-reversed partner levels close to the chemical potential can differ between the various single-particle states by up to about 30%, so blocking the incorrect state can make a visible difference for the resulting energy loss.

During our analysis, we noticed that the predictive power of the pairing EDF for the odd-even staggering of nuclear masses is significantly degraded when not keeping all coupling constants of the *particle-hole* Skyrme EDF at the values obtained from an underlying Skyrme generator, as is for example done for the SLy4 parameter set. An analysis of this finding is given in Appendix E.

Figure 17 displays the same as as Fig. 16, but for calculations with LO^{D1S} pairing parameters. These pairing parameters yield much larger $\Delta_n^{(5)}$ than the LO^{ULB} , which in almost all cases largely overestimate the available data. When comparing the four ph parametrisations using LO^{D1S} pairing parameters among each other, the differences between them are very similar to what is found with the LO^{ULB} parameters, appearing for the same nuclei and having about the same size and sign. As both sets of parametrisations have a quite different spatial form factor in finite nuclei, this finding corroborates our earlier conjecture that the deviations between the parametrisations of the ph EDF originate mainly in differences of their single-particle spectra and time-odd terms.

5.1.3 Why $\Delta_q(k_\lambda)$ is not representative for the pairing interaction from the Gogny force

Pairing matrix elements obtained with the Gogny force D1S are a widely used reference in the literature. The lacking performance of the LO^{D1S} pairing parameter sets adjusted to reproduce the Gogny D1S pairing gaps $\Delta_q(k_{\lambda,q})$ in INM when applying them to finite nuclei therefore deserves an explanation, in particular when recalling that calculations with the original D1S interaction in the particle-hole and particle-particle channel describe these data well [13, 134]. There is apparently a feature of the original Gogny interaction that is lost when mapping it onto the LO pairing EDF through pairing gaps in infinite matter.

Let us note first that, in spite of the curves for the $\Delta_n^{(5)}$ in Fig. 17 suggesting that a re-scaling of the global pairing strength might bring calculations closer to experiment, we found that multiplying V_0 by a factor of 0.8 while keeping η and σ constant does not visibly improve the reproduction of the data for $\Delta_n^{(5)}$.

Considering that the LO^{D1S} gaps in INM are at almost all values of k_λ significantly smaller than those from the LO^{ULB} parameters, see Fig. 15, it is at first

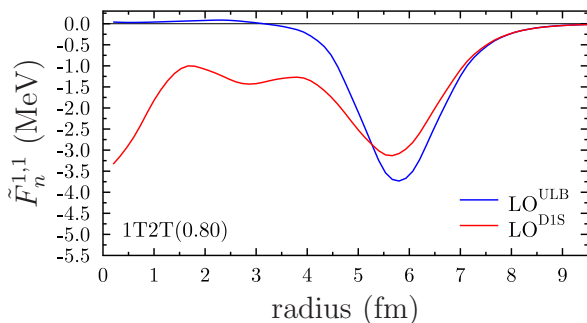


Fig. 18 Pairing potential $\tilde{F}_n^{1,1}(\mathbf{r})$ found for ^{120}Sn in calculations with 1T2T(0.80) and either the corresponding LO^{ULB} or LO^{DIS} pairing parameters.

surprising why pairing gaps in finite nuclei are well described by the LO^{ULB} parameters, but overestimated by the LO^{DIS} . The difference is made by the small region of momenta with $k_{\lambda,q} \gtrsim 1.15 \text{ fm}^{-1}$ for which the LO^{DIS} parameter sets still yield finite gaps in INM while pairing is already almost broken down for the LO^{ULB} . These values of $k_{\lambda,q}$ correspond to total densities that range from about 0.12 fm^{-3} to saturation density and slightly beyond, which are the densities that make most of the bulk volume of finite nuclei. When comparing the LO^{ULB} and LO^{DIS} pairing parameter sets, this then leads to very different pair potentials $\tilde{F}_n^{1,1}(\mathbf{r})$ in finite nuclei. This is illustrated by Fig. 18 for calculations of ^{120}Sn with 1T2T(0.80). LO^{ULB} pairing parameters lead to a surface-peaked $\tilde{F}_n^{1,1}(\mathbf{r})$ that is even slightly repulsive inside the nucleus, whereas LO^{DIS} pairing parameters yield both a strong peak at the surface and a large contribution in the volume, which then results in too large matrix elements $\Delta_{\mu\nu}$ for ^{120}Sn . It is because of this mix of surface and volume features of the LO^{DIS} parameter sets that, as mentioned above, a simple moderate rescaling of the overall strength V_0 would not significantly improve on the description of the $\Delta_q^{(5)}$ of finite nuclei in Fig. 17.

This explains why the LO^{DIS} pairing parameters overestimate pairing gaps in finite nuclei, but does by itself not explain why our adjustment procedure for the LO^{DIS} pairing parameters yields unrealistic pairing properties although it starts from a realistic pairing interaction. The deeper origin of the problem is that for a finite-range pairing interaction like the Gogny force the gap at the chemical potential $\Delta_q(k_\lambda)$ is not fully representative for the pairing interaction in infinite matter. This can be seen when comparing the k -dependence of the gap Δ_k in INM of the original Gogny interaction with what is obtained using LO^{DIS} parameters for SLy4, see Fig. 19 for six different values of $k_{\lambda,q}$ that provide every other of the gaps used to adjust the LO^{DIS}

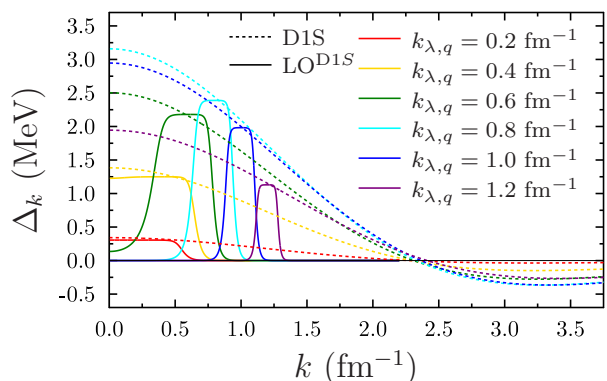


Fig. 19 Dotted lines: matrix elements Δ_k as a function of momentum k from HFB calculations of symmetric INM with the D1S parametrisation of the Gogny interaction taken from Ref. [118] at values of $k_{\lambda,q}$ as indicated. Solid lines: matrix elements Δ_k obtained from INM calculations at the same values of $k_{\lambda,q}$ performed with SLy4 and a LO pairing EDF whose parameters are adjusted to reproduce the gap $\Delta_q(k_{\lambda,q})$ in symmetric matter predicted by the Gogny D1S interaction.

pairing parameters to the gaps from D1S as listed in Table 4.

The gaps Δ_k obtained with D1S have a strong k dependence and even change their sign at high momenta for $k \simeq 2.3 \text{ fm}^{-1}$ before falling off to zero at even higher values of k . The sign change has its origin in the Gogny force being the combination of an attractive long-range part with a repulsive short-range part in the 1S_0 channel. The momenta at which the Δ_k become negligibly small depends on the shortest range of the interaction, which for D1S is the one of the repulsive part in the pairing channel. By contrast, as discussed in Sec. 3.3, a local LO pairing EDF leads to pairing matrix elements and gaps between all plane-wave states that in the absence of a cutoff are simply constant. The k dependence of the Δ_k from SLy4+ LO^{DIS} visible in Fig. 19 results from the energy cutoff (B.71).

There is, however, an important difference between how any energy cutoff acts in INM and in finite nuclei. Because of the one-to-one correspondence (18) between momentum k and single-particle energy $\varepsilon_{\mathbf{k}\sigma q}$, it is only in INM that an energy cutoff (8) also acts like a momentum cutoff, although with a density-dependent window size. This is different for finite nuclei, for which the eigenstates of the single-particle Hamiltonian are a wave packet spread over a large range of momenta. As an example for the most relevant neutron single-particle states in the vicinity of the chemical potential λ_n of the spherical nucleus ^{120}Sn , Fig. 20 displays the square of the reduced radial momentum-space wave function $k^2 |\psi_{njlq}(k)|^2$ obtained from the Fourier transformation of the full 3d wave function with isospin q , total angular

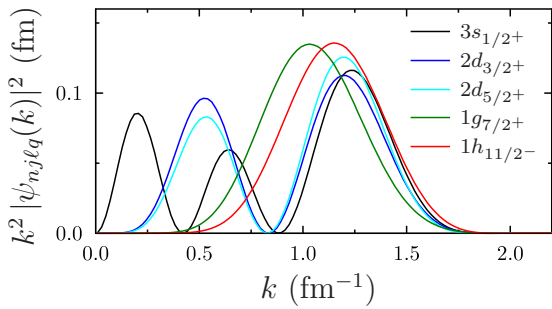


Fig. 20 Square of the reduced radial momentum-space wave function $k\psi_{n_j l q}(k)$ of the neutron levels around the chemical potential of ^{120}Sn calculated with SLy4+ULB pairing.

momentum j and orbital angular momentum ℓ

$$\psi_{n_j l q}(k) = \int_0^L dr r^2 j_\ell(kr) \psi_{n_j l q}(r), \quad (25)$$

where L is the size of the radial numerical box and the wave function is normalised to

$$4\pi \int_0^\infty dk k^2 |\psi_{n_j l q}(k)|^2 = 1. \quad (26)$$

The quantity $k^2 |\psi_{n_j l q}(k)|^2$ is proportional to the probability that a neutron in the given spherical shell takes the momentum k .

In finite nuclei the cutoff (8) of the LO EDFs multiplies the contribution from the entire single-particle state, irrespective of its decomposition into k components. For ^{120}Sn , all of the five single-particle states displayed in Fig. 20 fall inside the pairing window of the LO pairing EDF as can be deduced from Fig. 1. For each of them, $k^2 |\psi_{n_j l q}(k)|^2$ has a peak around $k \simeq 1.2 \text{ fm}^{-1}$ and is spread up to $k \simeq 1.7 \text{ fm}^{-1}$.

The matrix elements Δ_k seen by these momentum-space wave functions³ are therefore what is displayed in Fig. 21. Unfortunately, because of the combined momentum- and density-dependence of the Δ_k , the matrix elements $\Delta_{n_j l q}$ of the pair potential for states within a given spherical j shell in finite nuclei cannot be simply written as the integral over $k^2 |\psi_{n_j l q}(k)|^2$ of Fig. 20 times Δ_k . Still, combining the information from Figs. 20 and 21 qualitatively explains the very different performance of the Gogny force D1S and the LO^{D1S} parameter sets for finite nuclei.

With the exception of the $3s_{1/2+}$ shell, the dominant k contributions to the single-particle states are at

³High- k components of the single-particle states in finite nuclei are still implicitly cut by the usual choices for the numerical representation, which for the calculations presented here is the highest momentum that can be represented on the coordinate-space Lagrange mesh. For the spacing of $\Delta x = 0.8 \text{ fm}$ used for the 3d calculations of finite nuclei, this implicit cutoff amounts to $k_{\text{max}} = \pi/\Delta x = 3.927 \text{ fm}^{-1}$, which is outside the range of k displayed in Figs. 19, 20, and 21.

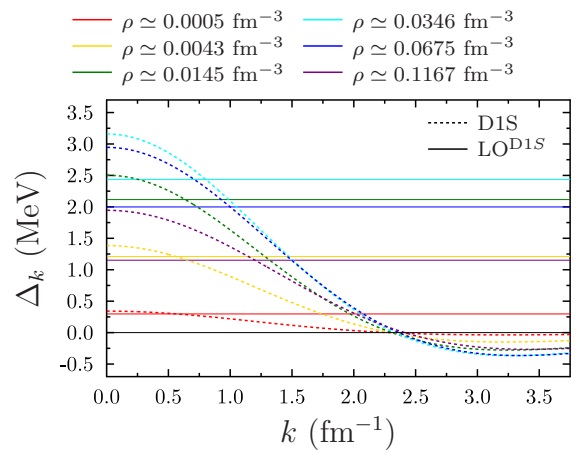


Fig. 21 Same as Fig. 19, but the Δ_k are now plotted as they contribute for single-particle states inside the pairing window of a finite nucleus. For easier connection with finite nuclei, the curves are now labelled by the density ρ in INM instead of the corresponding k_λ .

momenta at which the Δ_k from the LO^{D1S} parameters are significantly larger than the Δ_k from the original Gogny force at all densities. As a consequence, for most single-particle states in finite nuclei the LO^{D1S} parameters yield matrix elements $\Delta_{n_j l q}$ of the pair potential that are significantly larger than what is obtained with the full Gogny force that the LO pairing EDF tries to mimic. Owing to their structure with a single peak, this effect is most pronounced for high- j levels that, because of their high degeneracy, provide the dominant contributions to neutron pairing correlations.

By contrast, at small k , the Δ_k from the full Gogny force are at most densities larger than the Δ_k from the LO^{D1S} parameters. For single-particle states that are dominated by small- k contributions the opposite could happen, but this mostly concerns $s_{1/2+}$ levels that, because of their small degeneracy, only have a minor contribution to pairing correlations in strongly-bound heavy nuclei. Still, this might be of relevance when studying halo nuclei – for which the very extended spatial wave functions have very large low- k components – with pairing EDFs that are adjusted in the spirit of what is done for the LO^{D1S} parameter sets.

In summary, adjusting the parameters of a LO pairing EDF to the INM gaps $\Delta_q(k_{\lambda,q})$ at $k_{\lambda,q}$ obtained from the Gogny force is not sufficient to replicate the performance of the Gogny force for pairing gaps in finite nuclei. This explains why the LO^{D1S} parameter sets significantly overestimate the $\Delta_n^{(5)}$ displayed in Fig. 17.

We expect that a similar mismatch will also be found when adjusting the parameters of an LO pairing EDF solely to the $\Delta_q(k_{\lambda,q})$ obtained from HFB calculations of INM with other finite-range pairing interactions, or

when matching the $\Delta_q(k_{\lambda,q})$ from more microscopic methods.

5.2 Odd-even staggering of charge radii

Nuclear charge radii exhibit a pronounced odd-even staggering along isotopic chains, where in the vast majority of cases the charge radius of an odd isotope is smaller than the average of the charge radii of its even-even neighbours. There are a few known exceptions, which are usually attributed to either shape transitions or to the presence of exotic deformation modes. It has been pointed out [68–75] that in self-consistent mean-field calculations the contribution of a density-dependent pairing EDF to the single-particle Hamiltonian (3) can generate such an odd-even effect. The mechanism is that for a pairing EDF of form (1), its contribution to $F_q^{1,1}(\mathbf{r})$ is proportional to the sum of the absolute squares of the proton and neutron pair densities $\tilde{D}_q^{1,1}(\mathbf{r})$ and $\tilde{C}_q^{1,1}(\mathbf{r})$ whose size overall scales with the magnitude of pairing correlations. As pairing correlations in an odd nucleus are in general weaker than in the adjacent even-even isotopes, the always repulsive pairing contribution to $F_q^{1,1}(\mathbf{r})$ is smaller in odd nuclei than in even-even nuclei. With this, the single-particle energies of all bound neutrons *and* protons are slightly lower in odd nuclei than in the adjacent even isotopes, meaning that the single-particle states are slightly more localised inside odd nuclei. This ultimately leads to a small systematic shift between the charge radii of the odd and even isotopes.

The mean-square (ms) charge radii r_{ch}^2 are calculated taking into account corrections for the internal charge distribution of protons and neutrons, relativistic corrections from the distribution of magnetisation of protons and neutron and the Darwin-Foldy term, as well as a correction for the spurious centre-of-mass motion of a nuclear mean-field state, leading to the expression [143–146]

$$\begin{aligned} r_{\text{ch}}^2 &= \frac{1}{Z} \int d^3r r^2 \rho_{\text{ch}}(\mathbf{r}), \\ &= \frac{1}{Z} \int d^3r r^2 \rho_p(\mathbf{r}) + \langle r_p^2 \rangle + \frac{N}{Z} \langle r_n^2 \rangle \\ &\quad - \frac{2\mathcal{D} \mu'_p}{Z} \int d^3r r^2 \nabla \cdot \mathbf{J}_p(\mathbf{r}) \\ &\quad - \frac{2\mathcal{D} \mu_n}{Z} \int d^3r r^2 \nabla \cdot \mathbf{J}_n(\mathbf{r}) + 3\mathcal{D} \\ &\quad - \frac{3b^2}{2} A^{-1}. \end{aligned} \quad (27)$$

where $\rho_p(\mathbf{r}) = D_p^{1,1}(\mathbf{r})$ is the point-proton distribution, $\nabla \cdot \mathbf{J}_q(\mathbf{r}) = \nabla \cdot \mathbf{C}_q^{1,1, \nabla \times \sigma}(\mathbf{r})$ the divergence of the spin-current vector density of protons ($q = p$) and neutrons

($q = n$), $\langle r_p^2 \rangle = 0.8409 \text{ fm}^2$ and $\langle r_n^2 \rangle = -0.1155 \text{ fm}^2$ the ms radii of the internal charge distribution of protons and neutrons, $\mu'_p = \mu_p - 1/2 = 2.2928473446 \mu_N$ and $\mu_n = -1.9130427 \mu_N$ the anomalous contribution to the magnetic moment of protons and neutrons in units of the nuclear magneton μ_N , $\mathcal{D} = (\hbar^2/2m_a)^2 = 0.011042234 \text{ fm}^2$ a constant entering the relativistic corrections, and finally $b^2 = \hbar^2/(41m_a A^{-1/3} \text{ MeV})$, which equals $1.01148879 A^{1/3} \text{ fm}^2$, enters the harmonic-oscillator estimate of the centre-of-mass correction, where $m_a = \frac{1}{2}(m_n + m_p)$ is the average mass of protons and neutrons (see Ref. [146] for details).

The odd-even staggering of root-mean-square (rms) charge radii along an isotopic chain can be estimated in analogy to the odd-even staggering of binding energies discussed in Sec. 5.1.1 through the three-point difference

$$\begin{aligned} \Delta_r^{(3)}(N) &= -\frac{(-1)^N}{2} \left[r_{\text{ch}}(N-1) - 2r_{\text{ch}}(N) + r_{\text{ch}}(N+1) \right] \end{aligned} \quad (28)$$

that estimates the “gap” between the surface that interpolates between the charge radii of odd- N nuclei and the surface that interpolates between the charge radii of even-even nuclei. We use a convention for the sign of $\Delta_r^{(3)}$ such that positive values indicate normal staggering when the radii of even-even isotopes are larger than the average of the radii of the two adjacent odd- A nuclei.

For radii, using the three-point expression (28) instead of a higher-order formula is sufficient because – contrary to the systematics of binding energies – there is no significant contribution to the radii that scales with the square of the nucleon numbers. Some authors use an alternative definition of $\Delta_r^{(3)}(N)$ [147, 148] without the alternating sign $(-1)^N$ that, for nuclei with normal staggering of radii, leads to positive values for even isotopes and negative values for odd ones. In our opinion, such convention makes the identification of systematic trends in the deviation from experiment unnecessarily difficult.

Figure 22 displays results for $\Delta_r^{(3)}$ of the rms charge radii obtained from the same calculations used to prepare Fig. 16. For most isotopes in each of the three chains, theory predicts normal odd-even staggering of charge radii, although with some striking differences between the isotopic chains. Results obtained with the four parameter sets are overall very similar; in particular, there is no clearly identifiable impact of the effective mass, and results obtained with SN2LO1 are very similar to those obtained with the three NLO parameter sets.

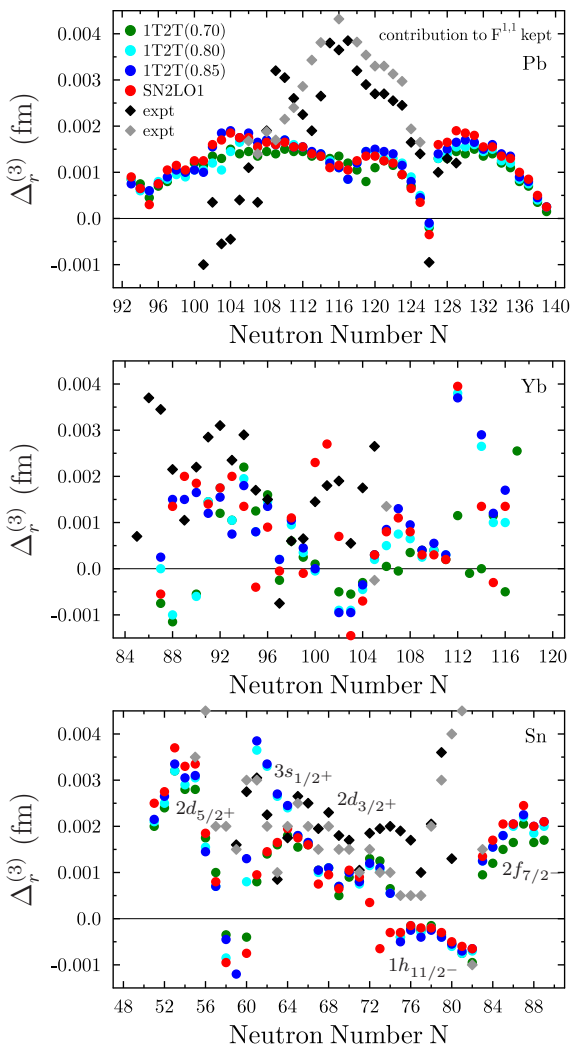


Fig. 22 Three-point gap $\Delta_r^{(3)}$ of the rms charge radii of the Sn, Pb, and Yb isotopic chains calculated with the 1T2T(X) and SN2LO1 parameter sets and LO^{ULB} pairing parameters, taking into account the contribution of the pairing EDF to $F_q^{1,1}(\mathbf{r})$. Experimental data taken from different sources are plotted with either black or grey diamonds (see text). Quantum numbers indicate the blocked ground-state configuration of Sn isotopes obtained with 1T2T(0.80).

Before comparing the model predictions with experiment, we analyse the effect of keeping or not the contribution (3) from the pairing EDF to the potential $F_q^{1,1}(\mathbf{r})$ that enters the single-particle Hamiltonian. To this aim, Fig. 23 displays results for $\Delta_r^{(3)}$ calculated in the same manner as in Fig. 22, except that the contribution (3) from the pairing EDF to the potential $F_q^{1,1}(\mathbf{r})$ is omitted when solving the HFB equations. In particular for the chains of spherical Sn and Pb isotopes, this makes a large systematic difference: $\Delta_r^{(3)}$ values calculated without the pairing contribution to the potential $F_q^{1,1}(\mathbf{r})$ are systematically smaller than those obtained with the pairing contribution, in some

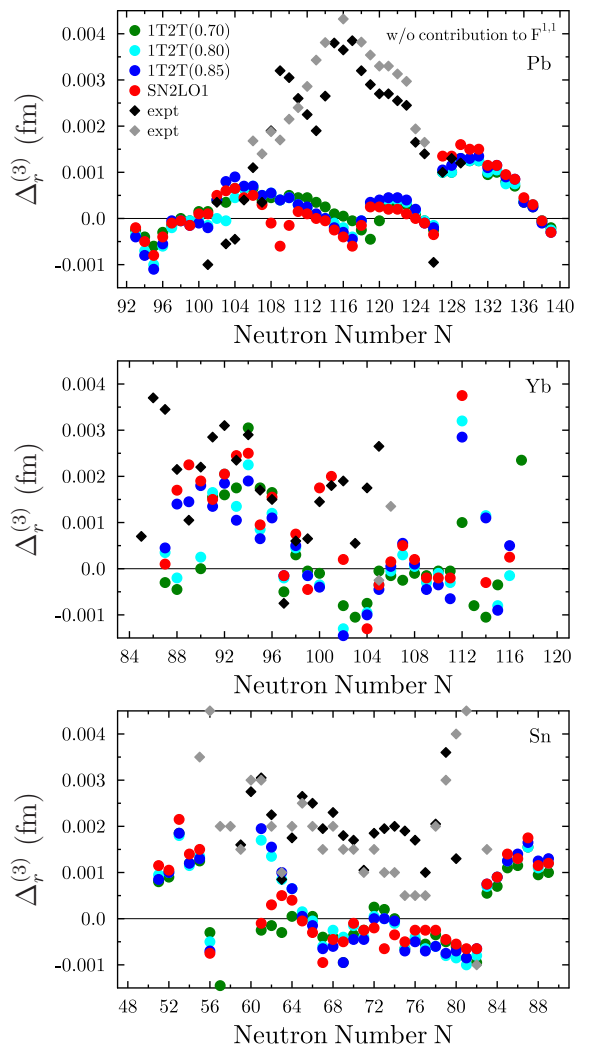


Fig. 23 Same as Fig. 22, but omitting the contribution of the pairing EDF to $F_q^{1,1}(\mathbf{r})$ in the calculations.

cases even exhibiting inverted odd-even staggering. For the deformed Yb isotopes, however, the differences between both sets of calculations are more subtle. This is possibly a degeneracy effect: for spherical nuclei, blocking a sub-state in a highly-degenerate j -shell yields a spatial change to $F_q^{1,1}(\mathbf{r})$ that has a large overlap with all other non-blocked orbits from the same j -shell that have practically the same radial wave function, whereas in deformed nuclei there is only the conjugate state that has a similar orbit.

The odd-even staggering of rms charge radii is a small effect on the order of a few permille of the total size of r_{ch} , and often also comparable in size with its experimental error bar. The odd-even staggering of ms charge radii is clearly and systematically visible in the measurements of the isotopic shift of ms charge radii, see for example Refs. [149–151] for Pb isotopes. After conversion of isotopic shifts to rms charge radii, how-

ever, the propagated error bars of the rms charge radii usually take values of a few times 10^{-3} fm, which is already comparable in size to the typical values of $\Delta_r^{(3)}$, whose error bar would be even larger. As it is customary in most of the existing literature on the odd-even staggering of rms charge radii, we omit the error bars of experimental data in Figs. 22 and 23 that otherwise would be illegible.

A related issue is that experimental data taken from different sources also often disagree on the order of a few times 10^{-3} fm. In Figs. 22 and 23, black diamonds indicate experimental values constructed from the rms charge radii tabulated in Ref. [152], whereas grey diamonds indicate data from more recent measurements of isotopic shifts. For Pb isotopes with $N \simeq 112$, the $\Delta_r^{(3)}$ computed from the isotopic shifts reported in Ref. [151] have the opposite slope compared to those obtained from Ref. [152]. Besides covering a wider range in N than the data tabulated in Ref. [152], the recent data for Sn isotopes reported in Ref. [147] significantly differ from those of Ref. [152] for the isotopes just below the $N = 82$ shell closure. Note, however, that data for rms charge radii reported in Ref. [147] are limited to three digits after the decimal point, which consequently results in a “binning” of the $\Delta_r^{(3)}$ values in discrete steps of 0.0005 fm. Because of this, one cannot attribute a significance to any disagreement of theory – or other experiments – with the $\Delta_r^{(3)}$ from Ref. [147] that remains smaller than that. There also are new experimental data for the isotopic shifts of ^{175}Yb and ^{177}Yb [153, 154]. Isotope ^{177}Yb was not included in Ref. [152], but the rms radius of ^{175}Yb resulting from this new measurement is significantly larger than the value tabulated there. This changes the experimental $\Delta_r^{(3)}$ value of ^{175}Yb from +0.00265 fm when computed from data listed in Ref. [152] to -0.00025 fm when using the data from Ref. [153]. All of this indicates that the experimental data for $\Delta_r^{(3)}$ have so large uncertainties that the comparison between theory and data has to be made with great caution.

It also has to be recalled that the charge radii of different configurations of a given odd- A nucleus are different, as is for example indicated by available data for low-lying spin-isomeric states in odd-mass Pb [149–151] and Sn [155] isotopes. Such configuration dependence is also found in calculations, independent of including or not the contribution of the pairing EDF to the potential $F_q^{1,1}(\mathbf{r})$, Eq. (3). The absolute size of the charge radius of a given configuration, and the differences between them, are of course different when including or not the contribution from the pairing EDF to the potential. An example where this is clearly visible on Figs. 22 and 23 are the $\Delta_r^{(3)}$ values of Sn isotopes around $N =$

61, for which different parameter sets predict different ground-state configurations that have significantly different charge radii. Because of this sensitivity, it cannot be expected that theory correctly predicts $\Delta_r^{(3)}$ values unless it also predicts the correct ground-state spin. And as already illustrated in Sec. 5.1.2, the theoretical predictions for the ground-state spin of odd nuclei often do disagree with experiment. One could of course block the same configuration as found in experiment, which for calculating total charge radii and their isotopic shifts is a valid strategy. But if the explanation of the origin of the odd-even staggering of charge radii sketched above is correct, in view of the smallness of this effect it is less obvious that blocking a single-particle level that has an incorrect distance to the chemical potential will induce the correct rearrangement effects with changing potential depth when comparing odd and even-even isotopes.

The mismatch in ground-state configuration between theory and experiment found for some nuclei in Fig. 1 therefore explains some of the large deviations found between calculated and observed $\Delta_r^{(3)}$ values in Figs. 22 and 23. For the odd-mass Pb isotopes between $105 \leq N \leq 117$, theory and experiment agree on the ground-state spin $3/2^-$, but above and below they often disagree. For the heavier isotopes up to the $N = 126$ shell closure, experiment assigns $5/2^-$ for $119 \leq N \leq 123$, and $1/2^-$ only for $N = 125$, whereas theory predicts $1/2^-$ ground states for all of these. Going to lighter isotopes, theory predicts the transition to $9/2^-$ ground states at $N = 103$, whereas in experiment this is observed at $N = 99$. The latter could be the reason why the inverted staggering at around $N \simeq 102$ is not reproduced by theory, and why theory underestimates the staggering around $N \simeq 124$. But for the Pb isotopes around $N \simeq 110$ there is a large systematic mismatch between theory and experiment for $\Delta_r^{(3)}$ despite the fact that the ground-state spin is correctly predicted.

For the Sn isotopes, the evolution of the calculated $\Delta_r^{(3)}$ with N is much more discontinuous than what is found for the Pb isotopic chain. Interestingly, almost all of these discontinuities occur where the ground-state configuration changes in the model description. With 1T2T(0.80), one finds $5/2^+$ up to $N = 59$, then $1/2^+$ for $61 \leq N \leq 67$, $3/2^+$ for $69 \leq N \leq 73$, $11/2^-$ for $75 \leq N \leq 81$, and finally $7/2^-$ for N above. With the exception of the $5/2^+$ configurations that yield an arch-like dependence of $\Delta_r^{(3)}$, each of the other ground-state configurations leads to a distinctly different size of $\Delta_r^{(3)}$. Sometimes, the other three parameter sets predict the change of ground-state configuration to happen for different isotopes, in which case there are large differences between the calculated $\Delta_r^{(3)}$ from different parameter sets. In particular, the other parameter sets predict that

either ^{109}Sn (with SN2LO1) or ^{111}Sn (with 1T2T(0.70) and 1T2T(0.85)) has a $7/2^+$ ground state, which explains the large deviations between models around $N = 60$.

For the Yb isotopes, the calculations roughly follow the global trend of the experimental data for $\Delta_r^{(3)}$, but again with many differences in detail. Because of the ground-state configuration being deformed, all single-particle levels in the fully paired states are just twofold degenerate. The observed ground-state spin of the blocked configurations changes each time when going to the next odd-mass isotope, whereas in the model calculations there are a few cases where two consecutive odd-mass isotopes are predicted to have the same blocked configuration.

As already discussed in Sec. 5.1.2, the ground-state spin of the Yb isotopes is not always correctly predicted, which can be expected to also have an impact on the predictions for $\Delta_r^{(3)}$. The largest deviations between theory and experiment are found for the isotopes around $N \simeq 100$, for which also the odd-even staggering of masses is badly described. At the same time it seems that the $\Delta_r^{(3)}$ of the Yb isotopes are less sensitive to such a mismatch than what is found for the chains of spherical Sn and Pb isotopes. This could again be related to the smaller degeneracy of single-particle levels that leads to a much smaller impact of the change of $F_q^{1,1}(\mathbf{r})$ as all single-particle levels have different spatial orbits.

In spite of the uncertainties of the data and the many differences found between data and experiment, the LO^{ULB} parameter sets yield an odd-even staggering of charge radii of reasonable size, in particular for Sn and Yb isotopes, if, and only if, the contribution of the pairing EDF to $F_q^{1,1}(\mathbf{r})$ is included. However, the large discrepancy found for Pb isotopes with $112 \leq N \leq 122$ – which is the region for which the odd-even staggering of masses is very well described – either points to the need for additional terms in the pairing EDF (such as the gradient terms used in Refs. [69–75]) or to missing microscopic physics in the model, or to an ill-controlled aspect of the particle-hole part of the EDF. A candidate for the latter are the time-odd terms of the ph EDF. As explained in Appendix E, some of them have a sizeable contribution to the odd-even staggering of binding energies, and thereby can also introduce an odd-even effect to the eigenvalues of the single-particle Hamiltonian that then feeds back onto the localisation of the spatial wave functions.

We note in passing that mean-field models that employ an extended pairing EDF with an additional dependence on the square of the gradient of the normal density and that are fine-tuned to describe the iso-

topic shifts and their odd-even staggering of Ca isotopes [74,75] largely overestimate the available data for the odd-even staggering of the charge radii of many spherical Sn [147] and Pb isotopes [151], and even more so those for the deformed Yb isotopes [148]. This possibly indicates that the mechanism that drives the evolution of charge radii in the pf -shell region is different from the mechanism behind the smaller and more regular odd-even staggering found for most heavy nuclei.

We will not detail results for $\Delta_r^{(3)}$ obtained with the LO^{DIS} parametrisations. From the discussion in Sec. 5.1 it cannot be expected that they well describe the pair densities that are at the origin of the variation of $F_q^{1,1}(\mathbf{r})$ between odd and even isotopes. Overall, the LO^{DIS} parameters also predict mostly positive values of $\Delta_r^{(3)}$ of Sb, Pb, and Yb isotopes when including the contribution of the pairing EDF to the single-particle potential $F^{1,1}(\mathbf{r})$. The actual values for $\Delta_r^{(3)}$, however, tend to be somewhat smaller than what is found with the LO^{ULB} .

5.3 Rotational moment of inertia

Shortly after the successful explanation of superconductivity in solids with the BCS model, it was pointed out that the presence of pair correlations could strongly affect the rotational moments of inertia of atomic nuclei, which to a large extent resolved the discrepancy between earlier models and available data [156, 157].

A widely-used approach to model nuclear collective rotation microscopically is to determine the energy $E(J)$ of rotating states with angular momentum J in a self-consistent cranked HFB calculation⁴ that minimises the Routhian E^ω [1, 49, 158]

$$E^\omega = E(J) - \omega_c \langle \hat{J}_z \rangle \quad (29)$$

that represents the energy of the nucleus in a frame rotating with the angular frequency ω_c . Like in the majority of applications of this model, the symmetries imposed in the MOCCa code used here imply principal-axis cranking, where the direction of the angular momentum vector is aligned with a major axis of a triaxial nuclear shape. For sake of compact notation, throughout this paper it is assumed that angular momenta are in units of \hbar .

⁴The fully variational cranked HFB method is not to be confused with the so-called “cranking approximation” [1, 2, 156, 157] for the calculation of moments of inertia. The latter is perturbative and neglects the nuclear response to rotational motion, in particular from the time-odd terms in the EDF. The moment of inertia from cranked HFB (often in the limit of small ω_c) is also known as the Thouless-Valatin [1] moment of inertia. We are, however, interested in the evolution of the moment of inertia along the rotational band.

In many implementations of cranked HFB, E^ω and $\langle \hat{J}_z \rangle$ are obtained from minimising E^ω for a set of systematically varied values of ω_c . In our calculations, however, the Lagrange parameter ω_c is adjusted to reproduce prescribed values of $\langle \hat{J}_z \rangle = \sqrt{J(J+1)}$ that can be associated with the energy levels at angular momentum J in the rotational band. With this, γ -ray energies and moments of inertia can be calculated in exactly the same way as in the evaluation of experimental data.

For a schematic axially-symmetric rigid rotor with constant moment of inertia Θ and energy spectrum $E(J) = J(J+1)/2\Theta$, the γ ray transition energies between the levels at J and $J-2$

$$E_\gamma(J) = E(J) - E(J-2) \quad (30)$$

would depend linearly on J , $E_\gamma(J) = (4J-2)/2\Theta$. In the cranked HFB description of nuclear rotation, however, the moment of inertia changes with increasing J . The reason is that the expectation value of the many-body angular momentum \hat{J}_z entering the Routhian (29) is generated microscopically from the one-body current $\mathbf{j}_0(\mathbf{r})$ and spin density $\mathbf{s}_0(\mathbf{r})$ distributions

$$\langle \hat{J}_z \rangle = \int d^3r \mathbf{e}_z \cdot [\mathbf{r} \times \mathbf{j}_0(\mathbf{r}) + \frac{1}{2}\mathbf{s}_0(\mathbf{r})]. \quad (31)$$

To obtain a given finite value of $\langle \hat{J}_z \rangle$, the angular momenta of the single-particle states progressively align with the axis of collective rotation. Because the angular momenta of the two nucleons in a conjugate pair of the $J=0$ ground state point into opposite directions, one of them tends to align more with the rotational axis than the other. The resulting mismatch between the spatial orbits of the conjugate states generates the time-odd densities $\mathbf{j}_0(\mathbf{r})$ and $\mathbf{s}_0(\mathbf{r})$, and in general also weakens pairing correlations [158–160]. In specific cases, including some of the Yb isotopes discussed here, the single-particle energies of the two nucleons in some of the pairs changes so quickly in opposite direction with J such that a multi-quasiparticle configuration is found as the energetically lowest (“yrast”) state when solving the cranked HFB equations. At such transition, the moment of inertia often dramatically changes, which produces a so-called “backbending” when plotting the moment of inertia as a function of ω . The same is found when plotting the moments of inertia deduced from the observed transitions between yrast states [158–160].

In cranked HFB, the nucleus’ response to rotation is also affected by the size of the often not very well controlled time-odd terms in the EDF, which can lead to significant differences between the moments of inertia predicted by different parameter sets [40, 142, 161].

For the purpose of probing the predictive power of the pairing interaction, we found it however more

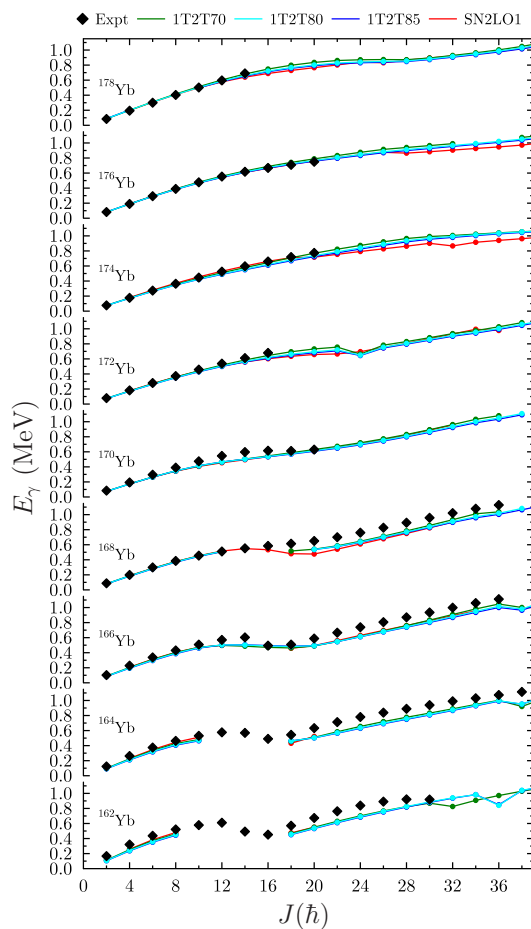


Fig. 24 γ -ray transition energies E_γ of yrast states of the even-even Yb isotopes as indicated calculated with the 1T2T(X) and SN2LO1 parameter sets and LO^{ULB} pairing parameters (see text). Note that for many states and nuclei, results obtained with the four parametrisations cannot be distinguished on the scale of the figure.

straightforward to analyse E_γ as a function of angular momentum J instead of the more frequently discussed kinematical or dynamical moments of inertia that highlight effects from the alignment of single-particle orbits with the rotational axis. When plotting E_γ as a function of J , as done in Fig. 24, a backbend is signalled by a decrease of E_γ with J , i.e. a substantial increase of the collective moment of inertia. Because of the coexistence of two different solutions of the cranked HFB equations (29) with same ω_c at a backbend, fully self-consistent HFB calculations do not always converge for angular momenta for which E_γ decreases even when fixing the expectation value of \hat{J}_z , which explains the absence of some calculated points.

Note that in the analysis of rotational bands, the value of E_γ can be associated with the empirical rotational frequency $\omega(J-1) = E_\gamma(J)/2$ [158], which in

general takes a similar (albeit not identical) value as the Lagrange parameter ω_c in Eq. (29).

Results from cranked HFB calculations for the yrast band of even-even Yb isotopes obtained with the LO^{ULB} pairing parameters are displayed in Fig. 24. We limited the range of isotopes to those for which data are available and whose calculated deformation energy surface has a pronounced minimum at large deformation.

The angular momenta at which the backbendings are found in experiment are in general fairly well reproduced by the calculations, which implies that, in spite of the many problems with the relative distances between single-particle levels pointed out above, the position of the quickly aligning levels relative to the chemical potentials is quite well described by all four parameter sets.

For most Yb isotopes, calculations closely follow data for E_γ up to the backbend, but then tend to underestimate the values of E_γ above, an exception being the lightest isotopes $^{162-164}\text{Yb}$, for which the E_γ are somewhat underestimated at all J . Also, in almost all cases, the results from all four parameter sets nearly fall on top of each other, notable exceptions being high-spin states of ^{174}Yb and ^{176}Yb for which SN2LO1 predicts slightly smaller E_γ for angular momenta for which there are no data available yet. Still, compared to the many small differences found between the parameter sets for the $\Delta_n^{(5)}$ and $\Delta_r^{(3)}$, the similarity of results for E_γ is quite striking. The LO^{ULB} parameter sets quite satisfactorily describe pairing correlations for these nuclei, irrespective of the effective mass of the parametrisation, or the detailed form of the EDF.

We will not discuss results of E_γ obtained with the LO^{D1S} parametrisations in detail. What is found is that the E_γ values are systematically slightly larger than those obtained with the LO^{ULB}, as is expected because of the overall stronger pairing interactions. For the LO^{D1S} parameter sets all calculated curves also fall almost perfectly on top of each other when plotting these results on the same scale as in Fig. 24.

6 Summary, conclusions, and outlook

Motivated by the well-known observation that the adjustment of the parameters of the pairing interaction is compromised by insufficiencies of the single-particle spectra predicted by even the best available parametrisations of the particle-hole EDF, we explored the possibility to use pairing properties of the idealised model system of infinite matter for a more controlled parameter adjustment of effective pairing interactions that accompany a given parametrisation of the mean fields.

To that aim, we implemented a solver for the HFB equations of infinite homogeneous non-polarised nuclear matter at arbitrary isospin asymmetry that can handle very general local Skyrme EDFs in the ph and pp channels.

Limiting ourselves for the present study to the widely-used density-dependent LO local pairing EDF, we studied the correlation between the pairing gap in INM and pairing properties of finite nuclei. As reference calculations for the gaps in INM we utilised two time-tested pairing interactions. One is the ‘‘ULB’’ parametrisation of the LO local pairing EDF, originally adjusted for the SLy4 parametrisation of the Skyrme NLO EDF and also widely used since with other parametrisations with the same isoscalar effective mass $m_0^*/m = 0.7$. The other is the D1S parametrisation of the finite-range Gogny interaction.

To cover a wide range of underlying mean-fields, we adjusted pairing parameters for three parametrisations of the NLO Skyrme EDF that differ in their effective mass and for one parametrisation of the N2LO Skyrme EDF that yields a more intricate momentum dependence of the mean fields than the standard NLO parameter sets. For each of these, the parameters of the LO local pairing EDF were adjusted to a set of gaps $\Delta_q(k_{\lambda,q})$ at the chemical potential that covers a wide range of densities of symmetric infinite nuclear matter and were obtained with either of the two reference calculations. The main observations of our study are

1. The pairing gap in INM can be used as a proxy to transfer the global performance of a given combination of Skyrme and LO pairing parameter sets for finite nuclei to a Skyrme parameter set with different effective mass. This is most useful when generating families of Skyrme parametrisations that have systematically varied effective mass, or that are of different order in gradients, in particular in view of the robustness and numerical simplicity of HFB calculations of INM.
2. Using our adjustment strategy, global trends of the odd-even staggering of masses and rotational moments of inertia are described with very similar quality across parameter sets. Nonetheless, there remain local differences between the performance of the such adjusted combined Skyrme and pairing parametrisations for specific nuclei. These can be attributed to deficiencies in the description of single-particle spectra that are differently pronounced for each of the four parameter sets used here, and also to differences in the size of time-odd terms in the ph part of the EDF. Because of the interdependencies between the parameters of the Skyrme ph EDF, for standard NLO EDFs some of the latter are correlated

to the effective mass. For an improved modelling of the odd-even staggering of nuclear masses and rotational moments of inertia it is therefore not entirely sufficient to fine-tune the effective pairing interacting, but also to better control shell structure and time-odd terms as predicted by the ph part of the EDF.

3. By contrast, when attempting to replicate the pairing properties of a finite-range interaction with a local pairing EDF, it is not sufficient to reproduce the density dependence of the pairing gap $\Delta_q(k_{\lambda,q})$ at the chemical potential of INM. The main reason is that the matrix elements Δ_k from finite-range interactions have a strong momentum dependence that is not captured by the gap at $k_{\lambda,q}$. For the specific case of pairing matrix elements from Gogny D1S, the mapping onto a LO pairing EDF yields much stronger pairing correlations than the original Gogny force, which then overestimates pairing gaps in finite nuclei.
4. A similar mismatch for the pairing properties of finite nuclei can be expected when trying to map the gaps at the chemical potential obtained from more microscopic calculations. In either case, this can possibly be remedied by adding gradient terms to the pairing EDF that are only active in inhomogeneous systems, but at the expense of having to adjust again the pairing EDF to properties of finite nuclei. Doing so can be a meaningful, even mandatory, strategy when aiming at a simultaneous modelling of nuclei and nuclear matter as found in astrophysical objects, and has already been exploited in Refs. [59–62]. But for models aiming primarily at finite nuclei, being obliged to do so brings back the difficulty that we wanted to avoid in the first place.
5. To reproduce a given infinite-matter reference calculation for $\Delta_q(k_{\lambda,q})$ for ph interactions with different effective mass, one has in general to readjust all of the three parameters of the LO pairing EDF that control strength, volume-to-surface ratio, and power of the density dependence.
6. For parametrisations of the pairing EDFs with very small values for the power of the density dependence we find a nonphysical transition to a Bose-Einstein condensate of di-nucleons at low density in INM. This signals a spurious instability of the effective interaction that leads to unrealistic results for finite nuclei. The same instability can also be found for more complex pairing interactions [118]. The conditions for its appearance will be analysed elsewhere.

Besides the practical points already mentioned above, there are also some more conceptual issues that need to be clarified by future work. These concern

1. The transfer of the predictive power for pairing properties of finite nuclei between different *types* of pairing EDFs. Until there is a satisfying answer, our procedure for the parameter adjustment relies on having a predictive parametrisation for each given type of pairing EDF to start with.
2. The generalisation of the procedure proposed here to more general local pairing EDFs with kinetic and gradient terms. Such EDFs generate a momentum dependence of the Δ_k , but with reasonable parametrisations their variations is much smaller than what is found for finite-range interactions.
3. The strategy to set up reference calculations for the pairing gap in INM. There is no reason to believe that the gaps from the phenomenological SLy4+ULB parametrisation of the pairing EDF that we successfully employ as a reference is an optimal one. Our observation that the momentum dependence of the gaps Δ_k in INM has a significant impact on the pairing properties of nuclei can be expected to also apply to calculations of the pairing gap in nuclear matter from first principles. In fact, when solely aiming at the best effective modelling of pairing correlations in finite nuclei at the HFB level, in view of the different correlation modes of INM and finite nuclei, it is even not evident that a reference HFB calculation of INM has to give a realistic microscopic description of pairing gaps in INM itself.

In spite of these remaining questions, the strategy to transfer the pairing properties of SLy4+ULB to other Skyrme parametrisations proposed here has already been successfully used for the description of nuclear phenomena across the chart of nuclei, and this also for many Skyrme parameter sets not included in the analysis presented here.

Acknowledgements

Illuminating discussions on various aspects of nuclear pairing that we had over the years with Jacek Dobaczewski, Paul-Henri Heenen, Jacques Meyer, and Wouter Ryssens that inspired part of this work are gratefully acknowledged. The computations were performed using HPC resources from the CC-IN2P3 of the CNRS.

Appendix A: Solving the HFB equations for homogeneous infinite nuclear matter

In this appendix, we sketch how the usual representation of general HFB theory as discussed in [1, 47] simplifies for the case of 1S_0 pairing correlations in homogeneous infinite nuclear matter.

In INM, the spatial part of a nucleons' single-particle wave function is an eigenstate of momentum, i.e. a plane wave. For 1S_0 pairing correlations, the Bogoliubov transformation then only mixes single-particle states with \mathbf{k} and spin σ and their time-reversed states with $-\mathbf{k}$ and spin $-\sigma$ (as usual "spin" will be used synonymously for spin projection). With this, the single-particle states remain eigenstates of the isospin operator $\hat{\tau}_3$ and can be chosen to be eigenstates of $\hat{\sigma}_z$. As a consequence, the full spinors representing single-particle states in INM can be chosen as

$$\begin{aligned}\Psi_{\mathbf{k},\sigma,q}(\mathbf{r}) &= \langle \mathbf{r} | a_{\mathbf{k}\sigma q}^\dagger | - \rangle = \psi_{\mathbf{k}\sigma q}(\mathbf{r}) \chi_\sigma \xi_q \\ &= \frac{1}{(2\pi)^{3/2}} e^{+i\mathbf{k}\cdot\mathbf{r}} \chi_\sigma \xi_q,\end{aligned}\quad (\text{A.1})$$

where we distinguish between the full spinor $\Psi_{\mathbf{k}\sigma q}(\mathbf{r})$ in spin-isospin space and the spatial wave function of its spin-isospin components $\psi_{\mathbf{k}\sigma q}(\mathbf{r})$. The χ_σ and ξ_q are unit spinors in spin- and isospin-1/2 spaces, respectively

$$\chi_+ = \begin{pmatrix} 1 \\ 0 \end{pmatrix}_\sigma \quad \chi_- = \begin{pmatrix} 0 \\ 1 \end{pmatrix}_\sigma, \quad (\text{A.2})$$

$$\xi_n = \begin{pmatrix} 1 \\ 0 \end{pmatrix}_\tau \quad \xi_p = \begin{pmatrix} 0 \\ 1 \end{pmatrix}_\tau, \quad (\text{A.3})$$

with

$$\hat{\sigma}_z \chi_\sigma = \sigma \chi_\sigma, \quad \hat{\sigma}^2 \chi_\sigma = 3 \chi_\sigma, \quad (\text{A.4})$$

$$\hat{\tau}_3 \xi_n = +\xi_n, \quad \hat{\tau}_3 \xi_p = -\xi_p, \quad \hat{\tau}^2 \xi_q = 3 \xi_q. \quad (\text{A.5})$$

The basis states are pairwise connected by the time-reversal operator $\hat{T} = -i\sigma_y \hat{K}$ [162]

$$\begin{aligned}\hat{T} \Psi_{\mathbf{k},\sigma,q}(\mathbf{r}) &= \hat{T} \psi_{\mathbf{k},\sigma,q}(\mathbf{r}) \chi_\sigma \xi_q \\ &= \sigma \psi_{\mathbf{k},-\sigma,q}^*(\mathbf{r}) \chi_{-\sigma} \xi_q \\ &= \sigma \Psi_{-\mathbf{k},-\sigma,q}(\mathbf{r}),\end{aligned}\quad (\text{A.6})$$

which fixes the relative phase between states with $\pm\mathbf{k}$. We recall that for Fermionic single-particle states one has $\hat{T}^2 \Psi_{\mathbf{k},\sigma,q}(\mathbf{r}) = -\Psi_{\mathbf{k},\sigma,q}(\mathbf{r})$ [162]. To better follow the phase factors, we continue to use a notation with separate momentum and spin indices. In specific matrix elements, $\sigma = +1$ is indicated by \uparrow , and $\sigma = -1$ by \downarrow . In the canonical basis of the HFB problem, the Bogoliubov quasiparticle vacuum takes the form of a BCS state [47], which for INM can be written as

$$|\text{BCS}_q\rangle = \prod_{\mathbf{k}} (u_{\mathbf{k},q} + v_{\mathbf{k},q} a_{\mathbf{k}\uparrow q}^\dagger a_{-\mathbf{k}\downarrow q}^\dagger) | - \rangle. \quad (\text{A.7})$$

This expression is schematic in so far as in INM the product over \mathbf{k} is over a continuous spectrum of momenta \mathbf{k} that have all possible orientations in space, with states having the same absolute value of $k = |\mathbf{k}|$

being degenerate and having the same occupation amplitudes $u_{k,q}$ and $v_{k,q}$.

With the symmetry choices made here, the canonical basis can be chosen to be equal to the basis of eigenstates of the single-particle Hamiltonian, such that for homogeneous INM the HFB approach becomes numerically equivalent to a HF+BCS calculation. Some papers on the mean-field description of pairing correlations in INM even go one step further and neglect the feedback of pairing correlations on the mean-fields and only solve the gap equation of BCS theory for fixed single-particle spectrum. This, however, is not what is done here. The rest of this appendix outlines how symmetry considerations can be used to construct closed expressions for the matrix elements $u_{q,k}$ and $v_{q,k}$ of the Bogoliubov transformation of full HFB theory in the canonical basis.

Note that, in contrast to the usual representation of BCS states for finite nuclei, the product in Eq. (A.7) runs over all \mathbf{k} and not just half of them. By contrast, the product is limited to half of the combinations of \mathbf{k} with spins σ , i.e. the product does not explicitly contain $a_{\mathbf{k}\downarrow q}^\dagger a_{-\mathbf{k}\uparrow q}^\dagger$: this operator is already implicitly contained in the many-body wave function through $a_{-\mathbf{k}\uparrow q}^\dagger a_{\mathbf{k}\downarrow q}^\dagger = -a_{\mathbf{k}\downarrow q}^\dagger a_{-\mathbf{k}\uparrow q}^\dagger$. Numerically, the continuous variable \mathbf{k} will be discretised with n_k points for its modulus, see Appendix C.

As we only consider $T = 1$ pairing between like nucleons, for sake of compact notation the rest of this subsection will be for a generic type of nucleons without keeping track of an isospin index. When treating asymmetric matter, the occupation amplitudes, the elements of the normal and anomalous density matrices, the pairing gaps, single-particle energies and chemical potentials will have of course have different values for protons and neutrons.

The usual sign change in v_k when going to the conjugate state concerns the occupation amplitude of the state with opposite \mathbf{k} and opposite spin (for which there is no explicit symbol with our choice for the representation of the formalism). The normalisation of the BCS state (A.7)

$$1 = \langle \text{BCS} | \text{BCS} \rangle = \prod_{\mathbf{k}} (u_{\mathbf{k}}^* u_{\mathbf{k}} + v_{\mathbf{k}}^* v_{\mathbf{k}}) \quad (\text{A.8})$$

leads to the condition $|u_{\mathbf{k}}|^2 + |v_{\mathbf{k}}|^2 = 1$ for all \mathbf{k} . The $u_{\mathbf{k}}$ and $v_{\mathbf{k}}$ can in general be complex. Up to a further common phase of both $u_{\mathbf{k}}$ and $v_{\mathbf{k}}$, a possible choice is [116, 163]

$$u_{\mathbf{k}} = \sin(\vartheta_{\mathbf{k}}), \quad (\text{A.9})$$

$$v_{\mathbf{k}} = e^{i\varphi_{\mathbf{k}}} \cos(\vartheta_{\mathbf{k}}). \quad (\text{A.10})$$

with $0 \leq \vartheta_{\mathbf{k}} \leq \pi$ and $0 \leq \varphi_{\mathbf{k}} \leq 2\pi$. As we are interested only in systems with a single gap in the $S = 0$ channel

for a given nucleon species, we can choose $\varphi_k = 0$ for all \mathbf{k} , i.e. u_k and v_k being real without loss of generality [116, 163]. When $\bar{\mu}$ labels the time-reversed state of μ , the normal and anomalous density matrices are given by [1, 47]

$$\begin{aligned}\rho_{\mu\nu} &\equiv \langle \text{BCS} | a_\nu^\dagger a_\mu | \text{BCS} \rangle = (V^* V^T)_{\mu\nu} = v_\mu^2 \delta_{\mu\nu}, \\ \kappa_{\mu\nu} &\equiv \langle \text{BCS} | a_\nu a_\mu | \text{BCS} \rangle = (V^* U^T)_{\mu\nu} = v_\mu u_\nu \delta_{\nu\bar{\mu}}, \\ \kappa_{\mu\nu}^* &\equiv \langle \text{BCS} | a_\mu^\dagger a_\nu^\dagger | \text{BCS} \rangle = v_\mu u_\nu \delta_{\nu\bar{\mu}}.\end{aligned}\quad (\text{A.11})$$

For INM the non-vanishing elements of the ρ and κ matrices become

$$\begin{aligned}\rho_{\pm\mathbf{k}\sigma, \pm\mathbf{k}\sigma} &\equiv \langle \text{BCS} | a_{\pm\mathbf{k}\sigma}^\dagger a_{\pm\mathbf{k}\sigma} | \text{BCS} \rangle \\ &= V_{+\mathbf{k}+\sigma, -\mathbf{k}-\sigma} V_{+\mathbf{k}+\sigma, -\mathbf{k}-\sigma} \\ &= v_k^2,\end{aligned}\quad (\text{A.12})$$

$$\begin{aligned}\kappa_{+\mathbf{k}\uparrow, -\mathbf{k}\downarrow} &\equiv \langle \text{BCS} | a_{-\mathbf{k}\downarrow} a_{+\mathbf{k}\uparrow} | \text{BCS} \rangle \\ &= V_{+\mathbf{k}\uparrow, -\mathbf{k}\downarrow} U_{-\mathbf{k}\downarrow, -\mathbf{k}\downarrow} \\ &= +u_k v_k,\end{aligned}\quad (\text{A.13})$$

$$\begin{aligned}\kappa_{-\mathbf{k}\downarrow, +\mathbf{k}\uparrow} &\equiv \langle \text{BCS} | a_{+\mathbf{k}\uparrow} a_{-\mathbf{k}\downarrow} | \text{BCS} \rangle \\ &= V_{-\mathbf{k}\downarrow, +\mathbf{k}\uparrow} U_{+\mathbf{k}\uparrow, +\mathbf{k}\uparrow} \\ &= -u_k v_k,\end{aligned}\quad (\text{A.14})$$

$$\begin{aligned}\kappa_{-\mathbf{k}\uparrow, +\mathbf{k}\downarrow} &\equiv \langle \text{BCS} | a_{+\mathbf{k}\downarrow} a_{-\mathbf{k}\uparrow} | \text{BCS} \rangle \\ &= V_{-\mathbf{k}\uparrow, +\mathbf{k}\downarrow} U_{+\mathbf{k}\downarrow, +\mathbf{k}\downarrow} \\ &= +u_k v_k,\end{aligned}\quad (\text{A.15})$$

$$\begin{aligned}\kappa_{+\mathbf{k}\downarrow, -\mathbf{k}\uparrow} &\equiv \langle \text{BCS} | a_{-\mathbf{k}\uparrow} a_{+\mathbf{k}\downarrow} | \text{BCS} \rangle \\ &= V_{+\mathbf{k}\downarrow, -\mathbf{k}\uparrow} U_{-\mathbf{k}\uparrow, -\mathbf{k}\uparrow} \\ &= -u_k v_k,\end{aligned}\quad (\text{A.16})$$

and zero otherwise. The U and V matrices are the usual building blocks of the Bogoliubov transformation [1, 47, 115]. In addition, with the choice $\varphi_k = 0$ for the phases of v_k , the matrix elements of ρ and κ are real with

$$\kappa_{\mathbf{k}\sigma, \mathbf{k}'\sigma'}^* \equiv \langle \text{BCS} | a_{\mathbf{k}\sigma}^\dagger a_{\mathbf{k}'\sigma'}^\dagger | \text{BCS} \rangle = \kappa_{\mathbf{k}\sigma, \mathbf{k}'\sigma'}.\quad (\text{A.17})$$

From these relations, the U and V matrices of the Bogoliubov transformation in the canonical basis can be constructed. In the canonical basis, one of these has to be symmetric and the other skew-symmetric [1, 47]. Equations (A.9) and (A.10) follow the usual convention where U is the symmetric matrix and V the skew-symmetric one. In addition, these relations follow the most common phase convention where in the canonical basis the symmetric matrix U is chosen to be positive semi-definite. The matrix elements of the skew-symmetric matrix V then will not have a universal sign. The full U and V matrices are block diagonal in 2×2 matrices that connect single-particle states linked by time-reversal. For given $\pm\mathbf{k}$ there are two such submatrices which each consist of the two single-particle

states that are coupled in the two-body wave functions. These two-by-two blocks become

$$\begin{pmatrix} U_{+\mathbf{k}\uparrow, +\mathbf{k}\uparrow} & U_{+\mathbf{k}\uparrow, -\mathbf{k}\downarrow} \\ U_{-\mathbf{k}\downarrow, +\mathbf{k}\uparrow} & U_{-\mathbf{k}\downarrow, -\mathbf{k}\downarrow} \end{pmatrix} = \begin{pmatrix} u_k & 0 \\ 0 & u_k \end{pmatrix},\quad (\text{A.18})$$

$$\begin{pmatrix} V_{+\mathbf{k}\uparrow, +\mathbf{k}\uparrow} & V_{+\mathbf{k}\uparrow, -\mathbf{k}\downarrow} \\ V_{-\mathbf{k}\downarrow, +\mathbf{k}\uparrow} & V_{-\mathbf{k}\downarrow, -\mathbf{k}\downarrow} \end{pmatrix} = \begin{pmatrix} 0 & +v_k \\ -v_k & 0 \end{pmatrix},\quad (\text{A.19})$$

and

$$\begin{pmatrix} U_{-\mathbf{k}\uparrow, -\mathbf{k}\uparrow} & U_{-\mathbf{k}\uparrow, +\mathbf{k}\downarrow} \\ U_{+\mathbf{k}\downarrow, -\mathbf{k}\uparrow} & U_{+\mathbf{k}\downarrow, +\mathbf{k}\downarrow} \end{pmatrix} = \begin{pmatrix} u_k & 0 \\ 0 & u_k \end{pmatrix},\quad (\text{A.20})$$

$$\begin{pmatrix} V_{-\mathbf{k}\uparrow, -\mathbf{k}\uparrow} & V_{-\mathbf{k}\uparrow, +\mathbf{k}\downarrow} \\ V_{+\mathbf{k}\downarrow, -\mathbf{k}\uparrow} & V_{+\mathbf{k}\downarrow, +\mathbf{k}\downarrow} \end{pmatrix} = \begin{pmatrix} 0 & +v_k \\ -v_k & 0 \end{pmatrix},\quad (\text{A.21})$$

Note that the signs represent the relative phases between the non-zero elements of the V matrix as they enter the definition of the BCS state (A.7), but they do not indicate the actual sign of the *numerical* value of $\pm v_k$. The numerical value of v_k is determined by the sign of the gap, see Eq. (A.39), such that $-v_k$ can actually be positive and $+v_k$ be negative.

The u_k and v_k are determined by the HFB equations for the quasiparticle wave functions [1, 47, 115]

$$\begin{pmatrix} h - \lambda & \Delta \\ -\Delta^* & -h^* + \lambda \end{pmatrix} \begin{pmatrix} U \\ V \end{pmatrix} = E \begin{pmatrix} U \\ V \end{pmatrix},\quad (\text{A.22})$$

for each nucleon species $q = n, p$, where λ is a Lagrange multiplier for the adjustment of the average particle number per volume (i.e. of the density) and where the matrices h and Δ are given by [1, 47, 115]

$$\hat{h}_{\nu\mu} \equiv \frac{\delta E}{\delta \rho_{\mu\nu}}, \quad \Delta_{\nu\mu} \equiv \frac{\delta E}{\delta \kappa_{\nu\mu}^*}, \quad \Delta_{\nu\mu}^* \equiv \frac{\delta E}{\delta \kappa_{\nu\mu}}.\quad (\text{A.23})$$

Even when the numerical values of the $\kappa_{\nu\mu}$ are real and therefore equal to those of $\kappa_{\nu\mu}^*$, for the derivation of the HFB equations one has to treat $\kappa_{\nu\mu} = -\kappa_{\mu\nu}$ and $\kappa_{\nu\mu}^* = -\kappa_{\mu\nu}^*$ as independent degrees of freedom that are varied separately, otherwise one does not obtain the usual matrix structure of the HFB equation.

Because of the definitions (A.23), the matrices $\hat{h}_{\mathbf{k}\sigma, \mathbf{k}\sigma}$ and $\Delta_{-\mathbf{k}-\sigma, +\mathbf{k}+\sigma}$ have the same 2×2 block structure between single-particle states linked by time-reversal like the ρ and κ matrices, respectively

$$\varepsilon_k \equiv \hat{h}_{\mathbf{k}\sigma, \mathbf{k}\sigma} = \frac{\delta E}{\delta \rho_{\mathbf{k}\sigma, \mathbf{k}\sigma}}\quad (\text{A.24})$$

$$\Delta_k \equiv \Delta_{-\mathbf{k}\downarrow, +\mathbf{k}\uparrow} = \frac{\delta E_{\text{pair}}}{\delta \kappa_{-\mathbf{k}\downarrow, +\mathbf{k}\uparrow}^*},\quad (\text{A.25})$$

$$\Delta_k^* \equiv \Delta_{-\mathbf{k}\downarrow, +\mathbf{k}\uparrow}^* = \frac{\delta E_{\text{pair}}}{\delta \kappa_{-\mathbf{k}\downarrow, +\mathbf{k}\uparrow}}.\quad (\text{A.26})$$

where we use directly that the matrix representing the single-particle Hamiltonian is diagonal by construction

and replace its non-vanishing matrix elements by its eigenvalues ε_k that will be called single-particle energies. That the gaps Δ_k are elements of skew-symmetric matrices is again completely hidden by the compact notation

$$\begin{aligned}\Delta_k &= +\Delta_{-\mathbf{k}\downarrow,+\mathbf{k}\uparrow} = -\Delta_{+\mathbf{k}\uparrow,-\mathbf{k}\downarrow} \\ &= +\Delta_{+\mathbf{k}\downarrow,-\mathbf{k}\uparrow} = -\Delta_{-\mathbf{k}\uparrow,+\mathbf{k}\downarrow},\end{aligned}\quad (\text{A.27})$$

$$\begin{aligned}\left(\begin{array}{cccc} h_{+\mathbf{k}\uparrow,+\mathbf{k}\uparrow} - \lambda & 0 & 0 & \Delta_{+\mathbf{k}\uparrow,-\mathbf{k}\downarrow} \\ 0 & h_{-\mathbf{k}\downarrow,-\mathbf{k}\downarrow} - \lambda & \Delta_{-\mathbf{k}\downarrow,+\mathbf{k}\uparrow} & 0 \\ 0 & -\Delta_{+\mathbf{k}\uparrow,-\mathbf{k}\downarrow} & -h_{+\mathbf{k}\uparrow,+\mathbf{k}\uparrow} + \lambda & 0 \\ -\Delta_{-\mathbf{k}\downarrow,+\mathbf{k}\uparrow} & 0 & 0 & -h_{-\mathbf{k}\downarrow,-\mathbf{k}\downarrow} + \lambda \end{array}\right) \begin{pmatrix} U_{+\mathbf{k}\uparrow,+\mathbf{k}\uparrow} & U_{+\mathbf{k}\uparrow,-\mathbf{k}\downarrow} \\ U_{-\mathbf{k}\downarrow,+\mathbf{k}\uparrow} & U_{-\mathbf{k}\downarrow,-\mathbf{k}\downarrow} \\ V_{+\mathbf{k}\uparrow,+\mathbf{k}\uparrow} & V_{+\mathbf{k}\uparrow,-\mathbf{k}\downarrow} \\ V_{-\mathbf{k}\downarrow,+\mathbf{k}\uparrow} & V_{-\mathbf{k}\downarrow,-\mathbf{k}\downarrow} \end{pmatrix} \\ = E_k \begin{pmatrix} U_{+\mathbf{k}\uparrow,+\mathbf{k}\uparrow} & U_{+\mathbf{k}\uparrow,-\mathbf{k}\downarrow} \\ U_{-\mathbf{k}\downarrow,+\mathbf{k}\uparrow} & U_{-\mathbf{k}\downarrow,-\mathbf{k}\downarrow} \\ V_{+\mathbf{k}\uparrow,+\mathbf{k}\uparrow} & V_{+\mathbf{k}\uparrow,-\mathbf{k}\downarrow} \\ V_{-\mathbf{k}\downarrow,+\mathbf{k}\uparrow} & V_{-\mathbf{k}\downarrow,-\mathbf{k}\downarrow} \end{pmatrix}\end{aligned}\quad (\text{A.28})$$

Unlike the case of finite nuclei for which one has a full $2n_k \times 2n_k$ matrix problem that in general has to be solved with numerical diagonalisation methods, the solutions of the HFB problem (A.28) can be given in a closed form.

Substituting the matrix elements of the quasiparticle Hamiltonian by (A.24), (A.25), and (A.26), as well as the elements of U and V by (A.18) and (A.19), the HFB equation (A.28) is equivalent to the two coupled equations

$$(\varepsilon_k - \lambda)u_k + \Delta_k v_k = E_k u_k, \quad (\text{A.29})$$

$$\Delta_k u_k - (\varepsilon_k - \lambda)v_k = E_k v_k. \quad (\text{A.30})$$

The eigenvalues E_k of Eq. (A.28) can be deduced from the squares of Eqs. (A.29) and (A.30)

$$(\varepsilon_k - \lambda)^2 u_k^2 + 2(\varepsilon_k - \lambda)\Delta_k u_k v_k + \Delta_k^2 v_k^2 = E_k^2 u_k^2, \quad (\text{A.31})$$

$$\Delta_k^2 u_k^2 - 2(\varepsilon_k - \lambda)\Delta_k u_k v_k + (\varepsilon_k - \lambda)^2 v_k^2 = E_k^2 v_k^2, \quad (\text{A.32})$$

Taking the sum of these equations and substituting the resulting $u_k^2 + v_k^2$ factor in front of each non-vanishing term by 1 this yields

$$(\varepsilon_k - \lambda)^2 + \Delta_k^2 = E_k^2 \quad (\text{A.33})$$

Recalling that the elementary excitations of the HFB ground state are given by the quasiparticle energies [1, 47] that each bring an excitation energy of E_k , the paired HFB quasiparticle vacuum with lowest energy is necessarily the state from which one can only create excitations with positive quasiparticle energy, see [47]

and therefore has to be explicitly kept track of with suitable phase factors. For a pairing interaction that at a given k is attractive, and our choice of phases, Δ_k takes a positive value.

The matrix representation of the HFB Hamiltonian in the canonical basis of homogeneous non-polarised INM therefore decomposes into 2×2 blocks that only mix single-particle states with $\pm \mathbf{k}$ and opposite spin

for a detailed discussion. Consequently, the quasiparticle energies of the solutions of the HFB equations that give the ground state of paired INM are given by

$$E_k = +\sqrt{(\varepsilon_k - \lambda)^2 + \Delta_k^2}. \quad (\text{A.34})$$

The values of the amplitudes u_k and v_k can also be deduced from Eqs. (A.29) and (A.30). Multiplying (A.29) with v_k and (A.30) with u_k

$$(\varepsilon_k - \lambda)u_k v_k + \Delta_k v_k^2 = E_k u_k v_k, \quad (\text{A.35})$$

$$\Delta_k u_k^2 - (\varepsilon_k - \lambda)u_k v_k = E_k u_k v_k, \quad (\text{A.36})$$

and taking the sum of these two equations yields

$$u_k v_k = \frac{\Delta_k}{2E_k}, \quad (\text{A.37})$$

where we used once again that $u_k^2 + v_k^2 = 1$. For the phase convention $u_k \geq 0$, the numerical value of v_k has the same sign as Δ_k

$$u_k = +\sqrt{u_k^2}, \quad (\text{A.38})$$

$$v_k = \text{sign}(\Delta_k)\sqrt{v_k^2}. \quad (\text{A.39})$$

In the most general case, the sign of the numerical value of $u_k^2 - v_k^2$ is also fixed by the sign of E_k . Assuming $\Delta_k \neq 0$ and inserting (A.33) for E_k^2 back into either Eq. (A.29) or (A.30), yields in both cases the relation

$$2(\varepsilon_k - \lambda)u_k v_k = \Delta_k (u_k^2 - v_k^2). \quad (\text{A.40})$$

Inserting Eq. (A.37) into Eq. (A.40), one finds

$$(u_k^2 - v_k^2) = \frac{\varepsilon_k - \lambda}{E_k}. \quad (\text{A.41})$$

For positive E_k , the sign of $(u_k^2 - v_k^2)$, and thereby the relative size of u_k^2 and v_k^2 , is determined by the sign of $(\varepsilon_k - \lambda)$: for $\varepsilon_k > \lambda$ one has $u_k^2 > v_k^2$, whereas for $\varepsilon_k < \lambda$ one finds $u_k^2 < v_k^2$.

The occupation probabilities can be directly calculated from Eq. (A.41) without passing through quadratic equations for v_k^2 and u_k^2 that would require an analysis of the solution to be kept. Using once more that $u_k^2 + v_k^2 = 1$ to substitute either v_k^2 or u_k^2 in Eq. (A.41), one finds for the occupation numbers that

$$1 - 2v_k^2 = \frac{\varepsilon_k - \lambda}{E_k}, \quad (\text{A.42})$$

$$2u_k^2 - 1 = \frac{\varepsilon_k - \lambda}{E_k}, \quad (\text{A.43})$$

which, inserting eq. (A.34), leads to the well-known expressions for the HFB ground state [1]

$$v_k^2 = \frac{1}{2} \left[1 - \frac{\varepsilon_k - \lambda}{\sqrt{(\varepsilon_k - \lambda)^2 + \Delta_k^2}} \right], \quad (\text{A.44})$$

$$u_k^2 = \frac{1}{2} \left[1 + \frac{\varepsilon_k - \lambda}{\sqrt{(\varepsilon_k - \lambda)^2 + \Delta_k^2}} \right]. \quad (\text{A.45})$$

Positive quasiparticle energy $E_k > 0$ therefore implies that $v_k^2 < 1/2$ for $\varepsilon_k > \lambda$ and $v_k^2 > 1/2$ for $\varepsilon_k < \lambda$ without the need for additional considerations.

With this, for given mean-field potentials and chemical potential λ , the n_k solutions of HFB equations for INM with positive eigenvalues can be directly determined from the matrix elements $h_{\mathbf{k}\sigma, \mathbf{k}\sigma}$ and $\Delta_{\mathbf{k}\sigma, -\mathbf{k}-\sigma}$ without the need to numerically solve a system of coupled integro-differential equations for the quasiparticle wave functions. The eigenvalues are given by Eq. (A.34), whereas Eqs. (A.18), (A.19), (A.39), and (A.38) define the eigenvectors in the plane-wave basis (A.1). Note that the spatial wave functions of the upper and lower components of the quasiparticle wave functions are plane waves with opposite \mathbf{k} .

We note in passing that there is a second set of n_k solutions of the HFB equations with negative quasiparticle energies [47, 115] for which the roles of U and V are exchanged. These are only relevant when either solving the HFB equations for explicit quasiparticle excitations or when solving the HFB equations at finite temperature, neither of which is needed here.

Appendix B: Implementing the HFB equations for the Skyrme energy density functional

To numerically solve the HFB equations in INM for the Skyrme EDF, the single-particle energies ε_k and the gaps Δ_k have to be calculated for this specific EDF. The relevant expressions are given in this appendix, using

the notation of Ref. [34]. Unlike Appendix A, the isospin indices will again be explicitly given.

Appendix B.1: Local densities

With the symmetries of homogeneous isotropic non-polarised INM, all normal and spin currents are zero, $C_q^{A,B} = C_q^{A,B\sigma} = 0$, as are all spin densities $D_q^{A,B\sigma} = 0$. As a consequence, for standard NLO Skyrme EDFs, one just has to calculate the local density $D_q^{1,1}$ and the local scalar kinetic density $D_q^{(\nabla, \nabla)}$ of protons and neutrons $q = p, n$

$$D_q^{1,1} = \sum_{\sigma} \int d^3k \rho_{\mathbf{k}\sigma q, \mathbf{k}\sigma q} |\psi_{\mathbf{k}\sigma q}(\mathbf{r})|^2, \quad (\text{B.46})$$

$$D_q^{(\nabla, \nabla)} = \sum_{\sigma} \int d^3k \rho_{\mathbf{k}\sigma q, \mathbf{k}\sigma q} \mathbf{k}^2 |\psi_{\mathbf{k}\sigma q}(\mathbf{r})|^2. \quad (\text{B.47})$$

The numerical evaluation of the momentum-space integrals is sketched in Appendix C. For N2LO EDFs, one has in addition to construct the kinetic tensor density $D_{\mu\nu q}^{\nabla, \nabla}$ that in isotropic INM only has diagonal components that are all equal $D_{xx, q}^{\nabla, \nabla} = D_{yy, q}^{\nabla, \nabla} = D_{zz, q}^{\nabla, \nabla}$

$$\begin{aligned} D_{\mu\nu, q}^{\nabla, \nabla} &= \sum_{\sigma} \int d^3k \rho_{\mathbf{k}\sigma q, \mathbf{k}\sigma q} k_{\mu} k_{\nu} |\psi_{\mathbf{k}\sigma q}(\mathbf{r})|^2 \\ &= \frac{1}{3} \delta_{\mu\nu} D_q^{(\nabla, \nabla)}, \end{aligned} \quad (\text{B.48})$$

and the higher-order scalar kinetic density

$$D_q^{\Delta, \Delta} = \sum_{\sigma} \int d^3k \rho_{\mathbf{k}\sigma q, \mathbf{k}\sigma q} \mathbf{k}^4 |\psi_{\mathbf{k}\sigma q}(\mathbf{r})|^2. \quad (\text{B.49})$$

For all of these, the matrix elements of $\rho_{\mathbf{k}\sigma q, \mathbf{k}\sigma q}$ are simply given by the occupation numbers v_k^2 of the single-particle states of the nucleon species q calculated from Eq. (A.44).

From the proton and neutron densities, the usual isoscalar and isovector densities that enter the compact formulation of the Skyrme EDF are obtained as

$$D_0^{A,B} = D_n^{A,B} + D_p^{A,B}, \quad (\text{B.50})$$

$$D_1^{A,B} = D_n^{A,B} - D_p^{A,B}. \quad (\text{B.51})$$

Appendix B.2: Local pair densities

From the symmetries assumed here, it also follows that many of the local pair densities are zero, i.e. $\tilde{C}_q^{A,B} = \tilde{C}_q^{A,B\sigma} = \tilde{D}_q^{A,B\sigma} = 0$. In addition, with the choice of real occupation amplitudes (A.9) and (A.10), all non-vanishing local pair densities are real [34].

For the pair EDF (1) used here, only the local pair density $\tilde{D}_q^{1,1}$ of protons and neutrons needs to be evaluated

$$\begin{aligned}\tilde{D}_q^{1,1} &= \sum_{\sigma} (-\sigma) \langle \text{BCS} | a_{\mathbf{r}-\sigma} a_{\mathbf{r}\sigma} | \text{BCS} \rangle \\ &= \sum_{\sigma} \int d^3k \kappa_{\mathbf{k}\sigma, -\mathbf{k}-\sigma} (-\sigma) \psi_{\mathbf{k}\sigma q}(\mathbf{r}) \psi_{-\mathbf{k}-\sigma q}(\mathbf{r}) \\ &= 2 \int d^3k u_k v_k |\psi_{\mathbf{k}\sigma q}(\mathbf{r})|^2,\end{aligned}\quad (\text{B.52})$$

where we used that for a time-reversal invariant system it follows from Eq. (A.6) that $-\sigma \psi_{-\mathbf{k}-\sigma q}(\mathbf{r}) = \psi_{\mathbf{k}\sigma q}^*(\mathbf{r})$.

For convenience, the cutoff factors f_k^2 of Eq. (8) are absorbed into effective pair densities

$$\tilde{D}_q^{1,1} \rightarrow 2 \int d^3k u_k v_k f_k^2 |\psi_{\mathbf{k}\sigma q}(\mathbf{r})|^2,\quad (\text{B.53})$$

as done in Ref. [34]. Note that the sums and differences of the pair densities $\tilde{D}_q^{A,B}$ of protons and neutrons do not represent isoscalar and isovector objects; isoscalar and isovector pair densities have to be constructed differently [164], reason being that pair densities do not transform like hermitian matrices, but like two-body wave functions [34]. In fact, the pairing EDF of Eq. (1) actually represents the pairing energy in the $T = 1$ channel.

Appendix B.3: The energy density functional

The total energy of a piece of nuclear matter of volume V is obtained as the sum of kinetic energy, and the contributions of the time-even part of the Skyrme EDF at LO, NLO, and N2LO, as well as the pairing EDF

$$\begin{aligned}E &= \int_V d^3r \mathcal{E} \\ &= \int_V d^3r \left[\mathcal{E}_{\text{kin}} + \mathcal{E}_{\text{Sk},e}^{(0)} + \mathcal{E}_{\text{Sk},e}^{(2)} + \mathcal{E}_{\text{Sk},e}^{(4)} + \mathcal{E}_{\text{pair},e}^{(0)} \right].\end{aligned}\quad (\text{B.54})$$

Compared to the calculations of finite nuclei, the centre-of-mass correction vanishes, and the Coulomb interaction between protons is omitted.

As the total energy scales with V , it is more useful to look at the energy per particle, which equals the energy density divided by the total density $E/A = \mathcal{E}/\rho$, which for homogeneous INM are both numbers instead of spatial functions. The kinetic energy density is given by

$$\mathcal{E}_{\text{kin}} = \frac{\hbar^2}{2m} D_0^{(\nabla, \nabla)}.\quad (\text{B.55})$$

For the sake of keeping the calculation of INM simple, one is obliged to use the same mass m for protons and neutrons, even when using a parametrisation of the Skyrme EDF that was adjusted using their different physical masses. Otherwise the saturation point of INM is not in symmetric matter, which introduces numerous practical and conceptual difficulties.

For homogeneous INM all derivatives of local densities are zero. The few remaining LO, NLO, and N2LO contributions from the full energy density of the ph EDF as defined in Ref. [34] are then

$$\mathcal{E}_{\text{Sk},e}^{(0)} = \sum_{t=0,1} \left[A_{t,e}^{(0,1)} (D_t^{1,1})^2 + A_{t,e}^{(0,2)} (D_0^{1,1})^\alpha (D_t^{1,1})^2 \right],\quad (\text{B.56})$$

$$\mathcal{E}_{\text{Sk},e}^{(2)} = \sum_{t=0,1} A_{t,e}^{(2,2)} D_t^{1,1} D_t^{(\nabla, \nabla)},\quad (\text{B.57})$$

$$\begin{aligned}\mathcal{E}_{\text{Sk},e}^{(4)} &= \sum_{t=0,1} \left[A_{t,e}^{(4,2)} D_t^{1,1} D_t^{\Delta, \Delta} + A_{t,e}^{(4,3)} D_t^{(\nabla, \nabla)} D_t^{(\nabla, \nabla)} \right. \\ &\quad \left. + A_{t,e}^{(4,4)} \sum_{\mu\nu} D_{t,\mu\nu}^{\nabla, \nabla} D_{t,\mu\nu}^{\nabla, \nabla} \right].\end{aligned}\quad (\text{B.58})$$

The definition of the coupling constants $A_{t,e}^{(n,j)}$ in terms of the usual coupling constants t_i and x_i of the EDF generator is given in Ref. [34].

Appendix B.4: The single-particle Hamiltonian

In a plane wave basis, the matrix $h_{\mathbf{k}\sigma q, \mathbf{k}'\sigma' q'}$ that represents the single-particle Hamiltonian in INM is diagonal, such that the non-vanishing matrix elements are automatically its eigenvalues $\varepsilon_{\mathbf{k}\sigma q}$, usually called single-particle energies. For the Skyrme EDF used here, these are given by

$$\begin{aligned}h_{\mathbf{k}\sigma q, \mathbf{k}\sigma q} &= \frac{\delta \mathcal{E}}{\delta \rho_{\mathbf{k}\sigma q, \mathbf{k}\sigma q}^q} \\ &= \left(\frac{\hbar^2}{2m} + F_q^{(\nabla, \nabla)} \right) \mathbf{k}^2 + F_q^{1,1} \\ &\quad + \sum_{\mu} F_{q, \mu\mu}^{\nabla, \nabla} k_{\mu}^2 + F_q^{\Delta, \Delta} \mathbf{k}^2 \mathbf{k}^2,\end{aligned}\quad (\text{B.59})$$

where the potentials are defined as the functional derivatives of the interaction part of the EDF with respect to the local densities, $F_q^{A,B} \equiv \delta \mathcal{E} / \delta D_q^{A,B}$.

Because of the isotropy of non-polarised INM, all three remaining components to the N2LO kinetic tensor potential are actually equal $F_{q,xx}^{\nabla, \nabla} = F_{q,yy}^{\nabla, \nabla} = F_{q,zz}^{\nabla, \nabla}$, such that one can substitute the kinetic tensor term through $F_{q,xx}^{\nabla, \nabla} k_x^2 + F_{q,yy}^{\nabla, \nabla} k_y^2 + F_{q,zz}^{\nabla, \nabla} k_z^2 = F_{q, \mu\mu}^{\nabla, \nabla} \mathbf{k}^2$, where μ is the index of any component x , y , or z , and over which summation is not needed anymore.

Using the shorthand introduced in Ref. [34] for the combinations of coupling constants that appear in contributions from the same ($q' = q$) or the other ($q' \neq q$) nucleon species to the single-particle potentials

$$\begin{aligned} A_{qq',x}^{(i,j)} &= (A_{0,x}^{(i,j)} + A_{1,x}^{(i,j)}) \delta_{qq'} + (A_{0,x}^{(i,j)} - A_{1,x}^{(i,j)}) (1 - \delta_{qq'}) \\ &= A_{0,x}^{(i,j)} + (2\delta_{qq'} - 1) A_{1,x}^{(i,j)}, \end{aligned} \quad (\text{B.60})$$

the contribution from the Skyrme EDF to the potentials $F_q^{A,B}$ for the nucleon species $q = p, n$ that are associated with time-even densities through $F_q^{A,B} \equiv \delta \mathcal{E}_{\text{Sk}} / \delta D_q^{A,B}$ are given by

$$\begin{aligned} F_q^{1,1} &= \sum_{q'=p,n} \left[2 A_{qq',e}^{(0,1)} D_{q'}^{1,1} + 2 A_{qq',e}^{(0,2)} (D_0^{1,1})^\alpha D_{q'}^{1,1} \right. \\ &\quad \left. + A_{qq',e}^{(2,2)} D_{q'}^{(\nabla,\nabla)} + A_{qq',e}^{(4,2)} D_{q'}^{\Delta,\Delta} \right] \\ &\quad + \alpha A_{0,e}^{(0,2)} (D_0^{1,1})^{\alpha-1} (D_0^{1,1})^2 \\ &\quad + \alpha A_{1,e}^{(0,2)} (D_0^{1,1})^{\alpha-1} (D_1^{1,1})^2 \end{aligned} \quad (\text{B.61})$$

$$F_q^{(\nabla,\nabla)} = \sum_{q'=p,n} \left[A_{qq',e}^{(2,2)} D_{q'}^{1,1} + 2 A_{qq',e}^{(4,3)} D_{q'}^{(\nabla,\nabla)} \right], \quad (\text{B.62})$$

$$F_{q,\mu\nu}^{\nabla,\nabla} = \sum_{q'=p,n} 2 A_{qq',e}^{(4,4)} D_{q',\mu\nu}^{\nabla,\nabla}, \quad (\text{B.63})$$

$$F_q^{\Delta,\Delta} = \sum_{q'=p,n} A_{qq',e}^{(4,2)} D_{q'}^{1,1}. \quad (\text{B.64})$$

Appendix B.5: The effective mass of N2LO EDFs

For Skyrme EDFs at NLO, at given density and asymmetry the effective masses of neutrons and protons in infinite matter might be different, but they are identical for all nucleons of the same species, irrespective of their momentum. This is different for N2LO EDFs with their higher-order gradient terms. The effective k -mass is defined through a derivative of the single-particle Hamiltonian [165], that for non-relativistic EDFs can be expressed as

$$\begin{aligned} \frac{m}{m_q^*(k_0)} &= \frac{m}{\hbar^2 k_0} \frac{\partial}{\partial k} h_{\mathbf{k}\sigma q, \mathbf{k}\sigma q} \Big|_{k=k_0} \\ &= 1 + \frac{2m}{\hbar^2} \left(F_q^{(\nabla,\nabla)} + F_{q,\mu\mu}^{\nabla,\nabla} + 2F_q^{\Delta,\Delta} \mathbf{k}^2 \right). \end{aligned} \quad (\text{B.65})$$

where the index μ is again either x, y , or z . With this, the single-particle Hamiltonian (B.59) can be rewritten as

$$\begin{aligned} h_{\mathbf{k}\sigma q, \mathbf{k}\sigma q} &= \frac{\hbar^2}{2m_q^*(k)} \mathbf{k}^2 + F_q^{1,1} - F_q^{\Delta,\Delta} \mathbf{k}^4 \\ &= \frac{\hbar^2}{2m_q^*(k)} \mathbf{k}^2 + U_q(\mathbf{k}^2). \end{aligned} \quad (\text{B.66})$$

For NLO EDFs the higher-order potential $F_q^{\Delta,\Delta} = 0$ vanishes, such that the single-particle energy is the kinetic energy evaluated of nucleons with constant effective mass m_q^*/m plus a constant. For N2LO EDFs, however, the \mathbf{k}^4 contribution to the single-particle Hamiltonian is double-counted in the now k -dependent effective mass (B.65). It therefore has to be subtracted when rewriting $h_{\mathbf{k}\sigma q, \mathbf{k}\sigma q}$ in the form (B.66), meaning that both the effective mass and the effective potential $U_q(\mathbf{k}^2) = F_q^{1,1} - F_q^{\Delta,\Delta} \mathbf{k}^4$ become k dependent.

We note in passing that for finite-range interactions for which the effective mass emerges from the non-locality of the exchange term, one also naturally finds that both the effective mass and the potential depend on k in a manner that is much more involved than Eqs. (B.65) and (B.66).

Appendix B.6: The pairing EDF

In the notation of Ref. [34], for non-polarised homogeneous INM the LO pairing EDF of Eq. (1) becomes

$$\mathcal{E}_{\text{pair},e}^{(0)} = \sum_{q=p,n} \left[\tilde{A}_{qq}^{(0,1)} + \tilde{A}_{qq}^{(0,2)} (D_0^{1,1})^\sigma \right] \tilde{D}_q^{1,1*} \tilde{D}_q^{1,1}, \quad (\text{B.67})$$

where we keep the distinction between $\tilde{D}_q^{1,1}$ and $\tilde{D}_q^{1,1*}$ for the sake of a more transparent derivation of the pair potentials and gaps along the lines of the standard textbook discussion of the HFB equations [1, 47, 115] in spite of the possibility to choose all quantities to be real in the INM calculations reported here. The pair density $\tilde{D}_q^{1,1}$ entering Eq. (B.67) and all other relations in this section is the one with cutoffs defined in Eq. (B.53).

The compact coupling constants of Eq. (B.67) are related to the traditional ones of Eq. (1) through

$$\tilde{A}_{qq}^{(0,1)} = \frac{1}{4} V_0, \quad (\text{B.68})$$

$$\tilde{A}_{qq}^{(0,2)} = -\frac{\eta}{4\rho_{\text{ref}}^\sigma} V_0. \quad (\text{B.69})$$

For the pair potential $\tilde{F}_q^{1,1}$ this yields

$$\tilde{F}_q^{1,1} = \frac{\delta \mathcal{E}_{\text{pair},e}^{(0)}}{\delta \tilde{D}_q^{1,1*}} = \tilde{A}_{qq}^{(0,1)} \tilde{D}_q^{1,1} + \tilde{A}_{qq}^{(0,2)} (D_0^{1,1})^\sigma \tilde{D}_q^{1,1}, \quad (\text{B.70})$$

and the complex conjugate of this expression for $\tilde{F}_q^{1,1*}$. With this, the gaps Δ_k defined through Eq. (A.25) are given by

$$\Delta_k = \Delta_{-\mathbf{k}\downarrow, +\mathbf{k}\uparrow} = \frac{\delta E_{\text{pair}}}{\delta \kappa_{-\mathbf{k}\downarrow, +\mathbf{k}\uparrow}^*}$$

$$= \frac{\delta \mathcal{E}_{\text{pair},e}^{(0)}}{\delta \tilde{D}_q^{1,1*}} \frac{\delta \tilde{D}_q^{1,1*}}{\delta \kappa_{-\mathbf{k}-\downarrow,+\mathbf{k}}} = -f_k^2 \tilde{F}_q^{1,1}. \quad (\text{B.71})$$

The pairing EDF also adds a further contribution to $F_q^{1,1}$ of Eq. (B.61)

$$F_q^{1,1} = \frac{\delta \mathcal{E}_{\text{Sk},e}}{\delta D_q^{1,1}} + \sigma \tilde{A}_{qq}^{(0,2)} (D_0^{1,1})^{\sigma-1} \sum_{q'=p,n} |\tilde{D}_{q'}^{1,1}|^2 \quad (\text{B.72})$$

that is included in our calculations of INM.

Appendix C: Discretisation of momentum-space integrals

For isotropic INM as considered here, the 3d integral over a function $f(k)$ of the momentum can be reduced a 1d-integral that is evaluated with a numerical quadrature

$$\int d^3k f(k) = 4\pi \int dk k^2 f(k) \rightarrow 4\pi \sum_i w_i k_i^2 f(k_i) \quad (\text{C.73})$$

with integration weights w_i and abscissas k_i . The following considerations entered the set-up of the discretisation:

1. Because of the pairing cutoff (8), the integration can be stopped at some k_{max} that is sufficiently larger than the momentum at which the cutoff $f_{k,q}$ makes the gaps Δ_k fall to negligibly small values.
2. The occupation numbers v_k^2 are known to vary quickly around the chemical potential, whereas their values much more slowly approach 1 below or fall off to 0 above. The $u_k v_k$ factors multiplying pair densities behave similarly. To achieve better convergence of integrals weighted with either v_k^2 or $u_k v_k$ with respect to their numerical discretisation, it is therefore advantageous to have a denser mesh for momenta close to the chemical potentials λ_q , in particular in the weak-pairing limit when the Δ_k , and with that the interval over which v_k^2 falls from 1 to 0, become very small. To achieve this, for each nucleon species the numerical integration interval $[0, k_{\text{max},q}]$ is divided into four sub-intervals

$$\int dk \rightarrow \left[\int_0^{k_1} + \int_{k_1}^{k_2} + \int_{k_3}^{k_4} + \int_{k_4}^{k_5} \right] dk \quad (\text{C.74})$$

where $k_2 = k_{\lambda,q}$ is the momentum corresponding to the chemical potential and $k_3 = k_{\lambda,q} + \epsilon$. The values of k_1 and k_4 are the momenta corresponding to the single-particle energies $\varepsilon_{\lambda,q} \mp 0.2 \text{ MeV}$.

3. In asymmetric matter, the values of k_1, k_2, k_3, k_4 , and k_5 are different for protons and neutrons.
4. Setting the upper limit k_2 of the second interval to either $k_{\text{F},q}$ or $k_{\lambda,q}$, and to have the lower limit k_3 of the third interval at an only infinitesimally larger value permits the precise evaluation of the momentum-space integrals in the HF limit when pairing breaks down, such that $k_2 = k_{\lambda,q} = k_{\text{F},q}$ with $v_{k_2}^2 = 1$ and $v_{k_3}^2 = 0$.
5. If $k_{\lambda,q}$ does not fall on a boundary of a sub-interval of the numerical integration, one artificially enforces $u_k v_k \neq 0$ around the chemical potentials as the HF solution with $u_k v_k = 0$ that yields the targeted density cannot be numerically represented.
6. The numerical integration is performed with a composite Newton-Cotes quadrature with eight equidistant points in the sub-intervals. At given total number of integration points, using such higher-order quadrature formula yields a more precise description of local higher-order kinetic densities $D_q^{\nabla,\nabla}$ and $D_q^{\Delta,\Delta}$ than using a simple trapezoidal formula *at exactly the same numerical cost*.
7. For INM in the BCS phase and $k_{\lambda,q}^2 > 0$, these integrals are discretised with

$$n_{k_1} = \frac{n_k}{3} + 1 \quad \text{points in } [0, k_1], \quad (\text{C.75})$$

$$n_{k_2} = \frac{n_k}{6} \quad \text{points in } [k_1, k_2], \quad (\text{C.76})$$

$$n_{k_3} = \frac{n_k}{6} + 1 \quad \text{points in } [k_3, k_4], \quad (\text{C.77})$$

$$n_{k_4} = \frac{n_k}{3} \quad \text{points in } [k_4, k_5], \quad (\text{C.78})$$

such that the two discretisation points at k_1 and k_4 contribute to two of the sub-integrals.

8. In case of a BEC solution for the nucleon species q for which $k_{\lambda,q}$ is outside of the spectrum of physical plane-wave states, the integrals cannot be set up as described above. In this case, all four sub-integrals are discretised in equidistant steps from $k = 0$ up to a suitably chosen $k_{\text{max},q}$ above the pairing cutoff.
9. Because of setting up the integral with four regions that all are discretised with a composite eight-point quadrature and shared points on some of the boundaries, $n_k - 2$ has to be a multiple of 42. Calculations reported here were performed with in total 3782 discretisation points, which in the majority of cases are many more than needed to achieve numerical convergence, but this ensures convergence also in extreme cases.

Appendix D: Solution of the self-consistent problem

The HFB equations for INM can be solved with a straightforward simplification of the the two-basis method de-

scribed in Ref. [81] that is used to solve the HFB equations for finite nuclei.

Solving the HFB equations can be broken down to nested “subproblems” as defined in Ref. [81], where inside each iteration that approaches the solution of the HFB problem one has to solve (i) a linear sub-problem that determines the eigenvalues and eigenvectors of the single-particle Hamiltonian h for given potentials, (ii) a pairing sub-problem that solves the HFB matrix equation in the basis of eigenstates of h , and (iii) a non-linear sub-problem for the updates of the self-consistent-fields (SCFs) that enter the calculation of the matrices that represent h and Δ .

For INM, the linear sub-problem of diagonalising the single-particle Hamiltonian h for given potentials is analytically solved as the eigenvectors of h are known a priori to be the plane waves of Eq. (A.1), while the eigenvalues of h can be calculated from the analytical expression (B.59).

Concerning the pairing sub-problem, for given chemical potential λ_q and set of h_k and Δ_k , the numerical values of the eigenvalues and eigenvectors of the HFB matrix equation (17) are calculated from the analytical expressions constructed in Appendix A. To solve the pairing sub-problem, however, the chemical potentials λ_q of protons and neutrons have to be numerically adjusted such that ρ_p and ρ_n calculated through Eq. (B.46) combine to the targeted values of ρ and I defined through Eqs. (13) and (14). This problem can be mapped on finding the roots of two coupled non-linear equations, one for protons and another one for neutrons. In case of either symmetric or pure neutron matter, there is even just one independent chemical potential, which then can be efficiently determined with a combination of bisection and Brent’s method. For the more general case of arbitrarily asymmetric INM, the two independent chemical potentials of protons and neutrons are adjusted with Newton’s method.

In either case, $k_{\lambda,q}$ is then determined by finding the momentum that yields $h_{k_{\lambda,q}\sigma,k_{\lambda,q}\sigma} = \lambda_q$ from Eq. (B.59). Even for Skyrme EDFs at N2LO, this is a simple bi-quadratic equation that can be analytically solved.

As the integration mesh as defined in Appendix C is centred at the momentum $k_{\lambda,q}$ corresponding to the chemical potential λ_q , the integration mesh however has to be re-centred to $k_{\lambda,q}$ for each update of λ_q .

As a numerically simpler and more robust alternative, the HFB equations can also be solved at fixed $k_{\lambda,q}$ [118] (which is equivalent to fixed λ_q), in which case the integration mesh does not have to be re-centred. In such scheme, however, one has no control over the resulting values of ρ_n and ρ_p , which makes it impossible to trace the density-dependence of asymmetric matter

at a fixed arbitrary asymmetry, or to scan BECs when the chemical potential is below the potential depth in INM. Still, a scheme with fixed $k_{\lambda,q}$ offers a very robust procedure for the analysis of the BCS phase of both symmetric and neutron matter.

Compared to the treatment of finite nuclei within the two-basis method as described in Ref. [81], the canonical basis of the HFB problem for INM does not have to be explicitly constructed, as the plane-wave states simultaneously diagonalise the single-particle Hamiltonian $h_{\mathbf{k}\sigma q,\mathbf{k}'\sigma'q}$ and the density matrix $\rho_{\mathbf{k}\sigma q,\mathbf{k}'\sigma'q}$. Instead, the normal and pair densities can be directly calculated in the plane-wave basis as described in Appendix B.1 and Appendix B.2 without a basis change. With this, the HFB calculation of INM has the numerical simplicity of what for finite nuclei is usually called the HF+BCS calculation [1], but without loss of generality.

For INM, the non-linear SCF updates also become quite simple: the potentials and densities are numbers instead of spatial functions, such that there are no spatial oscillations to be attenuated when going from one iteration to the next. Still, to stabilise the iterations, the normal potentials $F^{A,B}$ and pair potentials $\tilde{F}^{A,B}$ are linearly mixed going from the iteration i to the next

$$F^{A,B(i+1)} = (1 - \beta) F^{A,B(i)} + \beta F_{|\psi}^{A,B(i+1)}, \quad (\text{D.79})$$

$$\tilde{F}^{A,B(i+1)} = (1 - \beta) \tilde{F}^{A,B(i)} + \beta \tilde{F}_{|\psi}^{A,B(i+1)}, \quad (\text{D.80})$$

where the $F^{A,B(i)}$ are the “mixed” potentials constructed at the end of iteration i that enter the HFB Hamiltonian at iteration $i + 1$, and the $F_{|\psi}^{A,B(i+1)}$ are the potentials obtained directly from the densities constructed from the solution of the HFB equations at iteration $i + 1$. The optimal value for the mixing parameter β depends on the properties of the parametrisations of the Skyrme and pair EDFs used, and also the density and asymmetry at which the calculation is performed. In some cases the HFB equations can actually be converged without such mixing, $\beta = 1$. A robust choice that worked for almost all calculations we made so far is $\beta = 0.1$.

In the limit of disappearing pairing, the code does in general not find a HF solution by itself when starting from a weakly paired solution, reason being that $k_{\lambda,q}$ continues to change by a tiny amount at each iteration. When the code detects that the $u_k v_k$ factors are significantly different from zero only for a very few integration points around $k_{\lambda,q}$, it sets the occupation numbers to those of a HF calculation for which $k_{F,q}$ and $k_{\lambda,q}$ are equal and correspond to the targeted density ρ_q through Eq. (19).

At convergence, the internal consistency between the calculation of the EDF (B.54), the calculation of the

potentials $F_q^{A,B}$ of Eqs. (B.61), (B.62), (B.63), (B.64), (B.70), and (B.72), and the elements of the matrices $h_{\mathbf{k}\sigma q; \mathbf{k}'\sigma' q}$ (B.59) and $\Delta_{\mathbf{k}\sigma q; \mathbf{k}'\sigma' q}$ (B.71) can be verified through an alternative calculation of the total energy through the expression [48]

$$\mathcal{E}_{\text{tot},sp} = \frac{1}{2}\mathcal{E}_{\text{kin}} + \frac{1}{2}\mathcal{E}_{\text{sp}} + \frac{1}{2}\mathcal{E}_{\Delta} + \mathcal{E}_{\text{re}} \quad (\text{D.81})$$

that, besides the kinetic energy \mathcal{E}_{kin} of Eq. (B.55), is composed of the weighted sum over single-particle energies

$$\mathcal{E}_{\text{sp}} = \frac{8\pi}{(2\pi)^3} \sum_q \int dk k^2 v_{k,q}^2 \varepsilon_{k,q}, \quad (\text{D.82})$$

the pairing energy obtained summing up gaps

$$\mathcal{E}_{\Delta} = -\frac{1}{2} \frac{8\pi}{(2\pi)^3} \sum_q \int dk k^2 u_{k,q} v_{k,q} f_{k,q}^2 \Delta_{k,q}, \quad (\text{D.83})$$

and the rearrangement energy from the density-dependent terms that for the EDF used here reads

$$\begin{aligned} \mathcal{E}_{\text{re}} = & \frac{\alpha}{2} \sum_{t=0,1} A_{t,e}^{(0,2)} (D_0^{1,1})^\alpha (D_t^{1,1})^2 \\ & + \frac{\sigma}{2} \sum_{q=p,n} \tilde{A}_{qq}^{(0,2)} (D_0^{1,1})^\sigma |\tilde{D}_q^{1,1}|^2. \end{aligned} \quad (\text{D.84})$$

In our implementation, for NLO and N2LO EDFs, the energy per particle calculated either directly from the EDF of Eq. (B.54) expressed through the local densities as outlined in Appendix B.3 and Appendix B.6, or as $\mathcal{E}_{\text{tot},sp}/\rho$ from Eq. (D.81) typically differs by less than 10^{-2} keV.

Appendix E: The role of spin-gradient terms

A point not addressed in the main text concerns the predictive power of the original SLy4+ULB parametrisation for the pairing properties of finite nuclei or, more specifically, if SLy4+ULB shares the predictive power of the 1T2T(X) parametrisations plus a pairing EDF adjusted to reproduce the pairing gap of SLy4+ULB in symmetric INM.

Our unexpected observation is that the data for $\Delta_n^{(5)}(Z, N)$ are significantly less well reproduced by the original SLy4+ULB parametrisation than by the the 1T2T(X) + LO^{ULB} parameter sets. This is illustrated by the bottom panels of Fig. 25, which compare results for the Sn, Yb, and Pb isotopic chains obtained with SLy4+ULB (purple line) with results obtained with the 1T2T(X) + LO^{ULB} (data taken from Fig. 16 and represented by solid lines in the same colour as there). For SLy4, the difference between calculated and experimental gaps is particularly large for the spherical Sn and Pb isotopes just below ¹³²Sn and ²⁰⁸Pb, respectively.

It turns out that this difference in performance is mainly caused by the terms in the NLO EDF that in one way or another couple two gradients with two Pauli spin matrices

$$\begin{aligned} \mathcal{E}_{\sigma\nabla}(\mathbf{r}) = & A_{t,o}^{(2,2)} \left[\mathbf{D}_t^{1,\sigma}(\mathbf{r}) \cdot \mathbf{D}_t^{(\nabla,\nabla)\sigma}(\mathbf{r}) \right. \\ & \left. - \sum_{\mu\nu} C_{t,\mu\nu}^{1,\nabla\sigma}(\mathbf{r}) C_{t,\mu\nu}^{1,\nabla\sigma}(\mathbf{r}) \right] \\ & + A_{t,o}^{(2,1)} \mathbf{D}_t^{1,\sigma}(\mathbf{r}) \cdot \Delta \mathbf{D}_t^{1,\sigma}(\mathbf{r}), \end{aligned} \quad (\text{E.85})$$

represented again in the notation of Ref. [34]. Galilean invariance of the nuclear EDF [161] requires that two out of these three terms have the same coupling constant $A_{t,o}^{(2,2)}$ with opposite sign (but none of these terms contributes to the EDF of isotropic homogeneous non-polarised INM).

For reasons of numerical and phenomenological convenience, the coupling constants of these spin-gradient terms have been explicitly set to zero during the parameter adjustment of SLy4, see [35], which is common practice for the majority of Skyrme parameter sets found in the literature [48]. By contrast, all of these terms are kept for the 1T2T(X) and also SN2LO1. The influence of these terms on binding energies and the $\Delta_n^{(5)}(Z, N)$ values of Sn, Pb, and Yb isotopes can also be deduced from Fig. 25. The dots on the lower panel represent $\Delta_n^{(5)}(Z, N)$ obtained from self-consistent calculations with modified 1T2T(X) + LO^{ULB} parametrisations for which the coupling constants of the spin-gradient terms of Eq. (E.85) are artificially set to zero as always done for SLy4.⁵ The such modified 1T2T(X) parameter sets do of course not minimise the penalty function of their parameter adjustment anymore and should therefore not be used for production calculations. With few exceptions, the modified 1T2T(X) parameter sets yield significantly larger $\Delta_n^{(5)}(Z, N)$, with the effect being much more dramatic for the Sn and Pb chains than for the deformed Yb isotopes.

Interestingly, the effect of the spin-gradient terms seems to scale with effective mass. In particular, the $\Delta_n^{(5)}(Z, N)$ obtained from the modified 1T2T(0.70) are very similar to those of SLy4 that has a near-identical effective mass. The effective-mass dependence of the spin-gradient terms can be better isolated when plotting the difference in (negative) total energy between a calculation without spin-gradient terms and a full cal-

⁵Note that a modified SLy4 parametrisation to which spin-gradient terms are added with coupling constants as dictated by the two-body Skyrme generator has a finite-size spin instability, which prohibits us from doing the analysis also the other way around.

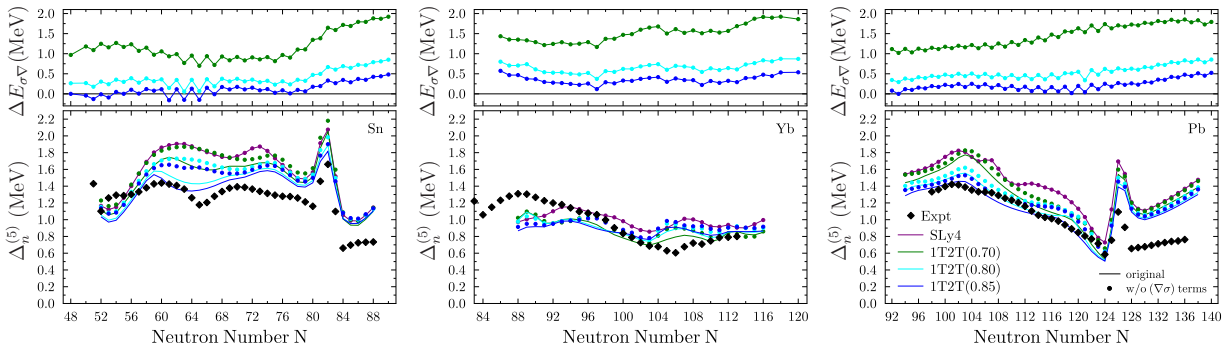


Fig. 25 The lower panels show the pairing gap $\Delta_n^{(5)}$ for the chains of Sn, Yb, and Pb, isotopes calculated with the original SLy4+ULB parameter set (purple) compared to calculations with the 1T2T(X) parameter sets combined with LO^{ULB} pairing parameters. For the 1T2T(X) results from two different sets of calculations are shown that either do (solid lines) or do not (dots) take into account the terms in the EDF that contain two gradients and two Pauli matrices (see text). The upper panel displays the difference in (negative) total ground-state energy $\Delta E = E_{w/o(\sigma\nabla)} - E_{\text{org}}$ between these two choices. Positive values indicate that the calculation without spin-gradient terms yields more binding energy.

calculation

$$\Delta E_{\sigma\nabla}(Z, N) \equiv E_{w/o(\sigma\nabla)}(Z, N) - E_{\text{org}}(Z, N), \quad (\text{E.86})$$

which is done in the upper panels on Fig. 25. The spin-gradient terms are mostly repulsive. For the 1T2T(X), the energy loss from the spin-gradient terms indeed becomes much larger with decreasing m_0^*/m . This seems to be an indirect consequence of the coupling constants of the spin-gradient terms of Eq. (E.85) depending on different combinations of the same coupling constants t_1 , x_1 , t_2 , and x_2 that determine the difference between the bare nucleon mass and the isoscalar and isovector effective masses of a NLO Skyrme EDF.

A global shift of all binding energies does not affect $\Delta_n^{(5)}(Z, N)$, though. More important for the purpose of our study is the clearly visible odd-even staggering of $\Delta E_{\sigma\nabla}(Z, N)$ that is much more pronounced for the chains of spherical Sn and Pb isotopes than for the chain of deformed Yb isotopes. The size of the odd-even staggering of $\Delta E_{\sigma\nabla}(Z, N)$ also tends to grow with decreasing effective mass, while exhibiting also a dependence on the quantum numbers of the blocked neutron.

The comparison of results from calculations with the modified and the original 1T2T(X) clearly indicates that the spin-gradient terms can bring a sizeable contribution to the odd-even staggering of total energies. For odd nuclei, the time-even $C_{t,\mu\nu}^{1,\nabla\sigma} C_{t,\mu\nu}^{1,\nabla\sigma}$ spin-current tensor terms, which are mainly determined by the overall filling of orbits [11, 14], usually take a similar size as in adjacent even-even nuclei. What is different for odd nuclei is that there is an additional contribution from the time-odd $\mathbf{D}_t^{1,\sigma} \cdot \mathbf{D}_t^{(\nabla,\nabla)\sigma}$ terms that leads to spin-dependent effective masses. These two types of terms usually contribute with opposite sign to the total energy, and in some cases the time-odd contribution reaches half the size of its time-even partner terms.

Combined, these terms generate a contribution to the odd-even staggering of masses that has nothing to do with pairing correlations. For the 1T2T(X) the combined contribution of these two terms is repulsive – as is the case for the majority of Skyrme parametrisations that take them into account [11, 14] – leading to a smaller energy loss for odd than for even isotopes.

In addition, for most Skyrme NLO EDFs the time-odd $\mathbf{D}_t^{1,\sigma} \cdot \Delta \mathbf{D}_t^\sigma$ terms that also only contribute to odd-mass nuclei are in general attractive and, depending on quantum numbers of the blocked quasiparticle, can be as large as a few 100 keV, which then further increases the binding energy of odd isotopes.

The presence of the spin-gradient terms of course affects the total size of the other time-odd spin terms though self-consistent polarisation effects when minimising the total energy, as it does more generally affect the size of all other terms, but the overall net effect is that the contribution of the spin-gradient terms of Eq. (E.85) in most cases reduces the difference in binding energy between odd nuclei and the adjacent even-even ones.

Through Eq. (24), the spin-gradient terms then ultimately lead to smaller $\Delta_n^{(5)}(Z, N)$ for *all* isotopes. Because of the interdependence of the coupling constants in the Skyrme EDF, for the 1T2T(X) the overall size of the odd-even effect from spin-gradient terms depends on effective mass. For the SLy4 parametrisation that by construction is to be used without spin-gradient terms, one consequently finds larger odd-even staggering of total energies and systematically larger $\Delta_n^{(5)}(Z, N)$ than what is found when using the (original) 1T2T(X) parameter sets.

The absence of spin-gradient terms actually introduces a violation of the Pauli principle by the Skyrme EDF (in addition to the one already present because of

density-dependent terms and the use of different EDFs for the particle-hole and particle-particle channels) which is accompanied by spurious self-interactions [44–46] whose net effect on binding energies might be on an energy scale that is relevant for the phenomena discussed here [166]. Because of the difficulty to isolate the net contribution from self-interactions to the total energy, however, it cannot be easily judged if the difference in performance of SLy4 and the 1T2T(X) for $\Delta_n^{(5)}(Z, N)$ is mainly related to relevant physics brought by spin-gradient terms to the 1T2T(X) or by spurious self-interactions contained in SLy4.

The quantum-number dependence of the contribution of the spin-gradient terms to $\Delta_n^{(5)}(Z, N)$ could also be partially responsible for deviations between theory and experiment when the ground-state configuration is incorrectly described, and the effective-mass dependence of this contribution found for the 1T2T(X) could be partially responsible for the systematic spread between the predictions from the 1T2T(X) for $\Delta_n^{(5)}(Z, N)$ as found for certain nuclei.

The difference in performance between SLy4 and the 1T2T(X) also raises the question to which extent the very satisfying performance of the LO^{ULB} pairing parameters that are adjusted to reproduce the gaps from SLy4+ULB pairing in INM might be fortuitous.

It is to be noted that, compared to the NLO EDF, the N2LO EDF of SN2LO1 contains several additional spin-gradient terms [34] with independent coupling constants, and there are also additional time-even terms contributing to m_0^*/m , which complicates the situation and might lead to different correlations between the terms in the EDF than what is found for the 1T2T(X).

References

1. P. Ring and P. Schuck, *The Nuclear Many Body Problem* (Springer, Berlin, 1980).
2. D. Brink and R. A. Broglia, *Nuclear Superfluidity: Pairing in Finite Systems* (Cambridge University Press, Cambridge, UK, 2005).
3. R. A. Broglia and V. V. Zelevinski (Edts.), *Fifty Years of Nuclear BCS* (World Scientific Pub. Co., Singapore, 2013).
4. D. J. Dean and M. Hjorth-Jensen, Pairing in nuclear systems: from neutron stars to finite nuclei, *Rev. Mod. Phys.* **75**, 607 (2003).
5. N. Chamel and P. Haensel, Physics of neutron star crusts, *Living Rev. Relativ.* **11**, 10 (2008).
6. M. Bender, P.-H. Heenen, and P.-G. Reinhard, Self-consistent mean-field models for nuclear structure, *Rev. Mod. Phys.* **75**, 121 (2003).
7. N. Schunck (Ed.), *Energy Density Functional Methods for Atomic Nuclei* (IOP, Bristol 2019).
8. A. S. Jensen and A. Miranda, The Skyrme-plus-pairing effective interaction and the global neutron-excess dependence of the pairing gap, *Nucl. Phys. A* **449**, 331 (1986).
9. Ph. Da Costa, K. Bennaceur, J. Meyer, W. Ryssens, and M. Bender, Impact of choices for center-of-mass correction energy on the surface energy of Skyrme energy density functionals, *Phys. Rev. C* **109**, 034316 (2024).
10. L. Bonneau, P. Quentin, and P. Möller, Global microscopic calculations of ground-state spins and parities for odd-mass nuclei, *Phys. Rev. C* **76**, 024320 (2007).
11. T. Lesinski, M. Bender, K. Bennaceur, T. Duguet, and J. Meyer, Tensor part of the Skyrme energy density functional: Spherical nuclei, *Phys. Rev. C* **76**, 014312 (2007).
12. D. Tarpanov, J. Dobaczewski, J. Toivanen, and B. G. Carlsson, Spectroscopic properties of nuclear Skyrme energy density functionals, *Phys. Rev. Lett.* **113**, 252501 (2014).
13. J. Dobaczewski, A. V. Afanasjev, M. Bender, L. M. Robledo, and Yue Shi, Properties of nuclei in the nobelium region studied within the covariant, Skyrme, and Gogny energy density functionals, *Nucl. Phys. A* **944**, 388 (2015).
14. M. Bender, K. Bennaceur, T. Duguet, P.-H. Heenen, T. Lesinski, and J. Meyer, Tensor part of the Skyrme energy density functional. II: Deformation properties of magic and semi-magic nuclei, *Phys. Rev. C* **80**, 064302 (2009).
15. T. Duguet and T. Lesinski, Non-empirical pairing functional, *Eur. Phys. J. ST* **156**, 207 (2008).
16. K. Hebeler, T. Duguet, T. Lesinski, and A. Schwenk, Non-empirical pairing energy functional in nuclear matter and finite nuclei, *Phys. Rev. C* **80**, 044321 (2009).
17. T. Lesinski, T. Duguet, K. Bennaceur, and J. Meyer, Non-empirical pairing energy density functional. First order in the nuclear plus Coulomb two-body interaction, *Eur. Phys. J. A* **40**, 121 (2009).
18. G. F. Bertsch and H. Esbensen, Pair correlations near the neutron drip line, *Ann. Phys. (NY)* **209**, 327 (1991).
19. H. Esbensen, G. F. Bertsch, and K. Hencken, Application of contact interactions to Borromean halos, *Phys. Rev. C* **56**, 3054 (1997).
20. M. Matsuo, Spatial structure of neutron Cooper pair in low density uniform matter, *Phys. Rev. C* **73**, 044309 (2006).
21. E. Garrido, P. Sarriguren, E. Moya de Guerra, and P. Schuck, Effective density-dependent pairing forces in the $T = 1$ and $T = 0$ channels, *Phys. Rev. C* **60**, 064312 (1999).
22. T. Duguet, Bare vs effective pairing forces: A microscopic finite-range interaction for Hartree-Fock-Bogolyubov calculations in coordinate space, *Phys. Rev. C* **69**, 054317 (2004).
23. N. Chamel, Effective contact pairing forces from realistic calculations in infinite homogeneous nuclear matter, *Phys. Rev. C* **82**, 014313 (2010).
24. C. Shen, U. Lombardo, and P. Schuck, Screening of nuclear pairing in nuclear and neutron matter, *Phys. Rev. C* **71**, 054301 (2005).
25. S. Ramanan and M. Urban, Screening and antiscreening of the pairing interaction in low-density neutron matter, *Phys. Rev. C* **98**, 024314 (2018).
26. M. Urban and S. Ramanan, Neutron pairing with medium polarization beyond the Landau approximation, *Phys. Rev. C* **101**, 035803 (2020).
27. S. Ramanan and M. Urban, Pairing in pure neutron matter, *Eur. Phys. J. ST* **230**, 567 (2021).
28. M. Baldo, U. Lombardo, E. E. Saperstein, M. V. Zverev, On the surface nature of the nuclear pairing, *Phys. Rep.* **391**, 261 (2004).

29. A. Pastore, F. Barranco, R. A. Broglia, and E. Vigezzi, Microscopic calculation and local approximation of the spatial dependence of the pairing field with bare and induced interactions, *Phys. Rev. C* **78**, 024315 (2008).
30. M. Baldo, U. Lombardo, S. S. Pankratov, and E. E. Saperstein, Microscopic evaluation of the pairing gap, *J. Phys. G: Nucl. Part. Phys.* **37**, 064016 (2010).
31. A. Idini, F. Barranco, and E. Vigezzi, Quasiparticle renormalization and pairing correlations in spherical superfluid nuclei, *Phys. Rev. C* **85**, 014331 (2012).
32. A. Idini, G. Potel, F. Barranco, E. Vigezzi, and R. A. Broglia, Dual origin of pairing in nuclei, *Phys. Atom. Nuclei* **79**, 807 (2016).
33. E. Litvinova and P. Schuck, Many-body correlations in nuclear superfluidity, *Phys. Rev. C* **102**, 034310 (2020).
34. W. Ryssens and M. Bender, Skyrme pseudopotentials at next-to-next-to-leading order. Construction of local densities and first symmetry-breaking calculations, *Phys. Rev. C* **104**, 044308 (2021).
35. E. Chabanat, P. Bonche, P. Haensel, J. Meyer, and R. Schaeffer, A Skyrme parametrization from subnuclear to neutron star densities Part II. Nuclei far from stabilities, *Nucl. Phys. A* **635**, 231 (1998), *Nucl. Phys. A* **643**, 441(E) (1998).
36. P. Becker, D. Davesne, J. Meyer, J. Navarro, and A. Pastore, Solution of Hartree-Fock-Bogoliubov equations and fitting procedure using the N2LO Skyrme pseudopotential in spherical symmetry, *Phys. Rev. C* **96**, 044330 (2017).
37. C. Rigollet, P. Bonche, H. Flocard, and P.-H. Heenen, Microscopic study of the properties of identical bands in the $A = 150$ mass region, *Phys. Rev. C* **59**, 3120 (1999).
38. T. Duguet, P. Bonche, P.-H. Heenen, and J. Meyer, Pairing correlations. II. Microscopic analysis of odd-even mass staggering in nuclei, *Phys. Rev. C* **65**, 014311 (2001).
39. T. Duguet, P. Bonche, and P.-H. Heenen, Rotational properties of $^{252,253,254}\text{No}$. Influence of pairing correlations, *Nucl. Phys. A* **679**, 427 (2001).
40. V. Hellemans, P.-H. Heenen, and M. Bender, Tensor part of the Skyrme energy density functional. III. Time-odd terms at high spin, *Phys. Rev. C* **85**, 014326 (2012).
41. V. Hellemans, P.-H. Heenen and M. Bender, Finite-size instabilities in nuclear energy density functionals, Proceedings of the International Conference on "Nuclear Structure and Dynamics II", held at Opatija, Croatia, July 9-13 2012. Tamara Nikšić, Matko Milin, Dario Vretenar, Suzana Szilner [edts.] *AIP Conf. Proc.* **1491**, 242 (2012).
42. A. Pastore, D. Davesne, and J. Navarro, Linear response of homogeneous nuclear matter with energy density functionals, *Phys. Rep.* **563**, 1 (2015).
43. A. Pastore, D. Davesne, K. Bennaceur, J. Meyer, and V. Hellemans, Fitting Skyrme functionals using linear response theory, Proceedings of the 19th Nuclear Physics Workshop "Maria and Pierre Curie", held at Kazimierz Dolny, Poland, September 26 - 30, 2012. A. Baran, K. Pomorski, J. Bartel and M. Goźdz [edts.] *Phys. Scr. T* **154**, 014014 (2013).
44. S. Stringari and D. M. Brink, Constraints on effective interactions imposed by antisymmetry and charge independence, *Nucl. Phys. A* **304**, 307 (1978).
45. D. Lacroix, T. Duguet, and M. Bender, Configuration mixing within the energy density functional formalism: removing spurious contributions from non-diagonal energy kernels, *Phys. Rev. C* **79**, 044318 (2009).
46. M. Bender, T. Duguet, and D. Lacroix, Particle-number restoration within the energy density functional formalism, *Phys. Rev. C* **79**, 044319 (2009).
47. M. Bender, N. Schunck, J. P. Ebran, and T. Duguet, Single-Reference and Multi-Reference Formulation, Chapter 3 of *Energy Density Functional Methods for Atomic Nuclei*, edited by N. Schunck (IOP, Bristol 2019), pp 3-1 to 3-78.
48. W. Ryssens, V. Hellemans, M. Bender, and P.-H. Heenen, Solution of the Skyrme HF+BCS equation on a 3D mesh. II. A new version of the Ev8 code, *Comp. Phys. Comm.* **187**, 175 (2015). Corrigendum *Comp. Phys. Comm.* **190**, 231 (2015). Unfortunately, the corrections of the expressions as given in the corrigendum still contain a typographical error: the formula for the second derivative has a superfluous factor of two when $i \neq j$, see Ref. [88].
49. I. Ragnarsson and S. G. Nilsson, *Shapes and Shells in Nuclear Structure* (Cambridge University Press, 1995).
50. M. Bender, K. Rutz, P.-G. Reinhard, and J. A. Maruhn, Pairing gaps from nuclear mean-field models, *Eur. Phys. J. A* **8**, 59 (2000).
51. G. F. Bertsch, C. A. Bertulani, W. Nazarewicz, N. Schunck, and M. V. Stoitsov, Odd-even mass differences from self-consistent mean field theory, *Phys. Rev. C* **79**, 034306 (2009).
52. P. Klüpfel, P.-G. Reinhard, T. J. Bürvenich, and J. A. Maruhn, Variations on a theme by Skyrme: A systematic study of adjustments of model parameters, *Phys. Rev. C* **79**, 034310 (2009).
53. M. Kortelainen, J. McDonnell, W. Nazarewicz, E. Olsen, P.-G. Reinhard, J. Sarich, N. Schunck, S. M. Wild, D. Davesne, J. Erler, and A. Pastore, Nuclear energy density optimization: Shell structure, *Phys. Rev. C* **89**, 054314 (2014).
54. J. Margueron, H. Sagawa, and K. Hagino, Effective pairing interactions with isospin density dependence, *Phys. Rev. C* **77**, 054309 (2008).
55. C. A. Bertulani, H. F. Lü, and H. Sagawa, Odd-even mass difference and isospin dependent pairing interaction, *Phys. Rev. C* **80**, 027303 (2009).
56. M. Yamagami, J. Margueron, H. Sagawa, and K. Hagino, Isoscalar and isovector density dependence of the pairing functional determined from global fitting, *Phys. Rev. C* **86**, 034333 (2012).
57. Zhen Zhang and Lie-Wen Chen, Pairing effects on neutron matter equation of state and symmetry energy at subsaturation densities, *Phys. Rev. C* **100**, 044301 (2019).
58. S. S. Zhang, L. G. Cao, U. Lombardo, E. G. Zhao, and S. G. Zhou, Isospin-dependent pairing interaction from nuclear matter calculations, *Phys. Rev. C* **81**, 044313 (2010).
59. S. Goriely, N. Chamel, and J. M. Pearson, Further explorations of Skyrme-Hartree-Fock-Bogoliubov mass formulas. XVI. Inclusion of self-energy effects in pairing, *Phys. Rev. C* **93**, 034337 (2016).
60. G. Grams, W. Ryssens, G. Scamps, S. Goriely, and N. Chamel, Skyrme-Hartree-Fock-Bogoliubov mass models on a 3D mesh: III. From atomic nuclei to neutron stars, *Eur. Phys. J. A* **59**, 270 (2023).
61. G. Grams, N. N. Shchepochin, A. Sánchez-Fernández, W. Ryssens, N. Chamel, and S. Goriely, Skyrme-Hartree-Fock-Bogoliubov mass models on a 3D mesh: IV. Improved description of the isospin dependence of pairing, *Eur. Phys. J. A* **61**, 35 (2025).

62. G. Grams, W. Ryssens, A. Sánchez-Fernández, N. N. Shchepochin, L. González-Miret Zaragoza, P. Demol, N. Chamel, S. Goriely, and M. Bender, Skyrme-Hartree-Fock-Bogoliubov mass models on a 3D mesh: V. The N2LO extension of the Skyrme EDF, preprint arXiv:2601.05968 [nucl-th].
63. S. A. Changizi and C. Qi, Density dependence of the pairing interaction and pairing correlation in unstable nuclei, *Phys. Rev. C* **91**, 024305 (2015).
64. E. Khan, M. Grasso, and J. Margueron, Constraining the nuclear pairing gap with pairing vibrations, *Phys. Rev. C* **80**, 044328 (2009).
65. E. Plumbi, M. Grasso, D. Beaumel, E. Khan, J. Margueron, and J. van de Wiele, Probing the pairing interaction through two-neutron transfer reactions, *Phys. Rev. C* **83**, 034613 (2011).
66. D. Gambacurta and D. Lacroix, Description of two-particle transfer in superfluid systems, *Phys. Rev. C* **86**, 064320 (2012).
67. H. Shimoyama and M. Matsuo, Di-neutron correlation in monopole two-neutron transfer modes in the Sn isotope chain, *Phys. Rev. C* **88**, 054308 (2013).
68. S. A. Fayans, S. V. Tolokonnikov, E. L. Trykov, and D. Zawischa, Isotope shifts within the energy-density functional approach with density dependent pairing, *Phys. Lett. B* **338**, 1 (1994).
69. S. A. Fayans and D. Zawischa, Towards a better parametrization of the nuclear pairing force: density dependence with gradient term, *Phys. Lett. B* **383**, 19 (1996).
70. S. A. Fayans, S. V. Tolokonnikov, E. L. Trykov, and D. Zawischa, Nuclear isotope shifts within the local energy-density functional approach, *Nucl. Phys. A* **676**, 49 (2000).
71. S. Fayans and D. Zawischa, Local energy-density functional approach to many-body nuclear systems with s -wave pairing, *Int. J. Mod. Phys. B* **15**, 1684 (2001).
72. E. E. Saperstein and S. V. Tolokonnikov, Self-consistent theory of Finite Fermi Systems and radii of nuclei, *Phys. At. Nucl.* **74**, 1277 (2011).
73. I. N. Borzov and S. V. Tolokonnikov, Self-Consistent study of nuclear charge radii in Ar-Ti region, *Phys. At. Nucl.* **85**, 222 (2022).
74. P.-G. Reinhard and W. Nazarewicz, Toward a global description of nuclear charge radii: Exploring the Fayans energy density functional, *Phys. Rev. C* **95**, 064328 (2017).
75. P.-G. Reinhard, J. O’Neal, S. M. Wild, and W. Nazarewicz, Extended Fayans energy density functional: optimization and analysis, *J. Phys. G: Nucl. Part. Phys.* **51**, 105101 (2024).
76. A. Bulgac and Y. Yu, Renormalization of the Hartree-Fock-Bogoliubov equations in the case of a zero range pairing interaction, *Phys. Rev. Lett.* **88**, 042504 (2002).
77. T. Duguet, K. Bennaceur, and P. Bonche, Pairing schemes for HFB calculations of nuclei, Proceedings of the Workshop on “New developments in Nuclear Self-Consistent Mean-Field Theories”, Yukawa Institute for Theoretical Physics, Kyoto, Japan, May 30 - June 1, 2005, arXiv:nucl-th/0508054.
78. P. J. Borycki, J. Dobaczewski, W. Nazarewicz, and M. V. Stoitsov, Pairing renormalization and regularization within the local density approximation, *Phys. Rev. C* **73**, 044319 (2006).
79. P. Bonche, H. Flocard, P.-H. Heenen, S. J. Krieger, and M. S. Weiss, Self-consistent study of triaxial deformations: Application to the isotopes of Kr, Sr, Zr and Mo, *Nucl. Phys. A* **443**, 39 (1985).
80. S. J. Krieger, P. Bonche, H. Flocard, P. Quentin, and M. S. Weiss, An improved pairing interaction for mean field calculations using Skyrme potentials, *Nucl. Phys. A* **517**, 275 (1990).
81. W. Ryssens, M. Bender, and P.-H. Heenen, Iterative approaches to the self-consistent nuclear energy density functional problem. Heavy ball dynamics and potential preconditioning, *Eur. Phys. J. A* **55**, 93 (2019).
82. R. Jodon, M. Bender, K. Bennaceur, and J. Meyer, Constraining the surface properties of effective Skyrme interactions, *Phys. Rev. C* **94**, 024335 (2016).
83. J. Erler, P. Klüpfel, and P.-G. Reinhard, A stabilized pairing functional, *Eur. Phys. J. A* **37**, 81 (2008). Note that the cutoff factor f_k used there corresponds to the square f_k^2 of the cutoff factor as used here.
84. J. Sauvage-Letessier, P. Quentin, and H. Flocard, Deformation properties of osmium, platinum, mercury isotopes from self-consistent calculations: Influence of the pairing treatment, *Nucl. Phys. A* **370**, 231 (1981).
85. J. Dobaczewski, H. Flocard, and J. Treiner, Hartree-Fock-Bogolyubov description of nuclei near the neutron-drip line, *Nucl. Phys. A* **422**, 103 (1984).
86. W. Ryssens, Symmetry breaking in nuclear mean-field models, Ph.D. thesis, Université Libre de Bruxelles, (2016).
87. W. Ryssens, M. Bender, and P.-H. Heenen, Numerical Code for 3d cartesian coordinate space HFB calculations with Skyrme EDFs (unpublished).
88. W. Ryssens, P.-H. Heenen, and M. Bender, Numerical accuracy of mean-field calculations in coordinate space, *Phys. Rev. C* **92**, 064318 (2015).
89. National Nuclear Data Center, information extracted from the NuDat database, <https://www.nndc.bnl.gov/nudat/>
90. From ENSDF database as of October 2024. Version available at <http://www.nndc.bnl.gov/ensarchivals/>
91. D. J. Rowe, *Nuclear Collective Motion – Models and Theory* (Methuen, London, 1970).
92. N. Schunck, J. Dobaczewski, J. McDonnell, J. Moré, W. Nazarewicz, J. Sarich, and M. V. Stoitsov, One-quasiparticle states in the nuclear energy density functional theory, *Phys. Rev. C* **81**, 024316 (2010).
93. M. Bender, Numerical code for 1d spherical coordinate space HFB calculations with Skyrme EDFs (unpublished).
94. E. M. Henley and L. Wilets, Energy gap in nuclear matter. I. Extended theory, *Phys. Rev.* **133**, B1118 (1964).
95. R. Kennedy, L. Wilets, and E. M. Henley, Energy gap in nuclear matter. II. BCS theory, *Phys. Rev.* **133**, B1131 (1964).
96. R. C. Kennedy, Pairing correlations in nuclear matter: A self-consistent calculation, *Nucl. Phys. A* **118**, 189 (1968).
97. M. Baldo, J. Cugnon, A. Lejeune, and U. Lombardo, Superfluidity in neutron matter and nuclear matter with realistic interactions, *Nucl. Phys. A* **515**, 409 (1990).
98. J. M. C. Chen, J. W. Clark, R. D. Davé, and V. V. Khodel, Pairing gaps in nucleonic superfluids, *Nucl. Phys. A* **555**, 59 (1993).
99. V. A. Khodel, V. V. Khodel, and J. W. Clark, Solution of the gap equation in neutron matter, *Nucl. Phys. A* **598**, 390 (1996).
100. Ø. Elgarøy and M. Hjorth-Jensen, Nucleon-nucleon phase shifts and pairing in neutron matter and nuclear matter, *Phys. Rev. C* **57**, 1174 (1998).

101. P. Yin, X. L. Shang, J. N. Hu, J. Y. Fu, E. Epelbaum, and W. Zuo, Pairing properties of semilocal coordinate- and momentum-space regularized chiral interactions, *Phys. Rev. C* **108**, 034002 (2023).
102. K. Hebeler and A. Schwenk, Chiral three-nucleon forces and neutron matter, *Phys. Rev. C* **82**, 014314 (2010).
103. L. G. Cao, U. Lombardo, and P. Schuck, Screening effects in superfluid nuclear and neutron matter within Brueckner theory, *Phys. Rev. C* **74**, 064301 (2006).
104. A. Rios, A. Polls, W. H. Dickhoff, Pairing and short-range correlations in nuclear systems, *J. Low Temp. Phys.* **189**, 234 (2017).
105. A. Sedrakian and J. W. Clark, Superfluidity in nuclear systems and neutron stars, *Eur. Phys. J. A* **55**, 167 (2019).
106. S. Gandolfi, A. Yu. Illarionov, F. Pederiva, K. E. Schmidt, and S. Fantoni, Equation of state of superfluid neutron matter and the calculation of the 1S_0 pairing gap, *Phys. Rev. Lett.* **101**, 132501 (2008).
107. S. Gandolfi, A. Yu. Illarionov, F. Pederiva, K. E. Schmidt, and S. Fantoni, Equation of state of low-density neutron matter, and the 1S_0 pairing gap, *Phys. Rev. C* **80**, 045802 (2009).
108. S. Gandolfi, G. Palkanoglou, J. Carlson, A. Gezerlis, and K. E. Schmidt, The 1S_0 pairing gap in neutron matter, *Condensed Matter* **7**, 19 (2022).
109. H. Kucharek, P. Ring, P. Schuck, R. Bengtsson, and M. Girod, Pairing properties of nuclear matter from the Gogny force, *Phys. Lett. B* **216**, 249 (1989).
110. D. Davesne, J. Navarro, A. Pastore, and Y. Lallouet, Isovector properties of effective finite-range nuclear interactions, *Eur. Phys. J. A* **61**, 28 (2025).
111. S. Takahara, N. Onishi, and N. Tajima, Pairing correlation in nuclear matter from Skyrme force, *Phys. Lett. B* **331**, 261 (1994).
112. R. Aguirre, Nuclear superfluidity in isospin asymmetric matter within the Skyrme model, *Phys. Rev. C* **85**, 064314 (2012).
113. H. Kucharek and P. Ring, Relativistic field theory of superfluidity in nuclei, *Z. Phys. A* **339**, 23 (1991).
114. M. Serra, A. Rummel, and P. Ring, Relativistic theory of pairing in infinite nuclear matter, *Phys. Rev. C* **65**, 014304 (2001).
115. J. P. Blaizot and G. Ripka, *Quantum Theory of Finite Systems* (MIT Press, Cambridge Massachusetts 1986).
116. E. K. U. Gross, E. Runge, and O. Heinonen, *Many-Particle Theory* (Adam Hilger, Bristol, Philadelphia and New York 1991).
117. J. A. Maruhn, P.-G. Reinhard, and E. Suraud, *Simple Models of Many-Fermion Systems* (Springer-Verlag, Berlin, Heidelberg, 2010).
118. V. Guillon, Équation du gap dans la matière infinie, Masters thesis, Université Claude Bernard - Lyon 1 (2024).
119. G. C. Strinati, P. Pieri, G. Röpke, P. Schuck, and M. Urban, The BCS–BEC crossover: From ultra-cold Fermi gases to nuclear systems, *Phys. Rep.* **738**, 1 (2018).
120. T. Lesinski, K. Bennaceur, T. Duguet, and J. Meyer, Isovector splitting of nucleon effective masses, ab initio benchmarks and extended stability criteria for Skyrme energy functionals, *Phys. Rev. C* **74**, 044315 (2006).
121. J. Margueron, E. Khan, G. Colò, K. Hagino, and H. Sagawa, Effect of pairing on the symmetry energy and the incompressibility, *Eur. Phys. J. A* **50**, 18 (2014).
122. C. Ducoin, Ph. Chomaz, and F. Gulminelli, Isospin-dependent clusterization of neutron-star matter *Nucl. Phys. A* **789**, 403 (2007).
123. N. Sandulescu, P. Schuck, and X. Viñas, Nuclear pairing: Surface or bulk? *Phys. Rev. C* **71**, 054303 (2005).
124. S. V. Tolokonnikov, S. Kamerdzhev, D. Voytenkov, S. Krewald, and E. E. Saperstein, Effects of density dependence of the effective pairing interaction on the first 2^+ excitations and quadrupole moments of odd nuclei, *Phys. Rev. C* **84**, 064324 (2011).
125. O. A. Rubtsova, V. I. Kukulín, V. N. Pomerantsev, and H. Muether, In-medium bound states and pairing gap, *Phys. Rev. C* **96**, 034327 (2017).
126. U. Lombardo, P. Nozieres, P. Schuck, H. J. Schulze, and A. Sedrakian, Transition from BCS pairing to Bose-Einstein condensation in low density asymmetric nuclear matter, *Phys. Rev. C* **64**, 064314 (2001).
127. T. T. Sun, B. Y. Sun, and J. Meng, BCS-BEC crossover in nuclear matter with the relativistic Hartree-Bogoliubov theory, *Phys. Rev. C* **86**, 014305 (2012).
128. J. Margueron, H. Sagawa, and K. Hagino, BCS-BEC crossover of neutron pairs in symmetric and asymmetric nuclear matter, *Phys. Rev. C* **76**, 064316 (2007).
129. V. Rotival, K. Bennaceur, and T. Duguet, Halo phenomenon in finite many-Fermion systems. Atom-positron complexes and large-scale study of atomic nuclei, *Phys. Rev. C* **79**, 054309 (2009).
130. V. Rotival, Fonctionnelles d'énergie non-empiriques pour la structure nucléaire, Thesis, Université Denis Diderot - Paris VII (2008).
131. J. Dobaczewski, W. Nazarewicz, T. R. Werner, J. F. Berger, C. R. Chinn, and J. Dechargé, Mean-field description of ground-state properties of drip-line nuclei: Pairing and continuum effects, *Phys. Rev. C* **53**, 2809 (1996).
132. W. Ryssens, M. Bender, K. Bennaceur, P.-H. Heenen, and J. Meyer, The impact of the surface energy coefficient on the deformation properties of atomic nuclei as predicted by Skyrme energy density functionals, *Phys. Rev. C* **99**, 044315 (2019).
133. J. F. Berger, M. Girod, and D. Gogny, Time-dependent quantum collective dynamics applied to nuclear fission, *Comp. Phys. Comm.* **63**, 365 (1991).
134. L. M. Robledo, R. Bernard, and G. F. Bertsch, Pairing gaps in the Hartree-Fock-Bogoliubov theory with the Gogny D1S interaction, *Phys. Rev. C* **86**, 064313 (2012).
135. K. Bennaceur, J. Dobaczewski, T. Haverinen, and M. Kortelainen, Properties of spherical and deformed nuclei using regularized pseudopotentials in nuclear DFT, *J. Phys. G: Nucl. Part. Phys.* **47**, 105101 (2020).
136. A. S. Jensen, P. G. Hansen, and B. Jonson, New mass relations and two- and four-nucleon correlations, *Nucl. Phys. A* **431**, 393 (1984).
137. D. G. Madland and J. R. Nix, New model of the average neutron and proton pairing gaps, *Nucl. Phys. A* **476**, 1 (1988).
138. M. Bender, G. F. Bertsch, and P.-H. Heenen, Systematics of quadrupolar correlation energies, *Phys. Rev. Lett.* **94**, 102503 (2005).
139. M. Bender, G. F. Bertsch, and P.-H. Heenen, Global study of quadrupole correlation effects, *Phys. Rev. C* **73**, 034322 (2006).
140. M. Bender, G. F. Bertsch, and P.-H. Heenen, Collectivity-induced quenching of signatures for shell closures, *Phys. Rev. C* **78**, 054312 (2008).
141. J. P. Delaroche, M. Girod, J. Libert, H. Goutte, S. Hilaire, S. Péru, N. Pillet, and G. F. Bertsch, Structure of even-even nuclei using a mapped collective Hamiltonian and the D1S Gogny interaction, *Phys. Rev. C* **81**, 014303 (2010).

142. X. Sun, J. Dobaczewski, M. Kortelainen, J. Sadhukhan, A. Sánchez-Fernández, and H. Wibowo, Moments of inertia of rare-earth nuclei and the nuclear time-odd mean fields within exact solutions of the adiabatic theory, *Phys. Lett. B* **868**, 139685 (2025).
143. W. Bertozzi, J. Friar, J. Heisenberg, and J. W. Negele, Contributions of neutrons to elastic electron scattering from nuclei, *Phys. Lett. B* **41**, 408 (1972).
144. J. Friar and J. W. Negele, Theoretical and experimental determination of nuclear charge distributions, *Advances in Nuclear Physics* **8**, 219 (1975).
145. P.-G. Reinhard and W. Nazarewicz, Nuclear charge densities in spherical and deformed nuclei: Toward precise calculations of charge radii, *Phys. Rev. C* **103**, 054310 (2021); *Phys. Rev. C* **107**, 069901(E) (2023).
146. M. Bender (in preparation).
147. F. P. Gustafsson, L. V. Rodríguez, R. F. Garcia Ruiz, T. Miyagi, S. W. Bai, D. L. Balabanski, C. L. Binnersley, M. L. Bissell, K. Blaum, B. Cheal, T. E. Cocolios, G. J. Farooq-Smith, K. T. Flanagan, S. Franchoo, A. Galindo-Uribarri, G. Georgiev, W. Gins, C. Gorges, R. P. de Groote, H. Heylen, J. D. Holt, A. Kanellakopoulos, J. Kartheim, S. Kaufmann, Á. Koszorús, K. König, V. Lagaki, S. Lechner, B. Maass, S. Malbrunot-Ettenauer, W. Nazarewicz, R. Neugart, G. Neyens, W. Nörtershäuser, T. Otsuka, P.-G. Reinhard, N. Rondelez, E. Romero-Romero, C. M. Ricketts, S. Sailer, R. Sánchez, S. Schmidt, A. Schwenk, S. R. Stroberg, N. Shimizu, Y. Tsunoda, A. R. Vernon, L. Wehner, S. G. Wilkins, C. Wraith, L. Xie, Z. Y. Xu, X. F. Yang, and D. T. Yordanov, Charge radii measurements of exotic tin isotopes in the proximity of $N = 50$ and $N = 82$, preprint arXiv:2504.17060v2 [nucl-ex].
148. E. Takacs, H. Staiger, S. A. Blundell, N. Kimura, H. A. Sakaue, R. F. Garcia Ruiz, W. Nazarewicz, P.-G. Reinhard, C. A. Faiyaz, C. Suzuki, Dipti, I. Angeli, Y. Ralchenko, I. Murakami, D. Kato, Y. Nagai, R. Takaoka, Y. Miya, and N. Nakamura, Puzzling isotonic odd-even staggering of charge radii in deformed rare earth nuclei, preprint arXiv:2511.19395v2 [physics.atom-ph].
149. M. Anselment, W. Faubel, S. Göring, A. Hanser, G. Meisel, H. Rebel, and G. Schatz, The odd-even staggering of the nuclear charge radii of Pb isotopes, *Nucl. Phys. A* **451**, 471 (1986).
150. H. De Witte, A. N. Andreyev, N. Barré, M. Bender, T. E. Cocolios, S. Dean, D. Fedorov, V. N. Fedoseyev, L. M. Fraille, S. Franchoo, V. Hellemans, P.-H. Heenen, K. Heyde, G. Huber, M. Huysse, H. Jeppesen, Köster, P. Kunz, S. R. Leshner, B. A. Marsh, I. Mukha, B. Roussière, J. Sauvage, M. Seliverstov, I. Stefanescu, E. Tengborn, K. Van de Vel, J. de Walle, P. Van Duppen, and Yu. Volkov, Nuclear charge radii of neutron deficient lead isotopes beyond $N = 104$ mid shell investigated by in-source laser spectroscopy, *Phys. Rev. Lett.* **98**, 112502, (2007)
151. L. Renth, Collinear laser spectroscopy of magic lead and mid-shell palladium isotopes, Dissertation, Technische Universität Darmstadt (2024).
152. I. Angeli and K. P. Marinova, Table of experimental nuclear ground state charge radii: An update, *At. Data Nucl. Data Tables* **99**, 69 (2013).
153. K. T. Flanagan, J. Billowes, P. Campbell, B. Cheal, G. D. Dracoulis, D. H. Forest, M. D. Gardner, J. Huikari, A. Jokinen, B. A. Marsh, R. Moore, A. Nieminen, H. Penttilä, H. L. Thayer, G. Tungate, and J. Äystö, Nuclear moments, charge radii and spins of the ground and isomeric states in ^{175}Yb and ^{177}Yb , *J. Phys. G* **39**, 125101 (2012).
154. T. Li, Y. Luo, and N Wang, Compilation of recent nuclear ground state charge radius measurements and tests for models, *At. Data Nucl. Data Tables* **140**, 101440 (2021).
155. D. T. Yordanov, L. V. Rodríguez, D. L. Balabanski, J. Bieroń, M. L. Bissell, K. Blaum, B. Cheal, J. Ekman, G. Gaigalas, R. F. Garcia Ruiz, G. Georgiev, W. Gins, M. R. Godefroid, C. Gorges, Z. Harman, H. Heylen, P. Jönsson, A. Kanellakopoulos, S. Kaufmann, C. H. Keitel, V. Lagaki, S. Lechner, B. Maaß, S. Malbrunot-Ettenauer, W. Nazarewicz, R. Neugart, G. Neyens, W. Nörtershäuser, N. S. Oreshkina, A. Papoulia, P. Pyykkö, P.-G. Reinhard, S. Sailer, R. Sánchez, S. Schiffmann, S. Schmidt, L. Wehner, C. Wraith, L. Xie, Z. Xu, and X. Yang, Structural trends in atomic nuclei from laser spectroscopy of tin, *Commun. Phys.* **3**, 107 (2020).
156. S. T. Belyaev, Effect of pairing correlations on nuclear properties, *Mat. Fys. Medd. Dan. Vid. Selsk.* **31**, no. 11 (1959).
157. S. G. Nilsson and O. Prior, The effect of pair correlation on the moment of inertia and the collective gyromagnetic ratio of deformed nuclei, *Mat. Fys. Medd. Dan. Vid. Selsk.* **32**, no. 16 (1961).
158. M. J. A. de Voigt, J. Dudek, and Z. Szymański, High-spin phenomena in atomic nuclei, *Rev. Mod. Phys.* **55**, 949 (1983).
159. B. Banerjee, H. J. Mang, and P. Ring, Variational calculation of energy spectra of rotational nuclei at high spins, *Nucl. Phys. A* **215**, 366 (1973).
160. R. Bengtsson and S. Frauendorf, An interpretation of backbending in terms of the crossing of the ground state band with an aligned two-quasiparticle band, *Nucl. Phys. A* **314**, 27 (1979).
161. J. Dobaczewski and J. Dudek, Time-odd components in the mean field of rotating superdeformed nuclei, *Phys. Rev. C* **52**, 1827 (1995); *Phys. Rev. C* **55**, 3177(E) (1997).
162. A. Messiah, *Quantum mechanics. 2* (North-Holland Publishing Company, 1970).
163. C. Cohen-Tannoudji, B. Diu, and F. Laloë, *Quantum Mechanics - Volume III: Fermions, Bosons, Photons, Correlations, and Entanglement*, (Wiley-VCH, Berlin, 2019)
164. E. Perlińska, S. G. Rohoziński, J. Dobaczewski, and W. Nazarewicz, Local density approximation for proton-neutron pairing correlations: Formalism, *Phys. Rev. C* **69**, 014316 (2004).
165. M. Jaminon and C. Mahaux, Effective masses in relativistic approaches to the nucleon-nucleus mean field, *Phys. Rev. C* **40**, 354 (1989).
166. D. Tarpanov, J. Toivanen, J. Dobaczewski, and B. G. Carlsson, Polarization corrections to single-particle energies studied within the energy-density-functional and quasiparticle random-phase approximation approaches, *Phys. Rev. C* **89**, 014307 (2014).